AD-A082 752 RENSSELAER POLYTECHNIC INST TROY NY DEPT OF ELECTRIC--ETC F/G 17/1
ACOUSTO-OPTIC INTERACTION IN SURFACE ACOUSTIC WAVES AND ITS APP--ETC(U)
DEC 77 D SCHUMER, P DAS N00014-75-C-0772
UNCLASSIFIED MA-ONR-30 NL

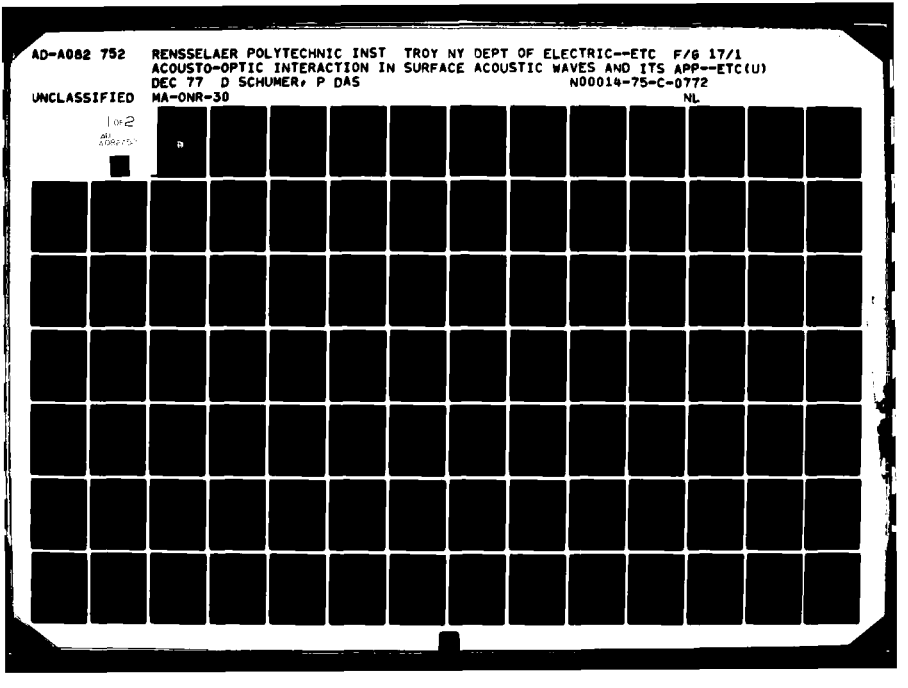

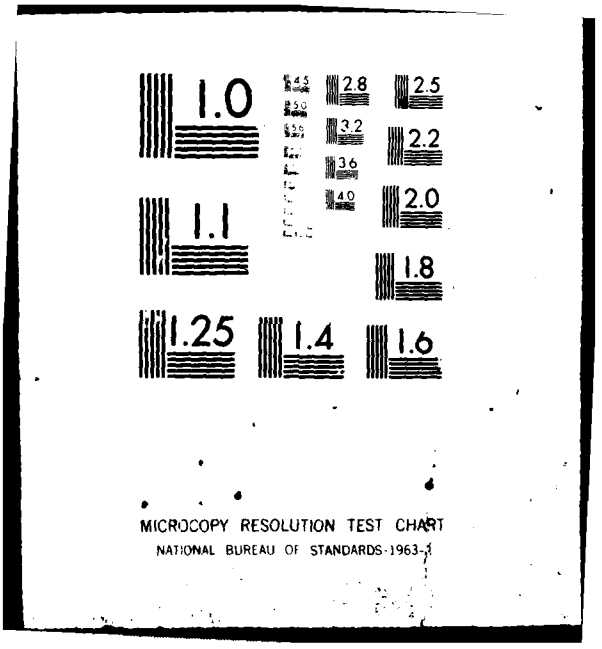
1.0
1.1
1.25
1.4
1.6
1.8
2.0
2.2
2.5
2.8
3.2
3.6
4.0
MICROCOPY RESOLUTION TEST CHART
NATIONAL BUREAU OF STANDARDS-1963-A

ACOUSTO-OPTIC INTERACTION IN SURFACE ACOUSTIC WAVES AND ITS APPLICATION TO REAL TIME SIGNAL PROCESSING

By

D. Schumer and P. Das

Electrical and Systems Engineering Department
Rensselaer Polytechnic Institute
Troy, New York 12181

December 30, 1977

Office of Naval Research
Contract N00014-75-C-0722
Project NR 009-017
Technical Report MA-ONR-30

SECURITY CLASSIFICATION OF THIS PAGE (When Data Entered)

REPORT DOCUMENTATION PAGE

READ INSTRUCTIONS BEFORE COMPLETING FORM

1. REPORT NUMBER: MA-ONR-30

2. GOVT ACCESSION NO.

3. RECIPIENT'S CATALOG NUMBER

4. TITLE (and Subtitle): ACOUSTO-OPTIC INTERACTION IN SURFACE ACOUSTIC WAVES AND ITS APPLICATION TO REAL TIME SIGNAL PROCESSING.

5. TYPE OF REPORT & PERIOD COVERED: Technical Report,

6. PERFORMING ORG. REPORT NUMBER

7. AUTHOR(s): D. Schumer [redacted] P. Das

8. CONTRACT OR GRANT NUMBER(s): N00014-75-C-0772

9. PERFORMING ORGANIZATION NAME AND ADDRESS
Electrical and Systems Engineering Department
Rensselaer Polytechnic Institute
Troy, NY 12181

10. PROGRAM ELEMENT, PROJECT, TASK AREA & WORK UNIT NUMBERS
NR-009-017

11. CONTROLLING OFFICE NAME AND ADDRESS
Office of Naval Research
Code 427
Washington, DC

12. REPORT DATE
Dec [redacted] 77

13. NUMBER OF PAGES
One hundred forty-eight (148)

14. MONITORING AGENCY NAME & ADDRESS (if different from Controlling Office)

15. SECURITY CLASS. (of this report)
UNCLASSIFIED

15a. DECLASSIFICATION/DOWNGRADING SCHEDULE

16. DISTRIBUTION STATEMENT (of this Report)
Unlimited

DISTRIBUTION STATEMENT A
Approved for public release;
Distribution Unlimited

17. DISTRIBUTION STATEMENT (of the abstract entered in Block 20, if different from Report)

18. SUPPLEMENTARY NOTES

19. KEY WORDS (Continue on reverse side if necessary and identify by block number)
Acousto-optics, Integrated optics, Optical Signal Processing.

20. ABSTRACT (Continue on reverse side if necessary and identify by block number)
The theory of the interaction of coherent light with surface acoustic waves and an experimental demonstration of the application of the interaction to new devices are presented. The analysis, based upon classical electromagnetic theory and a phenomenological formulation of the photoelastic effect, is applied to the piezoelectric material $LiNbO_3$, and provides good agreement with previously published experimental data. Explicit account is taken of the linear electro-optic and linear elasto-optic contributions to the interaction.
(cont. on back)

DD FORM 1 JAN 73 1473 EDITION OF 1 NOV 65 IS OBSOLETE

UNCLASSIFIED

SECURITY CLASSIFICATION OF THIS PAGE (When Data Entered)

The experimental demonstration of applications is restricted to the side-entry technique, an interaction configuration providing the longest interaction length between a surface acoustic wave and unguided optical wave. The relative merits of this configuration are discussed. New experimental results for the real-time side-entry convolver employing optical heterodyning include auto-correlation of Barker codes, ambiguity function generation, demonstration of a parallel acoustic track geometry to inhibit reflections, and measurement of diffraction characteristics for polarized light. Results are given for the correlation of a time varying light intensity distribution with an electrical signal, and the application to an optical communication system is indicated. The scanning of one and two dimensional black and white transparencies is performed, and the extension to color image scanning is demonstrated. All experiments are performed using Y-cut Z-propagating $LiNbO_3$. Acoustic frequencies employed range from 45 MHz to 100 MHz. Laser sources are HeNe and Ar.

Devices are analyzed and discussed with reference to the diffraction integral of scalar diffraction theory. The relation of this theory to the electromagnetic formulation of the acousto-optic interaction is discussed.

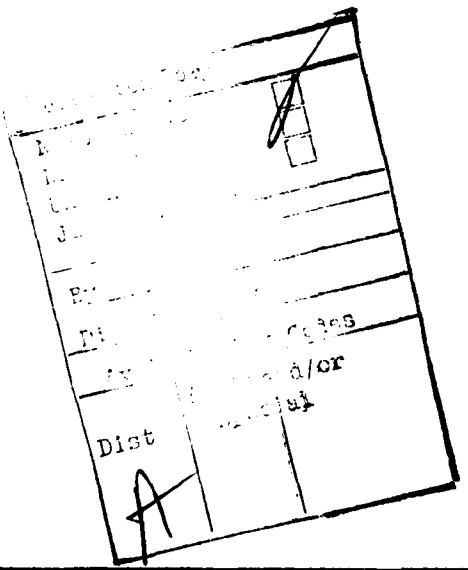

TABLE OF CONTENTS

Preface

This technical report was prepared by the Microwave Acoustics Laboratory, Electrical and Systems Engineering Department of Rensselaer Polytechnic Institute, Troy, New York. The partial support for this work came from Office of Naval Research Contract No. N00014-75-0772.

This report summarizes the work related to the real time signal processing and other applications of devices based on the acousto-optic interaction using SAW. Part of this work has already been published (References 52-56) and other parts will be published in the near future. The objective of this report is to present all the information in one place coherently.

Mr. L. Pearce, Mr. F. M. M. Ayub and Mr. H. Estrada-Vazquez have contributed significantly as co-authors of papers included in this report. Mr. R. T. Webster, Mr. Colin Lanzl and many students in the Laboratory have provided help in experimental set-up from time to time. Finally, most of this report forms the Ph.D. Thesis of Mr. D. Schummer.

LIST OF FIGURES

LIST OF TABLES

LIST OF SYMBOLS*

Chapter 1

x, y, z	spatial coordinates
t	time
n(z,t)	refractive index
n_o	unperturbed refractive index
n_1	perturbation of refractive index
a(subscript)	always denotes acoustic wave
ω_a	angular frequency (acoustic)
k_a	wavevector magnitude (acoustic)
p	elasto-optic constant
S	elastic strain
V_a	phase velocity (acoustic)
Λ	acoustic wavelength
f(subscript)	always denotes free space
λ_{o_f}	free space wavelength of incident light
n	labels the order (mode) of the diffracted light
I_n	intensity of n^{th} order diffracted light
J_n	n^{th} order Bessel function of first kind
ϕ	phase retardation introduced on light due to acoustic wave
λ	optical wavelength in medium
θ_B	Bragg angle

*Symbols are listed by chapter in which they are introduced.

Q	quantity used to distinguish Bragg, Raman-Nath, and transition regimes
L	interaction length
$k_{diffracted}$	wavevector (diffracted light)
$k_{incident}$	wavevector (incident light)
$k_{acoustic}$	wavevector (acoustic wave)
M_1, M_2, M_3	figures of merit
D	transducer height (bulk wave)
H	transducer width (bulk wave)
P_{ac}	acoustic power

Chapter 2

$x_1 = x$	
$x_2 = y$	Cartesian coordinates
$x_3 = z$	
E	electric field (optical)
E_i	component of electric field
B	impermeability tensor (inverse dielectric tensor)
B_{ij}	element of impermeability tensor
D_j	component of electric displacement vector
$P_{ijk\ell}$	element of elasto-optic tensor
$S_{k\ell}$	element of elastic strain tensor
u	particle displacement vector
u_i	component of particle displacement vector
$P_{ijk\ell}^{(E)}$	element of elasto-optic tensor (constant electric field)

$r_{ijm}^{(s)}$	element of electro-optic tensor (constant strain)
$E_m^{(a)}$	electric field associated with acoustic wave
q_{ijst}	photoelastic constant associated with rotation tensor
Ω	rotation tensor
Ω_{st}	element of rotation tensor
ϵ_{ij}	relative permittivity
ϵ_{ij}^{o}	unperturbed relative permittivity
$h^{(i)}$	refractive index for x_i-polarized light
c	speed of light in vacuum
$c^{(i)}$	speed of light in medium for x_i-polarized light
$S_{k\ell}$	complex elastic strain
e_m	complex electric field (acoustic)
$F_{k\ell}$	magnitude of complex elastic strain
$a_{k\ell}$	phase of complex elastic strain
G_m	magnitude of complex electric field (acoustic)
b_m	phase of complex electric field (acoustic)
R_{ij}	magnitude of perturbed part of relative permittivity
h_{ij}	phase of perturbed part of relative permittivity
B_a	acoustic wave amplitude
$C_{ij}^{(m)}$	amplitude coefficient of perturbed permittivity
$\Phi_n^{(i)}$	amplitude of n^{th} order diffracted light with x_i-polarization

$\phi_n^{(i)}$	amplitude of n^{th} order (differs from $\Phi_n^{(i)}$ by a phase factor)
w_n	angular frequency of n^{th} order diffracted light
f'	critical acoustic frequency
f_{min}	minimum acoustic frequency for polarization rotation
f_a	acoustic frequency
F_n	amplitude of n^{th} order (differs from $\Phi_n^{(i)}$ by a phase factor)
M_n	amplitude of n^{th} order (differs from $\Phi_n^{(i)}$ by a phase factor)
L_n	coefficient of driving term in coupled mode equation
$\beta^{(i)}$	free space incident angle of light normalized to ratio of optical to acoustic wavelength
$\theta_n^{(i)}$	diffraction angle of n^{th} order for x_i-polarization
η	change of scale variable
D	amplitude of incident light
A	undetermined coefficient
h	distance from surface of crystal
W	width of optical beam
C_d	constant characterizing photodetector
$\alpha_1,\alpha_2,\alpha_3$	Rayleigh wave decay parameters
N,O,P,m_{21},m_{31}, $n_{21},n_{31},a_{21},a_{31}$, b_{21},b_{31}	Rayleigh wave constants

Chapter 3

ζ, z, z'	spatial coordinates
$T(z)$	amplitude transmittance function
$f_1(t), f_2(t)$	envelope of electronic signal applied to IDT's
ℓ	optical aperture
d	length of ultrasonic delay line
C	normalizing constant
θ	diffraction angle
$A(\theta)$	amplitude distribution of diffracted light
$V_1(z), V_2(z)$	spatial replica of applied signal
L	interaction length
b	constant of proportionality
F	lens focal length
K	constant of proportionality
$\tau(\zeta)$	intensity transmission function
ω_{max}	largest angular frequency of input signal to modulator
ω	angular frequency
t	time
$S(\omega)$	frequency spectrum
$H(\omega)$	transfer function
N_o	noise spectral power density
α, τ	arbitrary real constants
$s(t)$	temporal signal
N	bit length of code

q_i	value of i^{th} bit of Barker code (= +1 or -1)
S/N	signal to noise power ratio
P_s	optical signal power
P_c	noise power from transmission channel
P_d	equivalent detector noise power
η	correlator deflection factor
N_i	ideal process gain of correlator
γ	noise power ratio (channel to detector)
R	image scanner resolution
T_p	pulse duration
S	diffraction limited spot size
λ	free space wavelength (optical)

CHAPTER 1

INTRODUCTION AND HISTORICAL REVIEW

1.1 Introduction

When a transparent material is mechanically deformed its index of refraction is affected. The physical basis of the refractive index change was first considered by Pockels, who gave a phenomenological description[1]. In 1922 Brillouin predicted that an ultrasonic acoustic wave propagating in a transparent material would give rise to a periodic modulation of the material's refractive index which would diffract an incident light beam,[2] and Debye and Sears observed the effect ten years later.[3]

More recently, the advent of the laser has provided renewed interest in the acousto-optic interaction of both an experimental and theoretical nature. Devices for laser modulation,[4] beam steering,[5] electronic filtering,[6] dye laser tuning,[7] digital signal multiplexing and demultiplexing,[8] spectrum analysis,[9] and correlation[10, 46] have been demonstrated and analyzed, to name a few representative applications.

In the next section we introduce some simple models which are useful in describing several features of the interaction. Subsequent sections treat acousto-optical materials and the acousto-optic interaction in surface acoustic waves.

1.2 Acousto-Optic Interactions: Raman-Nath and Bragg Scattering

For a single frequency ultrasonic wave traveling in the z-direction in some isotropic, homogeneous material, we can represent the refractive index in the region of the wave as

$$n(z,t) = n_o + n_1 \sin(\omega_a t - k_a z) \tag{1.1}$$

where n_o is the unpertubed refractive index and n_1 is the maximum change in refractive index arising from the presence of the sound wave. In terms of the elastic strain S, the elasto-optic constant p, and the unperturbed refractive index, n_1 is given by[150]

$$n_1 = \frac{1}{2} n_o^3 \, p \, S \tag{1.2}$$

The velocity of the acoustic wave, $v_a = \omega_a/k_a$, is normally about five orders of magnitude less than the velocity of light in the material. Consequently an optical beam incident on the sound wave effectively encounters a static phase grating of periodicity given by the acoustic wavelength Λ. It is well known that a spatially and temporally coherent, monochromatic, collimated light beam normally incident on such a phase grating is diffracted in the far field into several orders,[11] shown schematically in Fig. 1.1. The angle of the n^{th} order from the optic axis, θ_n, is given by

$$\sin \theta_n = \frac{n \lambda_{of}}{\Lambda} \quad , \tag{1.3}$$

in which λ_{of} is the free-space wavelength of the incident light. The intensity of the n^{th} order diffracted light, normalized to

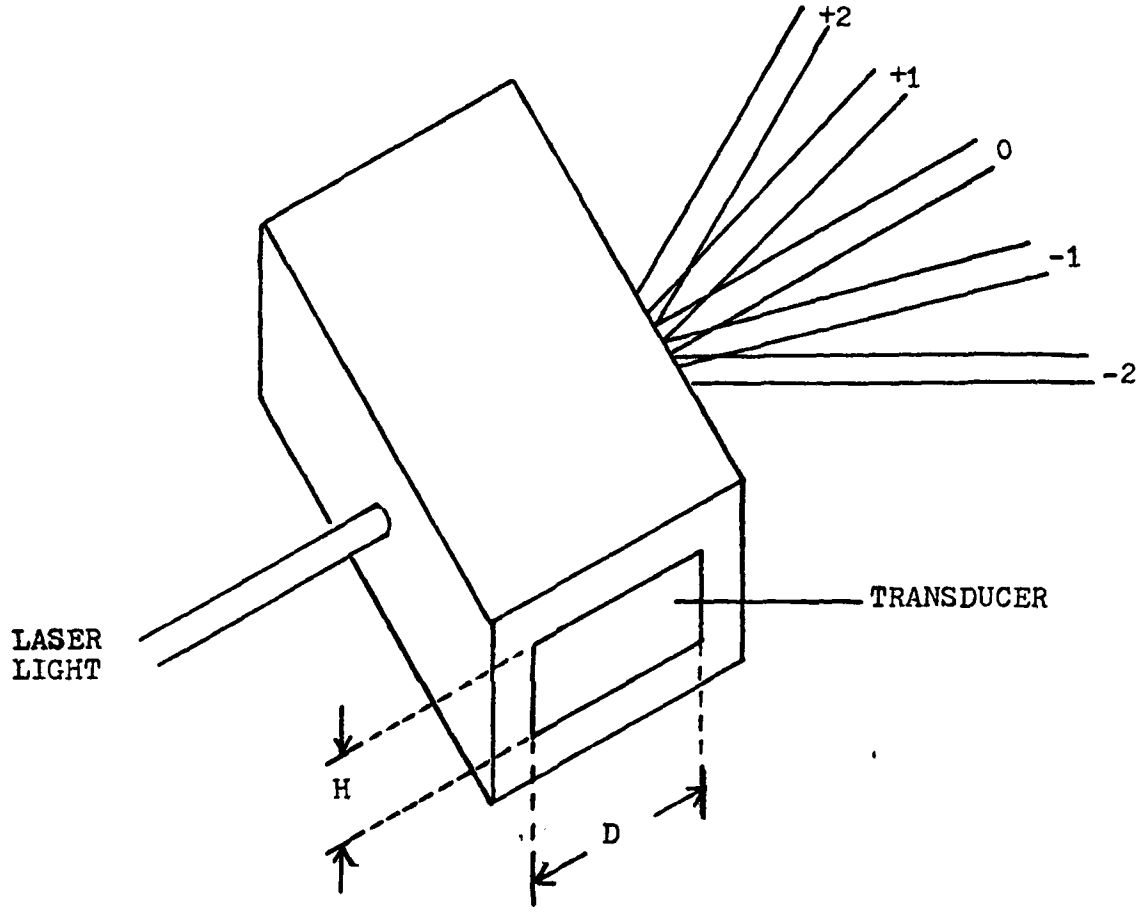

Fig. 1.1 Raman-Nath Diffraction
Acousto-optic interaction with bulk acoustic wave

that of the incident light, is given by

$$\frac{I_n}{I_o} = J_n^2(\phi). \tag{1.4}$$

J_n is the n^{th} order Bessel function and ϕ is the phase retardation introduced on the light due to the presence of the sound wave,

$$\phi = \frac{2\pi}{\lambda} n_1 L \quad , \tag{1.5}$$

in which λ is the wavelength in the medium and L is the interaction length. The interaction length is the distance over which the light and sound overlap, measured along the direction of optical propagation.

This description of the acousto-optic interaction in which the acoustic wave is considered as a phase grating was first given by Raman and Nath.[12] Under certain circumstances to be discussed, the effect of the acoustic wave is better described by considering the wave as a series of partially reflecting mirrors corresponding to the maxima of the refractive index wave, Eq. (1.1). In analogy to X-ray diffraction, when the light is incident at the Bragg angle θ_B given by

$$\theta_B = -\frac{1}{2}\frac{\lambda_{of}}{\Lambda} \quad , \tag{1.6}$$

the reflections constructively interfere in one direction giving rise to a single diffraction order of intensity

$$\frac{I_1}{I_o} = \sin^2\left(\frac{1}{2}\phi\right) \tag{1.7}$$

Bragg diffraction is shown schematically in Fig. 1.2(a), and in Fig. 1.2(b) is the momentum diagram for Bragg diffraction. The momentum diagram corresponds to a particle model of the interaction in which a photon and phonon are annihilated with the simultaneous creation of a new photon.[13] Conservation of momentum provides the result that the scattered light exits at an angle

$$\theta = \frac{1}{2} \frac{\lambda_{of}}{\Lambda} \quad , \tag{1.8}$$

and conservation of energy provides that the frequency of the scattered light is upshifted with respect to the incident light by the acoustic frequency. The shift in frequency could also have been arrived at by considering the doppler frequency shift of the light wave reflected from moving mirrors.[14]

A unified theory treating both Raman-Nath and Bragg scattering has been given by Klein and Cook[15] in which it is shown that the quantity Q, defined by

$$Q = \frac{2\pi \lambda_{of} L}{n_o \Lambda^2} \quad , \tag{1.9}$$

describes the nature of the acousto-optic interaction. For $Q \ll 1$, Raman-Nath diffraction occurs. For $Q \gg 1$, Bragg diffraction occurs. In the region $Q \sim 1$ an intermediate type of diffraction occurs.

The results of this section are developed more precisely within the framework of electromagnetic theory in Chapter 2, for the

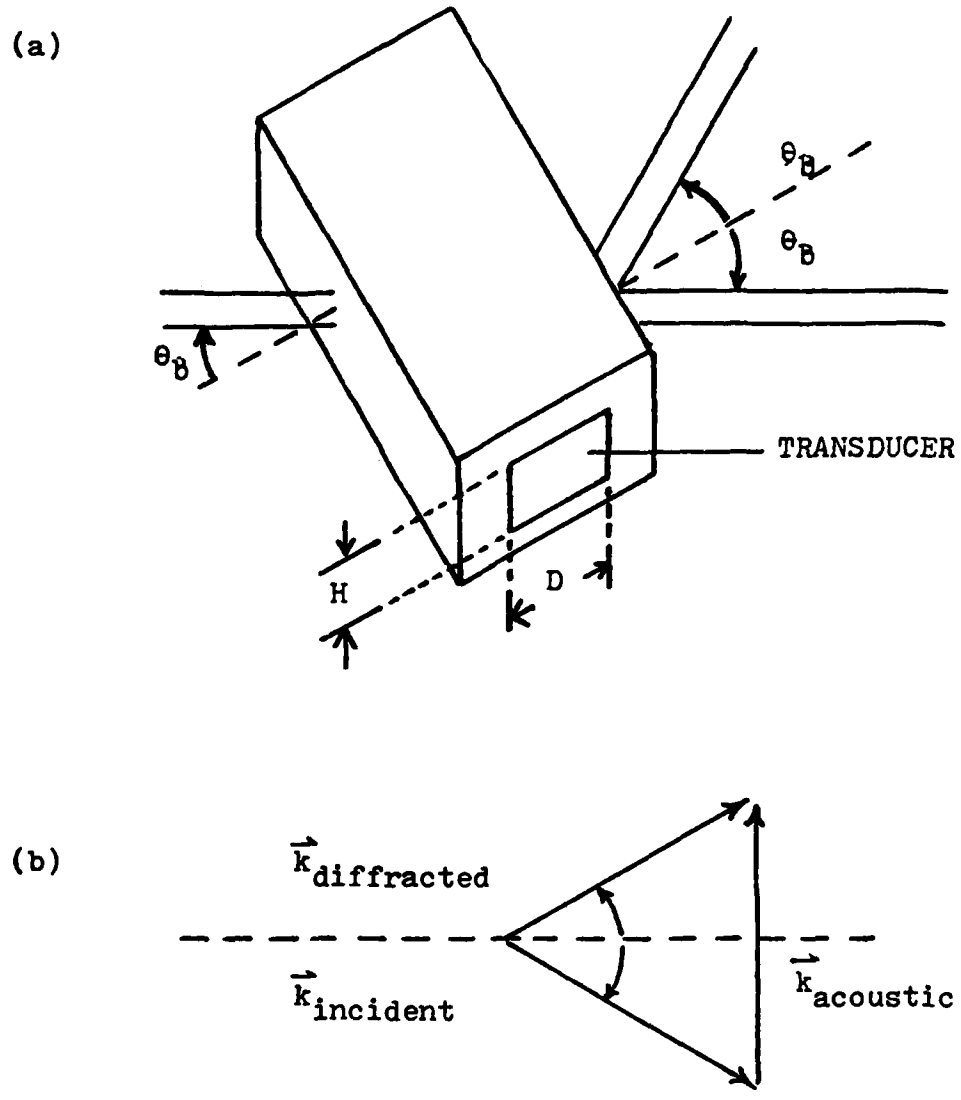

Fig. 1.2 Bragg Diffraction

(a) Acousto-optic interaction with bulk wave
(b) Momentum conservation for Bragg interaction

special case of surface acoustic waves. In the following section a discussion of acousto-optic materials is given.

1.3 Acousto-Optic Material Considerations

The acousto-optic interaction can be observed in both liquids and solids, in the latter case in amorphous and crystalline media belonging to all symmetry classes.[16] In comparing different materials it is useful to define certain figures of merit.[17,18,19] The most widely used are

$$M_1 = \frac{n_o^7 p^2}{\rho v_a} , \tag{1.10}$$

$$M_2 = \frac{n_o^6 p^2}{\rho v_a^3} , \tag{1.11}$$

and

$$M_3 = \frac{n_o^7 p^2}{\rho v_a^2} \tag{1.12}$$

in wich ρ is the material's mass density. The quantity M_2 is a material constant which is a measure of diffraction efficiency. In particular, the phase retardation ϕ appearing in Eqs. (1.4) and (1.7) can be written in the form

$$\phi = \pi \frac{2}{\lambda^2} \left(\frac{D}{H}\right) M_2 P_{ac} , \tag{1.13}$$

in which the ratio (D/H) is the inverse aspect ratio of the acoustic beam waist, and P_{ac} is the acoustic power. The figure M_1 takes into account diffraction bandwidth as well as efficiency, as does M_3 in

in the special case that the acoustic beam height is as small as the optical beam diameter. The relevancy of these figures is discussed in detail by Maydan.[20]

Pinnow[21] has proposed guidelines for the selection of acousto-optic materials which provide a qualitative estimate of the figures of merit of a material from its chemical formula and density. His conclusion is that there is a good possibility of finding materials with high figures of merit among the oxides which are dense and relatively soft and contain heavier cations. This is so because softness is related to low sound velocity, density with high refractive index, and heavy cations with higher photoelastic constants. His guidelines have led to the discovery of at least two new acousto-optic materials,[22] TeO_2 and $PbMoO_4$.

Factors not taken into account by the figures of merit, but which must be considered in selecting a material, include acoustic attenuation, optical transparency, chemical stability, mechanical durability, availability of an established technology for producing large and high quality boules, and the temperature coefficients of various physical constants, especially acoustic velocity.[23] Optical anisotropy is also not included in the figures of merit, and this can play an important role.[24,25]

Table 1.1 below provides comparative data for a few selected materials, taken from reference 23. The measurement of material constants and the identification of new useful materials is an important area of acousto-optics research.[26-29]

TABLE 1.1

Selected Acousto-Optic Materials

Material and Propagation Mode	Useful Wavelengths (μm)	Acoustic Attenuation at 500 MHz ($dB/cm \cdot GHz^2$)	M_1*	M_2*	M_3*
Fused Silica	.2 - 2.5	12	1.0	1.0	1.0
Water	.2 - .9	2400	4.6	80.7	18.52
Dense Flint (SF-59)	.46 - 2.5	1200	4.8	12.2	8.9
Si: L[111]	1.5 - 10	6.5	25.6	4.0	15.5
Ge: L[111]	2 - 20	30	1267.	575.	1370.
GaP: L[110]	.6 - 10.0	< 1	74.	29.5	69.
GaAs: L[110]	1 - 11	30	115.	67.	133
$LiNbO_3$: L[100]	.4 - 4.5	.15	8.3	4.5	7.5
$LiTaO_3$: L[001]	.4 - 5	.1	1.4	.8	1.4
α-HIO_3: L[001]	.3 - 1.8	10	12.8	55.	31.1
$PbMoO_4$: L[001]	.42 - 5.5	15	15.5	32.1	26.0
TeO_2: L[001]	.35 - 5	15	17.1	22.1	24.3
TeO_2: S[110]	.35 - 5	290	68	793	110

*Normalized to fused silica; computed from bulk wave data.

1.4 Acousto-Optic Interaction in Bulk and Surface Acoustic Waves

Until recently all acousto-optic devices and experiments have employed the interaction in bulk waves. Because of the considerable research and development effort invested in bulk wave device technology to date, it is to be expected that commercial applications of acousto-optics will be dominated by bulk wave devices for the next few years at least. This section discusses some problem areas attendant with bulk wave devices and provides a brief introduction and review of surface wave acousto-optics.

In bulk wave devices the acoustic wave is excited by means of a transducer fabricated from a plate cut from a piezoelectric crystal, across which the driving voltage is applied. A variety of transducer materials are available for this purpose, the most widely used in recent practice being $LiNbO_3$.[30] Bonding of the transducer to the acousto-optic medium is the most important technique in fabricating a bulk wave acousto-optic device.

The use of an organic adhesive such as epoxy is the simplest bonding technique. Because of the very low mechanical impedance of epoxy, which is highly mismatched to $LiNbO_3$ and other commonly used acousto-optic materials, the thickness of the epoxy layer must be kept to a small fraction of an acoustic wavelength. Chang[30] has obtained layers as thin as 0.1 μm which have given good results up to frequencies of 150 MHz. Above this frequency other techniques are required.

One method which has met with success is the cold-weld bonding technique using metallic bonding layers.[31] Indium is the most commonly used metal since good bonding can be obtained using low bonding pressure ($\sim$ 1000 psi) for a few seconds. However indium exhibits a rather large acoustic attenuation which precludes its use at high frequencies. Gold provides a good bond,[32] but owing to its extremely high mechanical impedance it is mismatched to most acousto-optical materials. Recently[30] conversion loss of less than 1 dB has been obtained at 350 MHz using aluminum as the bonding medium. A mechanical impedance close to that of indium, acoustic attenuation only slightly higher than gold, and a high electrical conductivity combine favorably in this material for use at high frequencies.

In addition to good transducer bonding, the attainment of high acoustic frequenices with bulk wave devices requires that the transducer plate be made to a thickness corresponding to the frequency of operation. For thicknesses in the range 3 - 6 microns, mechanical lapping is sufficient. Sputter etching[32] and ion milling[33] techniques have been developed to further reduce transducer thickness, .25 μm having been obtained. Stevenson and Hanak[34] have reported 1 dB conversion loss at an operating frequency of 1 GHz by applying ion milling and indium-gold bonding techniques.

Another problem area in the design of bulk acousto-optic devices, and surface wave devices as well, is that of

designing transducer impedance matching networks. In the bulk wave case, to a first approximation, the transducer acts as a large capacitor.[35] Due to the high dielectric constant of $LiNbO_3$, the impedance level of transducers for most devices can be on the order of a few ohms for frequencies above 100 MHz. Thus parasitic inductances can dominate the transducer impedance at high frequencies, raising the loaded Q of the transducer and narrowing bandwidth. The use of multiple series-connected transducers is often necessary to reduce transducer capacitance and raise impedance level. Although impedance matching networks based on filter synthesis have been developed, broadband matching is often obtained by resonating the transducer with a shunt inductance and transforming the source impedance by use of ferrite transformers or quarter wave transmission lines.

Recently there has been a trend toward the use of surface acoustic waves for acousto-optic devices, stimulated by advances in surface wave microwave acoustic technology.[36] The motivation for the development of surface wave acousto-optic devices is primarily miniaturization, ease of fabrication using planar technology, and compatability with the emerging integrated optics technology.[37] Further advantages of the use of surface waves over bulk waves are greater transducer flexibility[38] and the reduction in one dimension of acoustic beam diffraction limitations.

Theoretical interest in surface acoustic waves dates back to Lord Rayleigh's work in 1885,[39] but the acousto-optic application of such waves was not practical until the demonstration in 1968 of an efficient means of generating waves on the surface of the acousto-optic material $LiNbO_3$.[40] The technique is shown in Fig. 1.3. Electro-mechanical coupling between the interdigital transducer (IDT) and the crystal is achieved by means of the piezoelectric effect, which narrows the class of crystals to which this technique can be applied.[41] The use of piezoelectric materials to support the surface wave also significantly complicates the analysis of the wave propagation.[42]

In the figure is shown a single transducer with two finger pairs. The fingers are spaced, from center to center, a distance $\Lambda/2$ apart, where Λ is the acoustic wavelength at the design frequency. For YZ $LiNbO_3$, operation at a frequency of 100 MHz corresponds to a wavelength of approximately 35 μm. Generally, the electric-acoustic conversion efficiency of an interdigital transducer is proportional to the square of the number of finger electrode pairs. However, by considering the transit time for an acoustic wave to travel the length of the transducer, it is apparent that the IDT fractional bandwidth is given by the reciprocal of the number of finger pairs. In YZ $LiNbO_3$, five-finger pair transducers are used to optimize bandwidth and efficiency. In lieu of other requirements, the transducer aperture, length of finger overlap, is determined by electrical matching considerations.[43]

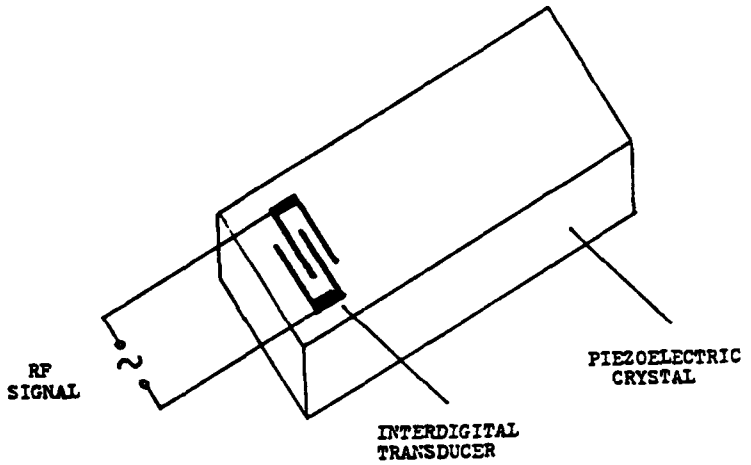

Fig. 1.3 Surface Wave Excitation

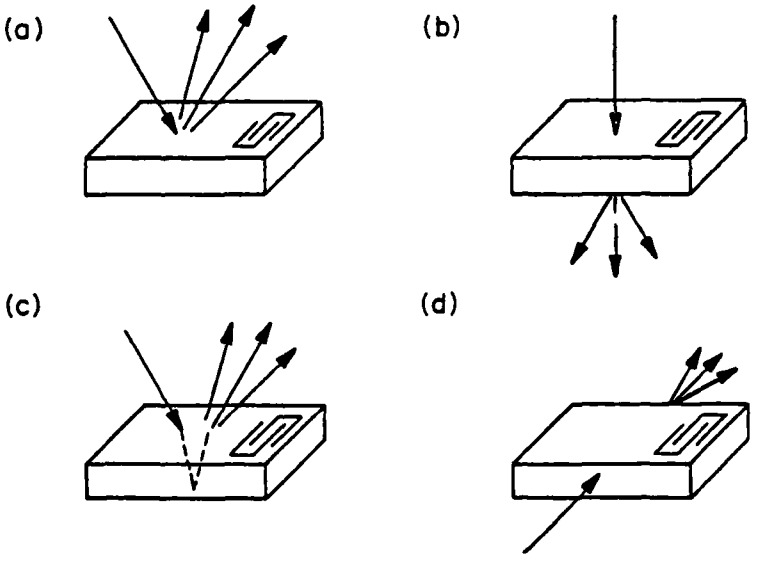

Fig 1.4 Interaction Configurations
(a) Top reflection (b) Top transmission
(c) Back reflection (d) Side entry

A variety of acousto-optic applications in surface acoustic waves have already been demonstrated. These have included surface wave probing for microwave acoustic device diagnosis,[44] real-time convolution using direct detection[45] and optical heterodyning,[46] light beam modulation,[47] image scanning,[48] and a host of others. Surface acoustic waves have also found application in the acousto-optic investigation of layer waves.[60]

Four interaction configurations have been used in the acousto-optic interaction between a surface acoustic wave and an unguided optical wave, shown in Fig. 1.4. In the top reflection configuration, 1.4(a), light is reflected from the surface on which the acoustic wave propagates. Diffraction occurs because of the slight surface corrugation associated with the propagation of the acoustic wave. Although the interaction is weakest in this configuration, it is a useful arrangement for the non-contact probing of surface waves.

A second interaction geometry is shown in 1.4(b), the top transmission configuration. The incident laser light is directed nearly normal to the acoustic propagation surface, and the diffracted light exits through the bottom of the crystal. Because the strain components of the surface acoustic wave decay with distance from the crystal surface, this configuration has a very short interaction length, on the order of an acoustic wavelength. A two-fold improvement in the interaction length is achieved through the scheme shown in 1.4(c), the back reflection

configuration. The light is here incident as in the top transmission case, but after exiting from the back side the light is reflected back by mirror through the crystal for a second pass through the acoustic wave. The periodic corrugation of the crystal surface due to the acoustic wave provides a slight additional phase contribution to that due to the internal effect. The top transmission and back reflection configurations have received considerable attention.[49,50]

The side entry technique, Fig. 1.4(d), provides a vast improvement in interaction length over the other configurations. The incident light in this case enters from the side of the crystal, near the crystal top surface, and propagates parallel to the surface on which the acoustic wave is propagating. The interaction length for the side-entry mode of operation is given, therefore, not by the depth of penetration of the acoustic wave below the crystal surface but rather by the acoustic beam width which is determined by the aperture of the interdigital transducer. For a transducer on YZ $LiNbO_3$ designed to match to 50 Ω at the center frequency, this is an improvement by two orders of magnitude over the top transmission case. Recent work suggests that a total internal reflection condition is achievable with the side-entry technique which provides an additional enhancement of the interaction in this device configuration.[47] Although optimum optical alignment is more difficult to achieve with the side-entry technique than with the other configurations, it is generally quite easy to exceed the interaction strength possible with the other interactions with even a non-optimal alignment.

Kramer has used the side-ent ry technique for mapping the decay of the Rayleight wave stran fields in $LiNbO_3$ and quartz,[51] and has reported on a real-time signal processor using this configuration.[46] More recent work at RPI has exploited this device configuration for a variety of applications.[52-56]

One feature common to all acousto-optic devices employing surface acoustic waves is that the figures of merit are larger than those for bulk devices employing the same material. This is due to the fact that the surface wave acoustic velocity is invariably smaller than the corresponding bulk wave velocity, on the order of a factor of 1.5. This corresponds to a factor of three improvement in the figure of merit M_2. Another advantage of surface acoustic waves over bulk waves is the very small acoustic beam waist aspect ratio, allowing for very efficient diffraction. However, of the four interaction configurations shown in Fig. 1.4, only the side-ent ry technique takes advantage of this fact.

The investigation of the acousto-optic interaction between surface acoustic waves and guided optical waves is an especially active area of applied optics. Beam deflection,[57] mode conversion,[58] and convolution[59] have been reported to date. Optical beam quality and in/out coupling efficiency is good for small optical apertures, which makes these devices well suited to beam steering applications, especially considering the potential low power requirements of these devices. Coupling over a large optical aperture remains a serious problem, and for the present this places a severe limitation on the practical application

of these devices to signal processors requiring a large time-bandwidth product, since this is proportional to the optical aperture.

1.5 Competitive Technologies

In some application areas alternative methods to the acousto-optic interaction are available. In the case of controllable light deflection, mechanical and electro-optic means have proven useful. The mechanical deflector, a mirror or prism, is driven by piezoelectric, galvanometric or magnetostrictive means. Its advantages are large number of resolveable spots, large deflection angle, and low optical loss. Deflection accuracy and scanning speed are problem areas which have yet to be overcome.

Electro-optic deflectors inherently exhibit fast responses and have been extensively investigated. With the exception of nitrobenzene Kerr cells[61] for digital light deflection, the unavailability of a high quality, large area electro-optical material having the capability of low power operation has prevented the use of the electro-optic deflector.

In the area of light modulation for the purpose of optical communications, the direct electronic modulation of the LED or solid state laser is sufficient and practical up to frequencies of about 150 MHz. To achieve the wide bandwidth potential of single mode optical fibers, the acousto-optic interaction may prove useful at higher frequencies.

For purposes of signal processing, conventional electronic and real-time digital computing methods are available for low frequency applications. In certain situations, including processing of optical images, charged coupled devices might prove competitive. At higher frequencies where the acousto-optic interaction might usefully be applied, other techniques have been demonstrated as well. Promising among these are those devices employing nonlinear coupling mechanisms between a surface acoustic wave propagating on a piezoelectric substrate and a semiconductor placed in close proximity.[62] Ultimately, both device performance as well as economic factors determine the appropriateness of a given technology for a given application.

CHAPTER 2

THEORY OF THE ACOUSTO-OPTIC INTERACTION IN SURFACE ACOUSTIC WAVES

2.1 Introduction

The theory of the acousto-optic interaction in surface acoustic waves is developed in this chapter and applied to the material $LiNbO_3$. As much work has been done in this area by other authors, an overview indicating the contributions of this chapter will be helpful.

Section 2.2 provides the foundation for the subsequent analysis. In that section the formulation of Pockels[1] is presented. This formulation couples a mechanical deformation to a material's optical properties by relating the optical permittivity tensor to elastic strain. Account is also taken of the fact that in piezoelectric materials, strains are associated with electric fields which can also perturb the permittivity tensor. This electro-optic contribution to the acousto-optic effect has been discussed by Coquin.[63]

In Section 2.4 the wave equation of classical electromagnetic theory is used to derive a set of coupled partial differential equations to describe the optical field. The strain and electric fields associated with a material deformation appear in these equations, introduced through the permittivity as discussed. Similar coupled equations have been given by Klein and Cook[15] who base their analysis on a scalar wave equation, Chang[30] in analyzing the case of a bulk wave in a non-piezoelectric material, and Lean[50] in analyzing the

surface wave case by means of a Green's function technique. In particular, Lean investigates the top transmission case including a contribution from the surface corrugation. Using the acoustic parameters provided by Spaight and Koerber,[68] the equations are provided for the specific case of $LiNbO_3$.

In Section 2.5 solutions are found for the formulated problem for the side-entry configuration. The problem had not previously been analyzed using actual Rayleigh wave parameters, although Kramer[71] provides similar results by considering a surface wave in an acoustically isotropic material. Numerical results are provided in Section 2.6 and are compared with Kramer's experimental findings.

2.2 Elasto-Optic and Secondary Electro-Optic Effect

The change in a material's refractive index due to a deformation is generally referred to as the photoelastic effect. In this chapter we employ a modification of the phenomenological formulation introduced by Pockels to describe this effect. In his formulation a mechanical strain gives rise to a proportional perturbation of the material's relative phase tensor $\overleftrightarrow{B}$. The phase tensor elements are defined through the linear relation

$$E_i = \frac{1}{\varepsilon_o} B_{ij} D_j \quad , \qquad (i,j = 1,2,3) \tag{2.1}$$

which relates the components of the electric and displacement fields of an optical wave propagating in a crystal. Equation (2.1) is written in rationalized MKS units, which are used throughout, in which ε_o is the permittivity of free space. Throughout this chapter, unless otherwise noted, the Einstein notation is employed in which summation over repeated subscripted indices is implied. According to the formulation of Pockels, the change in the relative phase tensor elements at optical frequencies is given by

$$\Delta B_{ij} = P_{ijk\ell} S_{k\ell} \quad , \tag{2.2}$$

where $P_{ijk\ell}$ are the elements of the fourth rank elasto-optic tensor and $S_{k\ell}$ is the infinitesimal strain defined below.

If $\vec{u}$ represents the vector displacement of a material point due to a deformation, and u_i are the magnitudes of the components in an orthogonal coordinate system with axes x_i ($i = 1,2,3$), then in the so-called "small deformation theory" of continuum mechanics in which the displacement gradients $\partial u_i/\partial x_i$ are small compared to unity, the infinitesimal strain tensor is given by

$$S_{k\ell} = \frac{1}{2}\left(\frac{\partial u_\ell}{\partial x_k} + \frac{\partial u_k}{\partial x_\ell}\right) \quad . \tag{2.3}$$

While we take Eq. (2.3) as the definition of strain for our purposes, $S_{k\ell}$ is in fact the infinitesimal limit to which both the Lagrangian and Eulerian strain tensors of finite deformation theory reduce. While in finite deformation theory a distinction must be made as to whether the coordinate system is fixed in space or fixed in the body of the material continuum, no such distinction need be made in the present "small deformation" treatment.

In piezoelectric materials, in which the strain is coupled via the piezoelectric effect to an associated electric field, a deformation can also give rise to a change in refractive index by means of the electro-optic effect. It was pointed out by Coquin[63] that in lithium niobate, which is highly piezoelectric, this can be a large effect, as important as the direct photoelastic effect. Thus we must write[64]

$$\Delta B_{ij} = P^{(E)}_{ijk\ell} \; S_{k\ell} + r^{(s)}_{ijm} \; E^{(a)}_m \tag{2.4}$$

where $r_{ijm}^{(s)}$ is the linear electro-optic tensor element measured at constant strain, $P_{ijk\ell}^{(E)}$ is the elasto-optic tensor element at constant electric field, and $E_m^{(a)}$ is the m^{th} component of the electric field associated with a deformation in the piezoelectric material. The superscript (a), referring to acoustic, distinguishes $E_m^{(a)}$ from the electric field associated with the light, which is oscillatory at a frequency much higher than that associated with piezoelectric phenomena.

Recently Nelson and Lax[65] have pointed out that the phenomenological formulation of Pockels is incomplete and neglects rotation effects arising from shear waves which should be included in strongly birefringent materials. Thus in place of the strain, a symmetric tensor, the displacement gradient which is asymmetric is taken by them as the more basic quantity. Equivalently, we could include a contribution to the optical relative inverse dielectric tensor (impermeability tensor) proportional to the rotation tensor, so that

$$\Delta B_{ij} = P_{ijk\ell} S_{k\ell} + q_{ijst} \Omega_{st} + r_{ijm} E_m^{(a)} , \qquad (2.5)$$

where the rotation tensor $\overleftrightarrow{\Omega}$ is the antisymmetric second rank tensor with elements defined by

$$\Omega_{st} = \frac{1}{2} \left(\frac{\partial u_s}{\partial x_t} - \frac{\partial u_t}{\partial x_s} \right) . \qquad (2.6)$$

Except for the material rutile,[66] experimental observation has not been made of the existence of nonvanishing tensor elements

$q_{ijk\ell}$. As we are interested in a numerical solution for the acousto-optic effect in lithium niobate, we do not include the rotation contribution in subsequent analysis, although such inclusion is easily facilitated within the framework to be developed. It should be specifically noted, too, that the present formulation is based upon linear piezoelectric constitutive relations, the linear electromagnetic constitutive relations, and linear elasto-optic and electro-optic relations.

In the description of the acousto-optic interaction to be developed, our interest is not in how the impermeability tensor is perturbed by the mechanical deformation, but rather how the optical dielectric tensor itself is perturbed. Writing the relative permittivity as

$$\varepsilon_{ij} = \varepsilon_{ij}^{o} + \Delta\varepsilon_{ij} \quad , \tag{2.7}$$

where ε_{ij}^{o} is the unperturbed tensor element and $\Delta\varepsilon_{ij}$ is the perturbation, it follows from

$$D_i = \varepsilon_{ij} E_j \tag{2.8}$$

and Eqs. (2.1) and (2.4) that, to linear terms in $S_{k\ell}$ and $E_m^{(a)}$,

$$\Delta\varepsilon_{ij} = -(\varepsilon_{ii}^{o})^2 [P_{ijk\ell} S_{k\ell} + r_{ijm} E_m^{(a)}] \quad . \tag{2.9}$$

The values of the unperturbed dielectric tensor elements ε_{ij}^{o} are those appropriate at optical frequencies. In the coordinate system in which the unperturbed dielectric tensor is diagonal, these elements are given by

$$\varepsilon^{o}_{ij} = \varepsilon^{o}_{ij}\,\delta_{ij} = [n^{(i)}]^2 \quad , \tag{2.10}$$

where δ_{ij} is the Kronecker delta, and $n^{(i)}$ is the refractive index for light polarized along the principal axis x_i. In lithium niobate, an optically uniaxial crystal, $\varepsilon^{o}_{11} = \varepsilon^{o}_{22} \neq \varepsilon^{o}_{33}$.

2.3 The Acousto-Optic Interaction

As discussed in Chapter 1, when an ultrasonic wave propagates through a transparent material, the refractive index of that material is perturbed by the presence of that wave via the photoelastic effect. The refractive index perturbation is periodic in the direction of acoustic propagation. Light passing through the medium can undergo diffraction as a direct result of this perturbation. This effect is referred to as the acousto-optic interaction. If the interaction rotates the polarization of the incident light, we refer to the interaction as a polarization rotating, or simply rotating, interaction. If the interaction does not rotate the light polarizaiton, we refer to the interaction as nonrotating. In the former case the refractive index for the incident and diffracted light will generally not be equal in an optically anisotropic material. Such would be the case in lithium niobate for a diffraction process coupling light polarized in the x_3 direction with light polarized along either of the other axes. In both the rotating and nonrotating cases, the diffracted light is generally shifted in its frequency from the incident light by an integral multiple of the acoustic

frequency. For this reason some authors[67,30] view the interaction as a parametric interaction in which the optical wave mixes with the acoustic wave to generate polarizion waves at the combination frequencies which then radiate at these new frequencies. Even though the linear constitutive relations and linear elasto- and electro-optic relations are employed, the acousto-optic interaction is inherently nonlinear. The mixing of frequency occurs in our present theory due to a term in the wave equation for the optical field which involves the product of the optical field with the perturbed part of the permittivity.

2.4 Coupled Mode Equations and Phase Matching Considerations

Starting with Maxwell's equations the following wave equation is obtainable which describes the electric field of the optical wave in the crystal. The details of this derivation are shown in the Appendix.

$$- \nabla^2 E_i + [\nabla(\nabla \cdot E)]_i = - \mu_o \frac{\partial^2}{\partial t^2} \varepsilon_{ij} E_j \qquad (2.11)$$

It is further shown in the Appendix that the gradient term in Eq. (2.11) is small compared to all other terms and can be neglected. The resultant equation, which provides the basis for the present investigation of the acousto-optic interaction, relates the optical field to the material's permittivity which is perturbed by the acoustic wave. Written in a cartesian coordinate system, employing indicial notation,

$$\nabla^2 E_i = \frac{1}{c^2} \frac{\partial^2}{\partial t^2} \varepsilon_{ij} E_j \quad , \tag{2.12}$$

where E_i is the i^{th} component of the electric field associated with the light propagating in the material, and ε_{ij} is an element of the permittivity tensor, given explicitly by Eq. (2.7).

With reference to the geometry of Fig. 2.1, the acoustic strain and associated electric field can be written as

$$S_{k\ell} = \frac{1}{2} (s_{k\ell} + s_{k\ell}^*) \tag{2.13}$$

and

$$E_m^{(a)} = \frac{1}{2} (e_m + e_m^*) \tag{2.14}$$

in which the asterisk * denotes complex conjugate, and

$$s_{k\ell} = F_{k\ell}(y)\, e^{ja_{k\ell}(y)}\, e^{j(\omega_a t - k_a z)} \tag{2.15}$$

$$e_m = G_m(y)\, e^{jb_m(y)}\, e^{j(\omega_a t - k_a z)} \quad , \tag{2.16}$$

where F_{ij}, G_m, $a_{k\ell}$, and b_m are real-valued functions of the variable $y = x_2$. The subscript "a" on quantities in Eqs. (2.15) and (2.16) refers to the acoustic wave. The coordinates (x,y,z) and (x_1,x_2,x_3) are used interchangeably throughout the chapter. While the latter enable us to use the compact indicial notation, the former are conventionally used in specifying crystallographic cuts. The imaginary unit, $j = \sqrt{-1}$, is easily distinguished from a sub- or superscript j, used as an index, from its context.

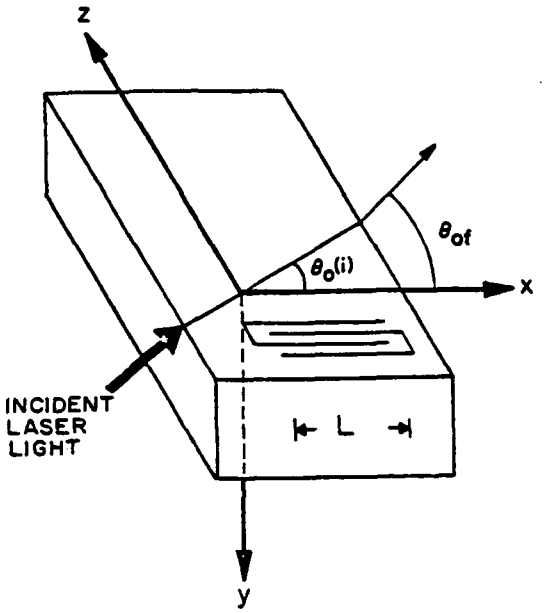

Fig. 2.1 Gecmetry for Acousto-Optic Interaction

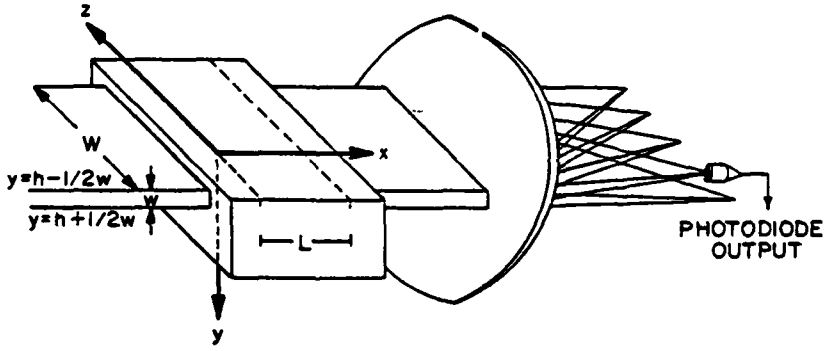

Fig. 2.2 Geometry for Acousto-Optic Interaction

While we are concerned with the solution to Eq. (2.12), subject to boundary conditions, for practical cases in which the width W of the incident light beam is of finite extent in the z-direction, or the acoustic disturbance itself is of finite spatial extent on the crystal or is not of constant amplitude, such effects will not be taken into explicit account in the following analysis. The effect of a finite optical aperture is well understood and is discussed in optics texts treating diffraction.[11] In subsequent chapters, in which applications of the interaction are discussed, the effect of a finite optical aperture is introduced where required. The case in which the acoustic disturbance is not of constant amplitude or is of finite spatial extent on the crystal is of crucial importance to the operation of all the devices described. The modifications required to apply the results of this chapter in describing those devices are explicitly noted for each device application in the appropriate section.

It follows from Eqs. (2.9), (2.13), (2.14), (2.15), and (2.16) that the perturbed relative permittivity is of the form

$$\Delta\varepsilon_{ij} = R_{ij}(y)\, e^{jh_{ij}(y)}\, e^{j(\omega_a t - k_a z)} + \text{C.C.} \qquad (2.17)$$

in which R_{ij} and h_{ij} are real valued functions of y. It is shown in the next section that for the acousto-optic interaction with surface waves in lithium niobate, only the functions $\Delta\varepsilon_{22}$ and $\Delta\varepsilon_{33}$ are of practical interest for the geometry shown in Fig. 2.1.

For a z-propagating Rayleigh wave on a stress free y-cut lithium niobate substrate, $\Delta\varepsilon_{ij}$ has the analytic form*

$$\Delta\varepsilon_{ij} = -\frac{1}{2}(\varepsilon_{ii}^{o})^{2} B_a k_a [C_{ij}^{(1)} e^{-j\alpha_1 k_a y} + C_{ij}^{(2)} e^{-j\alpha_2 k_a y} + C_{ij}^{(3)} e^{-j\alpha_3 k_a y}] + C.C. \quad (2.18)$$

where B_a is the amplitude of the acoustic wave, and the other constants characterize the material. The coefficients $C_{ij}^{(m)}$ are the sum of an elasto-optic and an electro-optic contribution, $C_{ij}^{(m)s}$ and $C_{ij}^{(m)e}$ respectively. All constants are provided in Section 2.5 of this chapter.

As a solution to the wave equation (2.12) we take a plane wave expansion of the form

$$E_i(x,y,z,t) = \sum_{n=-\infty}^{\infty} \phi_n^{(i)}(x,y) e^{j(\omega_n t - \vec{k}_n^{(i)} \cdot \vec{r})} \quad (2.19)$$

in which $\phi_n^{(i)}$ is the amplitude of the n^{th} diffracted order, $\vec{r}$ is the position vector, ω_n the frequency of the n^{th} order, and $k_n^{(i)}$ the wave vector associated with the n^{th} order optical mode. The superscripts on the mode amplitude and wave vector indicate that these depend on the particular electric field component (i.e. light polarization). The frequency ω_n and wave vector $\vec{k}_n^{(i)}$ obey

$$\omega_n = \omega_{n-1} + \omega_a \quad (2.20)$$

---

*Based on Spaight and Koerber.[68]

and

$$\vec{k}_n^{(i)} = \vec{k}_{n-1}^{(j)} + \vec{k}_a \tag{2.21}$$

in which ω_o is the frequency of the incident light and $\vec{k}_a$ is the acoustic wave vector. The wavevector of the incident light is denoted by $\vec{k}_o^{(p)}$, where p is either 2 or 3. It follows from Eq. (2.20) that

$$\omega_n = \omega_o + n\,\omega_a \quad . \tag{2.22}$$

Referring to the geometry of Fig. 2.1,

$$\vec{k}_n^{(i)} \cdot \vec{r} = k_n^{(i)} \cos\theta_n^{(i)}\, x + k_n^{(i)} \sin\theta_n^{(i)}\, z \quad , \tag{2.23}$$

where all wavevectors and angles in Eq. (2.23) are measured in the medium. *Using Eqs. (2.21) and (2.23),* conservation of momentum in the x-direction provides

$$k_n^{(i)} \cos\theta_n^{(i)} = k_{n-1}^{(j)} \cos\theta_{n-1}^{(j)} \quad , \tag{2.24}$$

and conservation in the z-direction yields

$$k_n^{(i)} \sin\theta_n^{(i)} = k_{n-1}^{(j)} \sin\theta_{n-1}^{(j)} + k_a \quad . \tag{2.25}$$

In terms of the incident light polarized along x_p axis (p = 2,3), Eqs. (2.24) and (2.25) can be written

$$k_n^{(i)} \cos\theta_n^{(i)} = k_o^{(p)} \cos\theta_o^{(p)} \tag{2.26}$$

and

$$k_n^{(i)} \sin \theta_n^{(i)} = k_o^{(p)} \sin \theta_o^{(p)} + n k_a \qquad (2.27)$$

The angles can be related to quantities in free space by means of Snell's Law,.

$$\sin \theta_{nf} = n^{(i)} \sin \theta_n^{(i)} \qquad (2.28)$$

in which the subscript f denotes free space. Similarly, wave vector magnitudes can be related to free space quantities by

$$n^{(i)} k_{nf} = k_n^{(i)} \quad , \qquad (2.29)$$

in which the wave vector magnitude for free space propagation k_{nf}, is related to the free space wavelength λ_{nf} by

$$k_{nf} = \frac{2\pi}{\lambda_{nf}} \qquad (2.30)$$

It should be observed that, in general, $n^{(i)}$ depends upon the direction of the propagating wave. We assume that all angles considered are sufficiently close that the refractive index may be treated as a constant for each polarization.* For incident light not polarized along the y- or z-axis, the light must first be decomposed into components along those axes. Each component is then treated separately, the results being combined at the exit face of the crystal.

With the definition

$$\phi_n^{(i)}(x,y) = \Phi_n^{(i)}(x,y)\, e^{-j k_o^{(i)} \cos \theta_o^{(i)} x} \quad , \qquad (2.31)$$

*The assumption is good for the experiments reported here, but becomes invalid at higher acoustic frequencies.

the field can be written

$$E_i = \sum_{n=-\infty}^{\infty} \phi_n^{(i)}(x,y) \; e^{j[\omega_n t - (k_o^{(i)} \sin \theta_o^{(i)} + n\, k_a)z]} \tag{2.32}$$

Substituting Eq. (2.32) into the wave equation (2.12) and equating terms at the light frequency $(\omega_o + n\,\omega_a)$ provides a coupled system of linear second order coupled-mode partial differential equations.

$$\frac{\partial^2}{\partial x^2} \phi_n^{(i)} + \frac{\partial^2}{\partial y^2} \phi_n^{(i)} + [\frac{\omega_n^2}{c^2} \varepsilon_{ii}^o - (k_o^{(i)} \sin \theta_o^{(i)} + n\, k_a)^2] \phi_n^{(i)}$$

$$= -\frac{1}{2} \frac{\omega_n^2}{c^2} R_{ii} [e^{jh_{ii}} \phi_{n-1}^{(i)} + e^{-jh_{ii}} \phi_{n+1}^{(i)}]$$

$$-\frac{1}{2} \frac{\omega_n^2}{c^2} R_{ij} [e^{jh_{ij}} \phi_{n-1}^{(j)} + e^{-jh_{ij}} \phi_{n+1}^{(j)}] \tag{2.33}$$

where $i \neq j$ in this equation. Use has been made of the fact that in the coordinate system employed, the unperturbed permittivity tensor is diagonal.

Several comments are in order regarding Eq. (2.33). It must be pointed out first that this represents two equations which are coupled, since $i = 2,3$. The term corresponding to $i = 1$ is neglected since the case with which we shall be concerned, all light propagation is along the x-axis, or nearly so, with the result $E_x \simeq 0$. Further, for the particular surface wave considered, a z-propagating Rayleigh wave on a y-cut crystal, there is no x-component of mechanical strain, thus $j = 2,3$ only. The diffracted

orders (modes) $\phi_n^{(i)}$ are coupled to adjacent orders through the subscript. This coupling can be to light of both the same and also orthogonal polarization, as provided by the superscript. The first term on the right hand side provides for the case in which the adjacent modes are of the same polarization. The second term on the right hand side provides for coupling between different polarizations and allows for the possibility that the refractive indices for the adjacent modes can be different. In Eq. (2.33), coupling is only between adjacent orders, i.e. $\phi_n^{(i)}$ is coupled to $\phi_{n+1}^{(i)}$ and $\phi_{n-1}^{(i)}$. This arises from the fact that in Eq. (2.17) $\Delta\varepsilon_{ij}$ has a simple sinusoidal time dependence. In the more general case that $\Delta\varepsilon_{ij}$ is periodic in time, expressed as a Fourier sum of sinusoids, coupling would be possible to other than just the adjacent mode.

Before proceeding to construct solutions to Eq. (2.33) subject to boundary conditions, considerable physical insight as well as an important mathematical simplification can be achieved by a more careful consideration of the phase expressions, Eqs. (2.23) through (2.27). We prove first that in all practical cases there cannot exist polarization rotation between axes of different refractive index in any multiple order diffraction, such as Raman-Nath diffraction. We prove this by assuming such an interaction can occur and show that this implies an inconsistency.

Consider coupling between the incident light with polarization along the x_p axis and the first order with polarization

along x_i. Squaring Eq. (2.26) and substituting from Eq. (2.27) provides for n = 1,

$$\sin \theta_1^{(i)} = \frac{k_a}{2 k_1^{(i)}} + \frac{k_{o_f}}{2n^{(i)} k_a} (n^{(i)^2} - n^{(p)^2}) \quad . \tag{2.34}$$

In terms of the acoustic frequency, Eq. (2.34) can be written

$$\sin \theta_1^{(i)} = \frac{1}{2} \frac{\lambda_{o_f}}{n^{(i)} v_a} [f_a + \frac{v_a^2}{\lambda_{o_f}^2 f_a} (n^{(i)^2} - n^{(p)^2})], \tag{2.35}$$

in which f_a and v_a are, respectively, the acoustic frequency and velocity. Equation (2.35) is a valid and useful result for an acousto-optic interaction involving only two modes, such as Bragg diffraction which involves an incident and a single diffraction mode. It is a feature of Eq. (2.35) that there is a critical frequency f' at which the two terms in brackets on the right hand side are equal. This frequency is given by

$$f' = \frac{v_a}{\lambda_{o_f}} \left| n^{(i)^2} - n^{(p)^2} \right| \tag{2.36}$$

For $f_a < f'$, the second term in the brackets of Eq. (2.35) is the larger of the two terms, in magnitude. This is generally the case for a polarization-rotating interaction involving a surface acoustic wave in $LiNbO_3$. For λ_{o_f} = 6328 Å, f' = 3.5 GHz. Experiments reported here were well below this frequency.

Having established the foregoing it is easily shown that multiple diffractions involving polarization rotation cannot occur below 1/2 f'. If it could occur then coupling to the second order would provide

$$\sin \theta_2^{(p)} = \frac{\lambda_{o_f}}{n^{(p)} v_a} \left[f_a + \frac{v_a^2}{4 \lambda_{o_f}^2 f_a} (n^{(p)2} - n^{(i)2}) \right] \tag{2.37}$$

which is derived in exactly the same manner that Eq. (2.35) was. Below frequencies 1/2 f' the sign of $\sin \theta_2^{(p)}$ is given by the sign of $[n^{(p)2} - n^{(i)2}]$, while the sign of $\sin \theta_1^{(i)}$ is of the opposite sign. If multiple order diffraction involving polarization rotation could occur, both angles would be of the same sign. For this reason, in studying Raman-Nath diffraction in highly birefringent materials, we need not include the term involving R_{ij} $(i \neq j)$ in Eq. (2.33).

For an interaction involving only a single diffracted order, such as Bragg diffraction, polarization rotation is not precluded by the above argument. We can identify two possible cases. In the event that the diffracted order is of the same polarization as the incident light, Eq. (2.33) applies with the R_{ij} term excluded. In the event that the diffracted order and the incident order are of orthogonal polarizaiton, Eq. (2.33) applies with the R_{ii} term excluded. The case that the diffracted order is a superposition of both polarizations is precluded by Eq. (2.35), except in the collinear case described below.

It follows from Eq. (2.25) that for the case of an acousto-optic diffraction involving only one diffraction order, there is a minimum acoustic frequency at which the interaction can occur if the diffracted and incident light are of orthogonal polarization. This frequency occurs for the case in which $\sin \theta_1^{(i)} = \sin \theta_o^{(p)}$, which corresponds to the incident and diffracted light propagating collinearly with the acoustic wave. This minimum acoustic frequency is given by

$$f_{min} = \frac{v_a}{\lambda_{o_f}} \left(n^{(i)} - n^{(p)}\right) \quad . \tag{2.38}$$

As a consequence of Eq. (2.38), which assumes that the incident and diffracted light both propagate in the same direction as the acoustic wave, if $n^{(i)} \neq n^{(p)}$ then the interaction can only occur if $n^{(i)} > n^{(p)}$. That is, the incident polarization must be along the axis of smaller refractive index. It is to be noted, too, that if $n^{(i)} = n^{(p)}$, such as for an optically isotropic crystal, or for light propagation along the c-axis of a uniaxial crystal, f_{min} is zero. In these circumstances the interaction is possible for acoustic frequencies down to the dc limit. Finally, had we considered the case in which the acoustic and light waves propagate collinearly but in opposite directions, the condition $n^{(i)} > n^{(p)}$ would be replaced by $n^{(p)} > n^{(i)}$.

Equation (2.19) expresses the optical field in the medium as a linear superposition of plane waves at frequencies $\omega_n = \omega_o + n\,\omega_a$, $(n = 0, \pm 1, \pm 2, \ldots)$. For light polarized

in the i^{th} direction, (i = 2,3), the local intensity of the n^{th} order is

$$I_n^{(i)} = |\phi_n^{(i)}|^2 \tag{2.39}$$

The z-component of the wavevector for this wave is $(k_o^{(i)} \sin \theta_o^{(i)} + n\, k_a)$, thus the sine of $\theta_n^{(i)}$, the angle between the x-axis and the direction of propagation of the wave at frequency ω_n is

$$\sin \theta_n^{(i)} = \frac{c^{(i)} [k_o^{(i)} \sin \theta_o^{(i)} + n\, k_a]}{\omega_o + n\, \omega_a} , \tag{2.40}$$

in which $c^{(i)}$ is the speed of light in the medium for polarization along the x_i axis. With Snell's Law, and using the approximation that

$$n\, \omega_a << \omega_o \tag{2.41}$$

it immediately follows that

$$\sin \theta_{n_f} = \sin \theta_{o_f} + \frac{n\, \lambda_{o_f}}{\Lambda} \tag{2.42}$$

in which the subscript f refers to free space. The quantities θ_n, λ_{o_f}, and Λ are, respectively, the angle from the x-axis of the direction of propagation for the n^{th} mode, the free space wavelength of the incident light, and the acoustic wavelength which is related to the magnitude of the acoustic wavevector by

$$|\hat{k}_a| = \frac{2\pi}{\Lambda} \tag{2.43}$$

Of special interest are the cases corresponding to Raman-Nath and Bragg scattering. In the former, near normal

incidence, $\theta_{o_f} \simeq 0$,

$$\sin \theta_{n_f} \simeq \frac{n \lambda_{o_f}}{\Lambda} \tag{2.44}$$

In the latter, incidence is at the Bragg angle, $\lambda_{o_f} = \theta_B$, where θ_B is defined by

$$\sin \theta_B = -\frac{1}{2} \frac{\lambda_{o_f}}{\Lambda} \quad , \tag{2.45}$$

assuming the refractive indices for the incident and diffracted wave are the same. Thus the diffracted order occurs at θ_{1_f} given by

$$\sin \theta_{1_f} = \frac{\lambda_{o_f}}{2\Lambda} \quad , \tag{2.46}$$

which agrees with the previous result, Eq. (2.35), when $n^{(i)} = n^{(p)}$, as expected.

2.5 Simplification of the Coupled Mode Equations: Solutions for Raman-Nath and Bragg Diffraction

In the preceding section the coupled mode equations were formulated, and arguments based on the conservation of pseudomomentum were given to simplify those equations. The result of those arguments is that Eq. (2.33) becomes

$$\frac{\partial^2}{\partial x^2} \phi_n^{(i)} + \frac{\partial^2}{\partial y^2} \phi_n^{(i)} + [\frac{\omega_n^2}{c^2} \varepsilon_{ii}^o - (k_o^{(i)} \sin \theta_o^{(i)} + n k_a)^2] \phi_n^{(i)}$$

$$= -\frac{1}{2} \frac{\omega_n^2}{c^2} R_{ik}(y)[e^{+jh_{ik}(y)} \phi_{n-1}^{(k)} + e^{-jh_{ik}(y)} \phi_{n+1}^{(k)}] \tag{2.47}$$

in which i and k may take on the values 2 and 3. If the diffracted light is of the same polarization as the incident light, which is always the case in Raman-Nath scattering, i = k. In Bragg scattering, if the incident light and diffracted light are of orthogonal polarization, $i \neq k$. When $i \neq k$, Eq. (2.47) represents a coupled set of partial differential equations. When i = k the equations decouple.

As was mentioned earlier, the field $\vec{E}$ associated with the incident light can always be decomposed into components along the principal axes of the unperturbed crystal. Each component can then undergo acousto-optic scattering via Eq. (2.47), and the results for the separate incident polarization components linearly superimpose. It is therefore only necessary to consider the case in which the incident light is polarized along the x_p axis, where p is 2 or 3. Designating by q the orthogonal axis, the boundary conditions we impose at x = 0 are

$$\Phi_o^{(p)}(o,y) = D \tag{2.48a}$$

$$\Phi_m^{(p)}(o,y) = 0 \quad , \quad (m = \pm 1, \pm 2, \pm 3, \ldots) \tag{2.48b}$$

$$\Phi_n^{(q)}(o,y) = 0 \quad , \quad (n = 0, \pm 1, \pm 2, \ldots) \tag{2.48c}$$

where a uniform plane plane with amplitude D for the p-polarized component has been assumed.

We proceed now to further simplify Eq. (2.47) before separately investigating the special cases of Raman-Nath and Bragg

diffraction. The equation, although linear, has nonconstant coefficients and consequently is not separable in the variables x and y. However, because no mechanism for loss has been introduced in our analysis, which could give rise to spatial amplitude modulation of the light, the predominant effect of the y-derivative is to introduce a phase variation in the y-direction. The effect of such phase variation would be to introduce spreading in the y-direction of the output light beam. It should be pointed out that in all applications reported in the following chapter, all the light in a given diffraction order is collected by the photodetector. Any variation in the y-direction is not important; only the total integral of the light intensity taken over the face of the detector is of practical interest. Because of this integration, only the average value of the acoustic wave amplitude taken in the region over which the light interacts is significant in determining the measured light diffracted into each order. In any application, what is measured by the photodetector is an effective value of the permittivity's perturbation for some interval Δy.

We now obtain solutions to Eq. (2.47) subject to the boundary constraints (2.48). We investigate first the case in which the polarization of the light is not rotated as a result

of the acousto-optic interaction, i = k. Defining $F_n^{(i)}(x,y)$ by

$$F_n^{(i)}(x,y) = e^{-j\,n\,\frac{\pi}{2}}\; e^{-j\,n\,h_{ii}(y)}\; \Phi_n^{(i)}(x,y), \tag{2.49}$$

employing Eq. (2.31) and neglecting the y-derivative, Eq. (2.47) is transformed into an ordinary differential equation in which y appears as a parameter.

$$2\,j\,k_o^{(i)} \cos\theta_o^{(i)} \frac{d\,F_n^{(i)}}{dx} + \left[\left(k_o^{(i)} \cos\theta_o^{(i)}\right)^2 - \frac{\omega_n^2}{c^2}\,\varepsilon_{ii}^o + \left(k_o^{(i)} \sin\theta_o^{(i)} + n\,k_a\right)^2\right] F_n^{(i)}$$

$$= j\,\frac{1}{2}\,\frac{\omega_n^2}{c^2}\,R_{ii}(j)\left[F_{n+1}^{(i)} - F_{n-1}^{(i)}\right] + \frac{d^2}{dx^2}\,F_n^{(i)} \tag{2.50}$$

With the change of variable

$$\eta = \frac{1}{2}\,\frac{\omega_n^2}{c^2}\,R_{ii}(y)\left[k_o^{(i)} \cos\theta_o^{(i)}\right]^{-1} x \quad , \tag{2.51}$$

Eq. (2.50) becomes

$$2\,\frac{d\,M_n^{(i)}}{d\eta} + \left[M_{n-1}^{(i)} - M_{n+1}^{(i)}\right] = j\,L_n^{(i)}\,M_n^{(i)} \tag{2.52}$$

in which $M_n^{(i)}$ and $L_n^{(i)}$ are defined by

$$M_n^{(i)}(\eta) = F_n^{(i)}(x,y) \tag{2.53}$$

and

$$L_n^{(i)} = \frac{2}{R_{ii}(y)} \frac{c^2}{\omega_n^2} [(k_o^{(i)} \cos \theta_o^{(i)})^2 - \frac{\omega_n^2}{c^2} \varepsilon_{ii}^o$$

$$+ (k_o^{(i)} \sin \theta_o^{(i)} + n k_a)^2] \tag{2.54}$$

To facilitate comparison of our results with those of other authors we define $Q^{(i)}$ and $\beta^{(i)}$ by

$$Q^{(i)} = \frac{k_a^2 L}{n^{(i)} k_{o_f}} \tag{2.55}$$

and

$$\beta^{(i)} = - \frac{n^{(i)} k_{o_f} \sin \theta_o^{(i)}}{k_a} \quad , \tag{2.56}$$

in which L is the interaction length in the medium, $0 \leq x \leq L$, as shown in Fig. 2.1. Using Eq. (2.41) we can write

$$L_n^{(i)} \simeq \frac{2n^{(i)}}{R_{ii}(y) k_{o_f}} \frac{n Q^{(i)}}{L} [(n - 2 \beta^{(i)})] \tag{2.57}$$

Klein and Cook,[15] in considering the acousto-optic interaction in an isotropic medium supporting bulk acoustic waves, show that the Raman-Nath and Bragg regimes correspond to the extreme cases $Q^{(i)} << 1$ and $Q^{(i)} >> 1$, respectively. Similar schemes for differentiating between the two cases have been proposed by Willard[69] and Extermann and Wannier.[70] Klein and Cook investigate these cases analytically and provide

numerical solutions for the transition region, $Q^{(i)} \gtrsim 1$. For the case of a bulk wave, $R_{ii}(y)$ = constant, Eq. (2.52) reduces to the set of coupled-mode equations first derived by Raman and Nath.[12]

In Raman-Nath diffraction, for even modest non-normal angles of incidence, $\beta^{(i)}$ can be very large, with the result that $L_n^{(i)}$ can be written as

$$L_n^{(i)} \gtrsim \frac{4\, n^{(i)}\, n\, Q^{(i)}\, \beta^{(i)}}{L\, R_{ii}(y)\, k_{o_f}} \tag{2.58}$$

In terms of the quantities k_a, k_{o_f}, and $\sin \theta_{o_f}$, this is given by

$$L_n^{(i)} \gtrsim \frac{4\, n \sin \theta_{o_f}\, k_a}{R_{ii}(y)\, k_{o_f}} \quad . \tag{2.59}$$

Substituting Eq. (2.59) into (2.52), and using the two Bessel function identities

$$2\, J_n'(x) = J_{n-1}(x) - J_{n+1}(x) \tag{2.60}$$

and

$$J_{n-1}(x) + J_{n+1}(x) = \frac{2n}{x}\, J_n(x) \tag{2.61}$$

it follows that

$$M_n^{(i)}(\eta) = A \exp\left[j \frac{\sin \theta_{o_f}\, k_a}{R_{ii}(y)\, k_{o_f}}\, \eta\right] J_n\left[\frac{R_{ii}(y)\, k_{o_f}}{\sin \theta_{o_f}\, k_a} \sin\left(\frac{\sin \theta_{o_f}\, k_a}{k_{o_f}\, R_{ii}(y)}\, \eta\right)\right] \tag{2.62}$$

in which the constant A is determined from Eq. (2.48)

$$A = D \tag{2.63}$$

In the limiting case of a bulk wave, $R_{ii}(y)$ = constant, the result is of the same for as given by Klein and Cook.

The intensity of the n^{th} diffraction order is

$$I_n^{(i)} = \delta_{ip} D^2 J_n^2 \left[\frac{R_{ii}(y)\, k_{o_f}}{\sin \theta_{o_f}\, k_a} \sin \left(\frac{\sin \theta_{o_f}\, k_a}{k_{o_f}\, R_{ii}(y)}\ \eta\right)\right] \tag{2.64}$$

At x = L, this reduces in the case of normal incidence to

$$I_n^{(i)} = \delta_{ip} D^2 J_n^2 \left[\frac{1}{2} R_{ii}(y)\ \frac{k_{o_f}}{h^{(i)}}\ L\right] \tag{2.65}$$

Using the expansion for integral order Bessel functions of small argument,

$$J_m(a) \sim \frac{1}{m!} \left(\frac{a}{2}\right)^m , \quad a \ll 1 , \tag{2.66}$$

the first order intensity, normalized to the incident light, is given by

$$\frac{I_1^{(i)}}{D^2} = \delta_{ip} \frac{1}{16} \left[R_{ii}(y)\ \frac{k_{o_f}}{n^{(i)}}\ L\right]^2 \tag{2.67}$$

A result analogous to Eq. (2.67) has previously been given by Kramer,[71] arrived at by analogy to the Raman-Nath diffraction in bulk waves using a physical argument. His theory, however, assumed an acoustically isotropic material and did not take the electro-optic contribution into explicit account.

In any physical experiment the photodetector gives a signal proportional to the integral of the light intensity taken

over the detector's active area. The geometry for an idealized acousto-optic experiment is shown in Fig. 2.2. The laser beam of width w in the y-direction interacts in the lithium niobate a depth h from the surface. All light in a given order is collected by a photodiode after focusing by a lens. Thus the photodiode output is given by

$$V_{out} = C_d \int_{-\infty}^{\infty} \text{rect}\left(\frac{h - y}{w}\right) I_n^{(i)}(L,y)\, dy \quad , \tag{2.68}$$

in which a uniform plane wave of width w has been assumed, and C_d is a constant of proportionality which characterizes the detector, given by the product of the photoelectric conversion factor, subsequent amplification, and load resistance. The *sampling function is defined by*

$$\text{rect}(x) = \begin{cases} 1 & |x| \leq \frac{1}{2} \\ 0 & |x| > \frac{1}{2} \end{cases} \tag{2.69}$$

Effects such as boundary reflections, cone-angle due to lens focusing, and Gaussian laser beam profile will modify Eq. (2.68). Cone-angle and Gaussian profile characteristics can be taken into account by properly defining h and w and have been treated in previous work.[71] Boundary reflections can be eliminated by proper index matching. From Eqs. (2.68) and (2.69), light in the first diffracted order will produce the following photodiode signal:

$$V_{out} = C_d D^2 \frac{1}{16} \left[\frac{k_{o_f}}{n^{(p)}} L\right]^2 \int_{-\infty}^{\infty} \text{rect}\left(\frac{h - y}{w}\right) \left[R_{pp}(y)\right]^2 dy \qquad (2.70)$$

Following the method of Klein and Cook, we now investigate Eq. (2.52) for the case of Bragg diffraction in which the incident and diffracted beam are of the same polarization. Unlike the Raman-Nath case we now seek a solution for which only one diffraction order is nonvanishing. For light to appear in some single order other than the zero, that order must be synchronous with the zero order. Thus the right hand side of Eq. (2.52) must have the same value for the diffracted order as for the zero order. Equation (2.57) provides that the right hand side is zero for this order. If the first order, n = 1, is to be synchronous with the zero order, we must insist that

$$\beta^{(i)} = \frac{1}{2} \qquad (2.71)$$

For n = -1, we must have $\beta^{(i)} = -1/2$; for a synchronous second order, $\beta^{(i)} = 1$. A condition can be imposed upon $\beta^{(i)}$ to make $L_n^{(i)}$ vanish for any desired order. It should be recalled, however, that only adjacent modes are coupled by the differential equation. Thus $\beta^{(i)} = \pm 1$ is unacceptable. $\phi_o^{(i)}$ and $\phi_{\pm 2}^{(i)}$ are not directly coupled. Moreover, the order through which the zero and second orders are coupled, the first order, is synchronous with neither if we take $\beta^{(i)} = 1$. The case given by Eq. (2.71) in which the zero and first orders are coupled, meets all criteria.

It is satisfying that this equation is equivalent to Eq. (2.44) derived earlier in describing Bragg scattering.

With only $M_o^{(p)}(\eta)$ and $M_1^{(p)}(\eta)$ nonvanishing, Eq. (2.46) provides the system of coupled mode equations

$$2 \frac{d M_o^{(p)}}{d\eta} - M_1^{(p)} = 0 \tag{2.72}$$

$$2 \frac{d M_1^{(p)}}{d\eta} + M_o^{(p)} = 0 \tag{2.73}$$

Solutions, subject to the boundary condition (2.48), are

$$M_o^{(p)} = D \cos \left(\frac{1}{2} \eta\right) \tag{2.74}$$

$$M_1^{(p)} = -D \sin \left(\frac{1}{2} \eta\right) \tag{2.75}$$

In terms of the original quantities, the intensities at $x = L$ are given by

$$I_o^{(p)} = D^2 \cos^2 \left(\frac{1}{4} R_{pp}(y) \frac{k_{o_f}}{n^{(p)}} L\right) \tag{2.76}$$

$$I_1^{(p)} = D^2 \sin^2 \left(\frac{1}{4} R_{pp}(y) \frac{k_{o_f}}{n^{(p)}} L\right) \tag{2.77}$$

The approximation $\omega_a << \omega_n$ was used in writing Eqs. (2.76) and (2.77). Again, in the limiting case of a bulk wave, the solutions agree with previously published results.[72] With $\sin(\alpha) \simeq \alpha$ for small α, Eq. (2.77) reduces in the case of low acoustic power to

$$I_1^{(p)} = D^2 \frac{1}{16} \left[R_{pp}(y) \frac{k_{o_f}}{n^{(p)}} L\right]^2 . \tag{2.78}$$

Comparison of Eqs. (2.78) and (2.67) shows that the first order diffraction profile is independent of whether the diffraction occurs in the Bragg or Raman-Nath regime.

As was previously indicated, at high acoustic frequencies it is possible that the polarization of the Bragg diffracted light is rotated from that of the zero order. The procedure for determining the intensity of the diffracted order is exactly as that employed above, except that in this case $R_{pp}(y)$ is replaced by $R_{pq}(y)$. Thus, when polarization rotation occurs,

$$I_o^{(p)} = D^2 \cos^2 \left(\frac{1}{4} R_{pq}(y) \frac{k_{o_f}}{n^{(p)}} L\right) \tag{2.79}$$

$$I_1^{(q)} = D^2 \sin^2 \left(\frac{1}{4} R_{pq}(y) \frac{k_{o_f}}{n^{(q)}} L\right) \tag{2.80}$$

2.6 Numerical Results

The theory of the acousto-optic interaction in surface acoustic waves has been developed in the preceding sections of this chapter. In this section we evaluate the obtained expressions for the special case of a z-propagating Rayleigh wave on y-cut lithium niobate. The form of the Rayleigh wave as given by Spaight and Koerber[68] is

$$u_2 = B_a \left(e^{-j\alpha_1 k_a y} + m_{21} e^{-j\alpha_2 k_a y} + m_{31} e^{-j\alpha_3 k_a y}\right) e^{4j(\omega_a t - k_a z)}$$

$$u_3 = B_a N\left(e^{-j\alpha_1 k_a y} + n_{21} e^{-j\alpha_2 k_a y} + n_{31} e^{-j\alpha_3 k_a y}\right) e^{j(\omega_a t - k_a z)}$$

$$e_2 = B_a k_a O\left(e^{-j\alpha_1 k_a y} + a_{21} e^{-j\alpha_2 k_a y} + a_{31} e^{-j\alpha_3 k_a y}\right) e^{j(\omega_a t - k_a z)}$$

$$e_3 = B_a k_a P\left(e^{-j\alpha_1 k_a y} + b_{21} e^{-j\alpha_2 k_a y} + b_{31} e^{-j\alpha_3 k_a y}\right) e^{j(\omega_a t - k_a z)}$$

$$e_1 = u_1 = 0, \; y \geq 0 \qquad (2.81)$$

Parameters given in these equations are provided in Table 2.1.

Table 2.2 below provides numberical values for the parameters which optically characterize lithium niobate. A few comments are in order regarding several of the constants listed. First, the usual convention has been employed in which certain sets of subscripted indices are given in a contracted notation.[16] The sets i,j and kℓ appearing in $P_{ijk\ell}$ and r_{ijm} (i,j,k, = 1,2,3) are replaced by a single index with values 1,2,3,...,6. Thus $P_{ijk\ell}$ becomes P_{IJ} and r_{ijm} becomes r_{Im}.

i,j =	I =
11	1
22	2
33	3
23 or 32	4
13 or 31	5
12 or 21	6

TABLE 2.1

Rayleigh Wave Parameters for YZ $LiNbO_3$ [68]

Symbol	Value	Description
v_a	3.5105×10^3 m/sec	Phase Velocity
α_1	0.06462 - j 0.1217	Decay Constants
α_2	0.3804 - j 1.0379	
α_3	-0.3960 - j 0.7738	
N	-0.05180 + j 0.09717	Wave Amplitude Coefficients
O	$(-0.1826 + j\ 0.1402) \times 10^9$	
P	$(-1.5202 - j\ 0.6931) \times 10^9$	
m_{21}	-0.02637 + j .3719	
m_{31}	0.02740 - j 0.5141	
n_{21}	-1.9258 + j 5.0939	
n_{31}	-4.1164 - j 1.4533	
a_{21}	-32.435 - j 22.191	
a_{31}	27.233 + j 19.453	
b_{21}	-3.6274 - j 3.2912	
b_{31}	-0.05632 + j 5.3042	

TABLE 2.2

Optical Properties of $LiNbO_3$

Symbol	Value	Description
$\varepsilon_{11}^{o} = \varepsilon_{22}^{o}$	5.24	Unperturbed Relative Permittivity[13]
ε_{33}^{o}	4.84	
$P_{11} = P_{22}$	-.02	Elasto-Optic Tensor Element[27]
$P_{12} = P_{21}$	.08	
$P_{13} = P_{23}$	$.13\ e^{j\pi}$ *	
$P_{14} = -P_{24} = P_{65}$	-.08	
$P_{31} = P_{32}$	.17	
P_{33}	.07	
$P_{41} = -P_{42} = P_{56}$	-.15	
$P_{44} = P_{55}$	.12	
r_{33}	$30.8 \times 10^{-2}\ e^{j(-.125\pi)}$ m/V*	Electro-Optic Tensor Element[73]
$r_{22} = -r_{12} = -r_{61}$	3.4×10^{-12} m/V	
$r_{13} = r_{23}$	8.6×10^{-12} m/V	
$r_{51} = r_{42}$	28×10^{-12} m/V	

*modified value

The values employed for the elasto-optic coefficients at constant electric field and electro-optic coefficients at constant strain were those given by Pinnow[27] and Kaminow[73] respectively. It was found in calculating $\Delta\varepsilon_{ij}$ from these constants using Spaight and Koerber data for the Rayleigh wave, numerical discrepancies existed with $\Delta\varepsilon_{ij}$ calculated using Dixon's[19,74] effective elasto-optic coefficients which include both electro- and elasto-optic contributions. This discrepancy was minimized by introducing a phase factor on some of the constants, which is reflected in Table 2.2. This resulted in good agreement with experimental results of Kramer.

With reference to Tables 2.1 and 2.2 and Eqs. (2.10) and (2.38),

$$f_{min} = 497 \text{ MHz} \quad , \tag{2.82}$$

assuming $\lambda_{o_f} = 6328$ Å. This frequency was not approached in any of the experiments reported here.

Table 2.3 gives the calculated values of the coefficients appearing in Eq. (2.18). Coefficients for the elasto-optic, electro-optic, and combined effects are provided. Based on these coefficients, the function $[R_{ij}(y)]^2$ is calculated. The intensity profile for light in the first diffraction order is proportional to this function, assuming low acoustic power. Results are shown graphically in Figs. 2.3, 2.4, and 2.5.

TABLE 2.3

Calculated Coefficients for the Perturbed Relative Permittivity

	Y-Polarization	Z-Polarization	Rotated Polarization*
Elasto-Optic Contribution	$c_{22}^{(1)s} = 1.557 \times 10^{-2} - j\ 3.231 \times 10^{-2}$	$c_{33}^{(1)s} = 2.749 \times 10^{-2} - j\ 1.461 \times 10^{-2}$	$c_{23}^{(1)s} = -1.750 \times 10^{-2} - j\ 7.020 \times 10^{-2}$
	$c_{22}^{(2)s} = 4.857 \times 10^{-2} + j\ 8.471 \times 10^{-2}$	$c_{33}^{(2)s} = -.6026 \times 10^{-2} + j\ 9.158 \times 10^{-2}$	$c_{23}^{(2)s} = 4.547 \times 10^{-2} - j\ 1.770 \times 10^{-2}$
	$c_{22}^{(3)s} = -7.226 \times 10^{-2} - j\ 3.967 \times 10^{-2}$	$c_{33}^{(3)s} = -5.373 \times 10^{-2} - j\ 9.429 \times 10^{-2}$	$c_{23}^{(3)s} = -1.223 \times 10^{-2} + j\ 8.317 \times 10^{-2}$
Electro-Optic Contribution	$c_{22}^{(1)e} = -1.369 \times 10^{-2} - j\ 5.483 \times 10^{-3}$	$c_{33}^{(1)e} = -4.682 \times 10^{-2} - j\ 2.135 \times 10^{-2}$	$c_{23}^{(1)e} = -5.113 \times 10^{-2} + j\ 3.926 \times 10^{-2}$
	$c_{22}^{(2)e} = 5.852 \times 10^{-2} + j\ 6.297 \times 10^{-2}$	$c_{33}^{(2)e} = 9.958 \times 10^{-2} - j\ 2.315 \times 10^{-1}$	$c_{23}^{(2)e} = 2.529 \times 10^{-2} - j\ 1.387 \times 10^{-2}$
	$c_{22}^{(3)e} = 6.173 \times 10^{-3} - j\ 6.810 \times 10^{-2}$	$c_{33}^{(3)e} = -1.000 \times 10^{-2} - j\ 1.092 \times 10^{-2}$	$c_{23}^{(3)e} = -2.156 \times 10^{-2} + j\ 7.447 \times 10^{-3}$

Table 2.3 (Cont.)

	Y-Polarization	Z-Polarization	Rotated Polarization*
Combined Effect	$C_{22}^{(1)} = 1.882 \times 10^{-3} - j\ 3.779 \times 10^{-2}$	$C_{33}^{(1)} = -1.933 \times 10^{-2} - j\ 6.737 \times 10^{-2}$	$C_{23}^{(1)} = -2.261 \times 10^{-2} - j\ 6.628 \times 10^{-2}$
	$C_{22}^{(2)} = 9.947 \times 10^{-3} + j\ 1.476 \times 10^{-2}$	$C_{33}^{(2)} = 3.932 \times 10^{-2} - j\ 1.399 \times 10^{-1}$	$C_{23}^{(2)} = 2.984 \times 10^{-1} - j\ 3.158 \times 10^{-2}$
	$C_{22}^{(3)} = 6.609 \times 10^{-2} - j\ 1.078 \times 10^{-1}$	$C_{33}^{(3)} = -6.373 \times 10^{-2} - j\ 1.052 \times 10^{-1}$	$C_{23}^{(3)} = -2.278 \times 10^{-1} + j\ 9.062 \times 10^{-2}$

*Coefficients for (i,j) = (3,2) are the same as for (2,3).

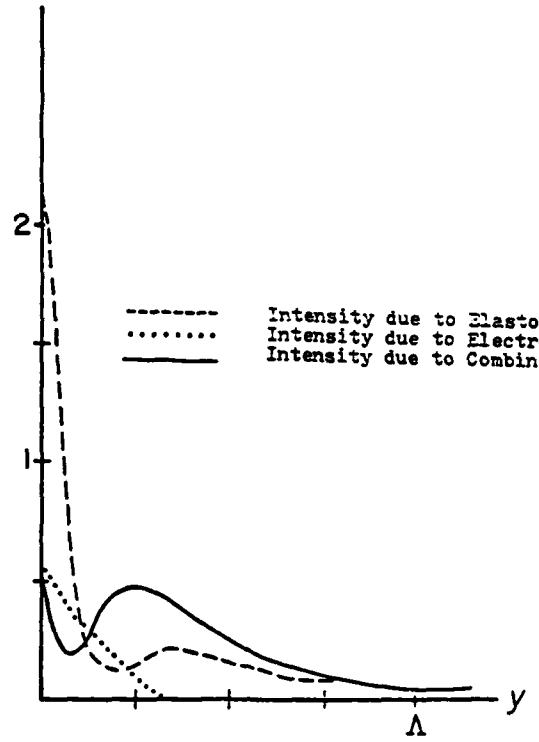

Fig. 2.3 Intensity for Y-Polarized Light

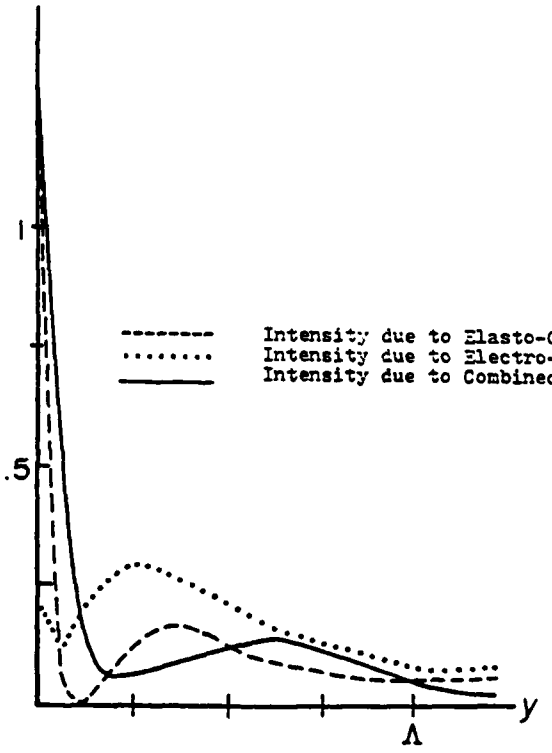

Fig. 2.4 Intensity for Z-Polarized Light

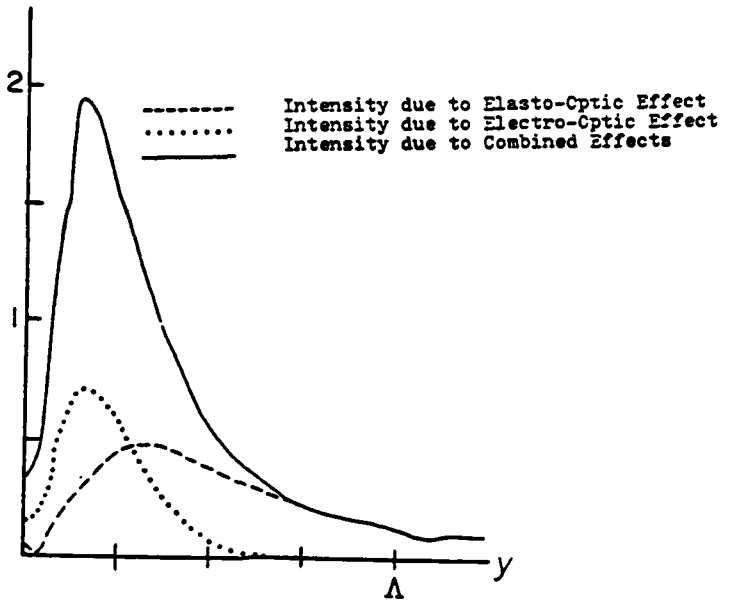

Fig. 2.5 Intensity for Light Rotated from Y-Polarized to Z-Polarized

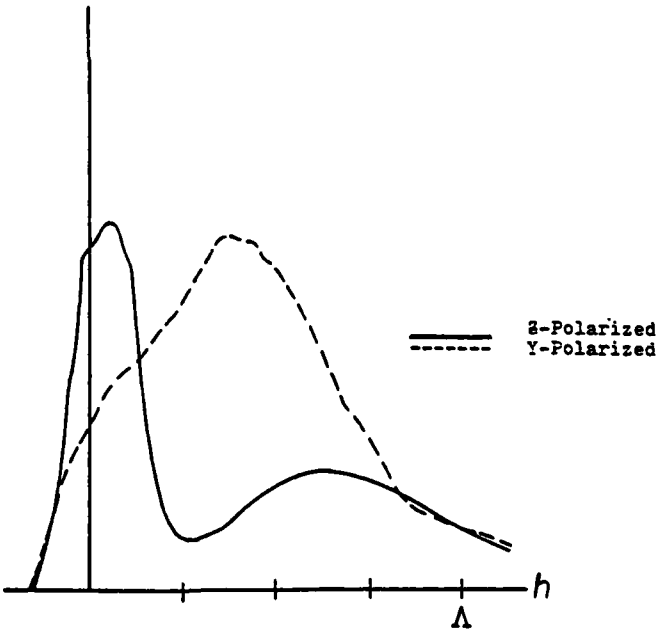

Fig. 2.6 Comparison of Scattering Profiles for Y- and Z-Polarized Light

Integration Width: .26Λ

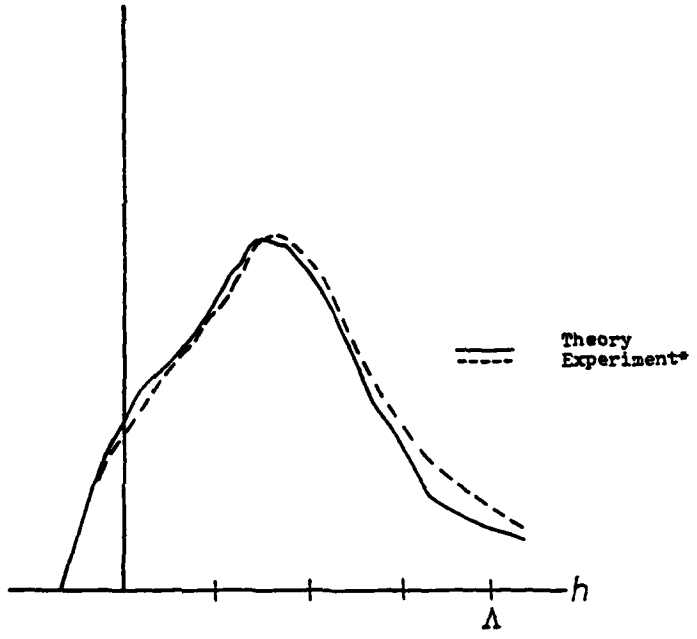

Fig. 2.7 Comparison of Experimental and Theoretical Results for Y-Polarization

*From Kramer, ref. (71)

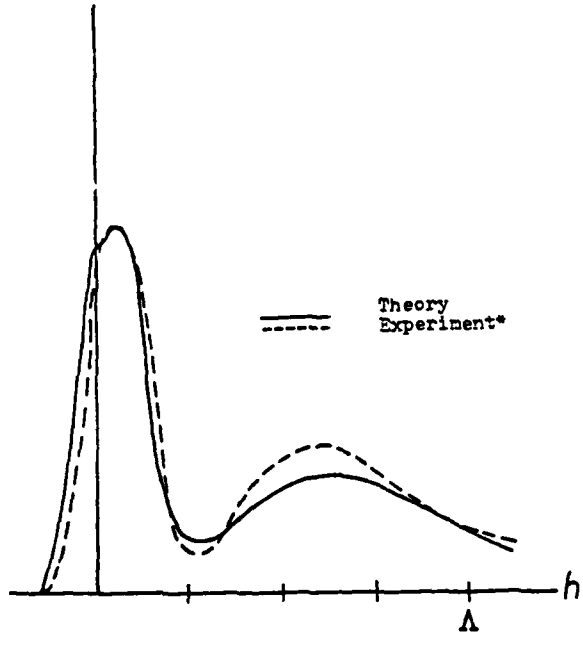

Fig. 2.8 Comparison of Experimental and Theoretical Results for Z-Polarization

*From Kramer, ref. (71)

Figures 2.3 and 2.4 have obvious implications to integrated optics structures fabricated on lithium niobate. Those devices employing z-polarized light require very shallow waveguides, less than oneeighth of an acoustic wavelength, for example. In this category are all those devices fabricated by out-diffusion of Li_2O from the surface, since this process chiefly effects the extraordinary refractive index and therefore provides waveguiding for z-polarized light. On the other hand, for devices which can make use of y-polarized light a deeper guide, extending to about one third of an acoustic wavelength, would take better advantage of the available acoustic power. A buried waveguide would be most advantageous in this case.

Figure 2.6 shows the integrating effect of a finite beam width, as discussed in connection with Eq. (2.68). The integral

$$\int_{-\infty}^{\infty} \text{rect}\left(\frac{h - y}{w}\right) I_n^{(I)}(L,y)dy \quad , \quad \text{divided by } (D\, B_a\, k_a)^2 \quad ,$$

is shown in the figure for I = 2,3 (contracted notation). The solid line indicates z-polarized light; the dashed line is for the y-polarization. The trapezoidal integration technique was used in generating these curves. Sixteen intervals were utilized spanning a total width w = .255 Λ. As noted earlier, the diffraction effect is more pronounced near the surface for z-polarized light. Further from the surface the diffraction of y-polarized light is stronger. These calculated results are superimposed upon the experimental results of Kramer in Figs. 2.7 and 2.8, with good agreement. In

Fig. 2.7 it was necessary to translate Kramer's curve approximately .08 Å toward the surface in order to have the maxima of the two curves coinciding. This is probably within his experimental resolution in determining the crystal surface position with the optical probe he used.

CHAPTER 3

ACOUSTO-OPTIC INTERACTION IN SURFACE ACOUSTIC WAVES: DEVICE APPLICATIONS

3.1 Unified Description of Acousto-Optic Devices

In this section we develop a description of acousto-optic devices which can be applied to the operational analysis of such varied devices as modulators, signal processors, and image scanners. The description, which is appropriate to both bulk and surface wave devices, is developed for an interaction in the Raman-Nath regime.

Consider the one-dimensional optical system shown in Fig. 3.1. A uniform plane wave is amplitude modulated by the transmittance function $T(\zeta)$ which is imaged via lens L_1 into the z-plane, where it appears as $T(z)$. Depending on the placement of L_1 the imaging process could involve magnification. Since $T(z)$ is spatially limited we can consider an aperture of width ℓ, $\ell \leq d$, positioned in the z-plane of the diffraction limited system. Voltages $f_1(t)$ and $f_2(t)$ amplitude modulate rf carriers at the acoustic frequency ω_a which excite transducers at opposite ends of the ultrasonic delay line. It is assumed throughout that the time rates of change of $f_1(t)$ and $f_2(t)$ are small compared to that of the rf carrier. These signals produce traveling optical phase gratings which diffract the incident light. The Fraunhofer diffraction pattern is formed in the z'-plane, which is the focal plane of lens L_2.

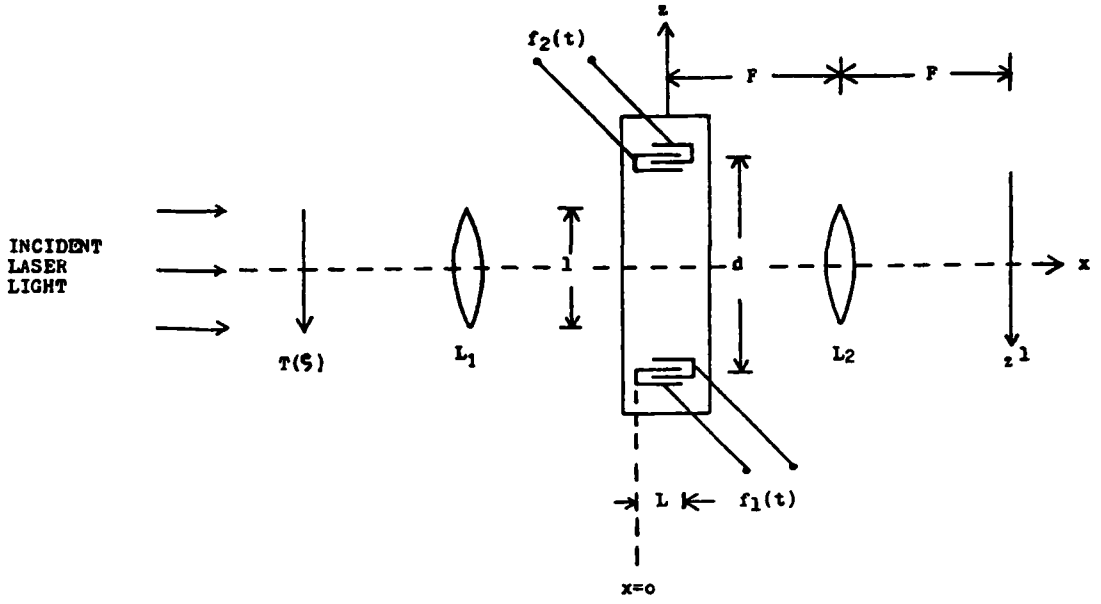

Fig. 3.1 Geometry for Acousto-Optic Device Model

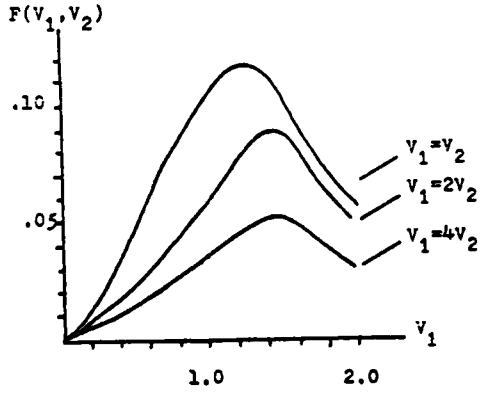

Fig. 3.2 Calculated Convolver Peak Response for Constant Amplitude Input

$$F(V_1,V_2) = J_1(V_1)J_1(V_2)\left[J_0(V_1)J_0(V_2)+J_2(V_1)J_2(V_2)\right]$$

The amplitude distribution of the diffracted light is given by the diffraction integral

$$A(\theta) = C\, e^{j\omega t} \int_{-\ell/2}^{\ell/2} T(z)\, e^{j\left[\frac{2\pi}{\lambda_{o_f}} \sin\theta + V_1 \left(v_a t - z - \frac{d}{2}\right) \sin\left(\omega_a t - k_a z\right)\right.}$$

$$\left. + V_2 \left(v_a t + z + \frac{d}{2}\right) \sin\left(\omega_a t + k_a z\right)\right]$$

$$dz \quad , \tag{3.1}$$

in which C is a normalizing constant, ω is the frequency of the incident light, λ_{o_f} is the free space wavelength of the incident light, the angle θ is measured from the x-axis, v_a is the acoustic velocity given by ω_a/k_a, and the spatial functions V_1 and V_2 are proportional to the applied voltages $f_1(t)$ and $f_2(t)$. In particular, with respect to a common point of insertion,

$$V_1(v_a t) = \frac{2\pi Lb}{\lambda_{o_f}} f_1(t) \tag{3.2}$$

and

$$V_2(v_a t) = \frac{2\pi Lb}{\lambda_{o_f}} f_2(t) \quad , \tag{3.3}$$

in which b is a constant which takes into account material photo-elastic constants and transducer electro-mechanical coupling. Although Eq. (3.1) is the diffraction integral of scalar diffraction theory, we interpret $A(\theta)$ as a component of the electric field of the diffracted light.

Using the identity

$$e^{j\alpha\sin\beta} = \sum_{r=-\infty}^{\infty} J_r(\alpha)\, e^{jr\beta} \quad , \tag{3.4}$$

in which J_r is the r^{th} order Bessel function of the first kind, Eq. (3.1) becomes

$$A(\theta) = C\, e^{j\omega t} \int_{-\ell/2}^{\ell/2} T(z) \sum_s \sum_r J_r\,[V_1(v_a t - z - d/2)]\, J_s\,[V_2(v_a t + z + d/2)]$$

$$\times\, e^{j[\frac{2\pi}{\lambda_{o_f}} \sin\theta\, z + (r+s)\,\omega_a t + (s-r)\,k_a z]}\, dz \tag{3.5}$$

Assuming uniform convergence of both series, the order of integration and summation can be exchanged. Letting $n = r - s$, Eq. (3.5) becomes

$$A(\theta) = C\, e^{j\omega t} \sum_n \sum_r \int_{-\ell/2}^{\ell/2} T(z)\, J_r[V_1(v_a t - z - d/2)]\, J_{r-n}[V_2(v_a t + z + d/2)]$$

$$\times\, e^{j[(2r-n)\,\omega_a t + (\frac{2\pi}{\lambda_{o_f}} \sin\theta - n\,k_a)z]}\, dz \tag{3.6}$$

For ideal diffraction, $\ell \to \infty$, and the integral has nonvanishing values only for

$$\frac{2\pi}{\lambda_{o_f}} \sin\theta - n\,k_a = 0 \quad , \tag{3.7}$$

which means that light occurs only at discrete angles θ_n given by

$$\sin \theta_n = \frac{n \lambda_{o_f}}{\Lambda} \quad . \tag{3.8}$$

In this case the light in the z'-plane appears as δ-functions at the points

$$z'_n \simeq F \sin \theta_n = \frac{n F \lambda_{o_f}}{\Lambda} \tag{3.9}$$

In the physical case in which the aperture ℓ is finite, diffraction spreading of these spots occurs, the width of each spot given approximately by $F \lambda_{o_f} / \ell$.

The amplitude of the light in the n^{th} diffracted order is given by

$$A_n = C \sum_r e^{j[(2r-n)\omega_a + \omega]t} \int_{-\ell/2}^{\ell/2} T(z)\, J_r[V_1(v_a t - z - d/2)]$$

$$J_{r-n}\,[V_2(v_a t + z + d/2)]\, dz \tag{3.10}$$

The time dependent intensity in the n^{th} order is given by

$$I_n = A_n A_n^*$$

$$= C^2 \sum_r \sum_p e^{j2(r-p)\omega_a t} \int_{-\ell/2}^{\ell/2} T(z)\, J_r[V_1(v_a t - z - d/2)] J_{r-n}[V_2(v_a t + z + d/2)]\, dz$$

$$\times \int_{-\ell/2}^{\ell/2} T(z)\, J_p[V_1(v_a t - z - d/2)]\, J_{p-n}[V_2(v_a t + z + d/2)] dz \tag{3.11}$$

The time-averaged light intensity, taken over a time interval greater than several rf cycles but small compared to the time rate of change of $f_1(t)$ and $f_2(t)$, is

$$\bar{I}_n = C^2 \sum_{r=-\infty}^{\infty} \left| \int_{-\ell/2}^{\ell/2} T(z)\, J_r[V_1(v_a t - z - d/2)]\, J_{r-n}[V_2(v_a t + z + d/2)]\, dz \right|^2 \tag{3.12}$$

To relate Eq. (3.12) to the results of Chapter 2, we take $V_2 = 0$, and $T(z) = 1$, with the result that Eq. (3.12) becomes

$$\bar{I}_n = C^2 \left| \int_{-\ell/2}^{\ell/2} J_n\,[V_1(v_a t - z - d/2)]\, dz \right|^2 . \tag{3.13}$$

If $f_1(t)$ is constant with time, this can be further reduced to

$$\bar{I}_n = C^2\, \ell^2\, J_n{}^2\,(V_1) \tag{3.14}$$

The total time-averaged light intensity in the n^{th} order is obtained from the results of Chapter 2 by taking the integral over y of Eq. (2.65).

$$I_n{}^{(i)}{}_{\text{total}} = \int_{h-w/2}^{h+w/2} D^2\, J_n{}^2\, [\tfrac{1}{2} R_{ii}(y)\, \frac{k_{o_f}}{n^{(i)}}\, L]\, dy \tag{3.15}$$

Equation (3.15) represents the total light in the n^{th} order at x = L. Parseval's theorem provides that this is the same intensity that would appear in the n^{th} order in the z'-plane. The mean value theorem for integrals guarantees that there exists some value $y = \alpha$ in the interval $h - w/2 \le y \le h + w/2$ such that the integral of Eq. (3.15) can be written

$$I_n{}^{(i)}{}_{\text{total}} = w\, D^2\, J_n{}^2\, [\tfrac{1}{2} R_{ii}(\alpha)\, \frac{k_{o_f}}{n^{(i)}}\, L] . \tag{3.16}$$

A comparison of Equations (3.14) and (3.16) provides

$$C^2 = \frac{w D^2}{\ell^2} \tag{3.17}$$

and

$$V_1 = \frac{1}{2} R_{ii}(\alpha) \frac{k_{o_f}}{n^{(i)}} L \quad . \tag{3.18}$$

From Eq. (3.18) it is apparent that the constant b appearing in Eq. (3.2) is given by

$$b = \frac{1}{2} \frac{R_{ii}(\alpha)}{f_1 n^{(i)}} \quad , \tag{3.19}$$

which is a measure of the effectiveness of an applied voltage signal to produce a perturbation of the material's permittivity. We are now in a position to indicate several device applications of the acousto-optic interaction.

Modulator

The modulator is the simplest acousto-optic device. By varying the input voltage $f_1(t)$, the time-averaged light intensity of the various orders is controlled. With $f_2(t) = 0$ and $T(z) = 1$ in $-\ell/2 \leq z \leq \ell/2$, the intensity in the n^{th} order is given by Eq. (3.14). Using Eq. (3.2),

$$\bar{I}_n = \bar{I}_o J_n^2 [K f_1(t)] \quad , \tag{3.20}$$

in which K is a constant given by $2\pi L b/\lambda_{o_f}$. It should be recalled that Eq. (3.14) was derived under the assumption that V_1 was constant in the optical aperture region. Thus we require that the aperture ℓ

be small compared to the spatial rate of change of V_1. In terms of the angular frequency of the highest frequency component of $f_1(t)$, ω_{max}, we can express this requirement as

$$\ell < \frac{\pi v_a}{\omega_{max}} \quad , \tag{3.21}$$

in which the acoustic wavelength corresponding to ω_{max} is at least twice ℓ. For a signal with $\omega_{max} = 2\pi \times 1$ MHz, this requires ℓ to be less than 1.75 mm, which is a typical beam diameter for a low power HeNe laser.

Of particular interest is the case n = 1 for a small signal $f_1(t)$. In this case,

$$\bar{I}_1 \simeq \frac{1}{4} \bar{I}_o K^2 [f_1(t)]^2 \quad . \tag{3.22}$$

The first order diffracted light is proportional to the power of the input signal.

Image Scanner

With $f_2(t) = 0$, the configuration shown in Fig. 3.1 can be used to transform an intensity transmission function $\tau(\zeta) \equiv |T(\zeta)|^2$ into a voltage for the purpose of facsimile transmission. From Eq. (3.12),

$$\bar{I}_n = C^2 \left| \int_{-\ell/2}^{\ell/2} T(z) J_n[V_1 (v_a t - z - d/2)] \, dz \right|^2 \quad . \tag{3.23}$$

For small arguments of the Bessel function, the first order light is given by

$$\bar{I}_1 = C^2 \left| \int_{-\ell/2}^{\ell/2} T(z)\, V_1(v_a t - z - d/2)\, dz \right|^2 . \qquad (3.24)$$

Equation (3.24) can be interpreted as the square of the convolution of the spatial mask $T(z)$ with the acoustic signal V_1. If $f_1(t)$ is a very short rectangular pulse which amplitude modulates the rf carrier, then V_1 approximates the delta function, $\delta(v_a t - z - d/2)$. Thus the integral of Eq. (3.23) becomes

$$\bar{I}_1 = C^2 \left| T(v_a t - d/2) \right|^2$$

$$= C^2\, \tau(v_a t - d/2) \qquad (3.25)$$

As a function of time the intensity replicates the spatial information $\tau(\zeta)$. In practice V_1 need not be made small in amplitude. The pulse height is adjusted to maximize the first order Bessel function.

Convolver

It is apparent from Eq. (3.11) that the time dependent intensity in each diffraction order is made up of a sum of temporal frequency components occurring at even integral multiples of the acoustic rf frequency. Any given frequency component can be electronically isolated by proper filtering of the output signal of a photodetector placed to collect the light in a single diffraction order. The resultant signal, after filtering, provides the real-time convolution of $f_1(t)$ and $f_2(t)$. We illustrate this for the

case of light in the zero order at twice the acoustic frequency, but a similar analysis can be applied to obtain real-time convolution in any order at any even multiple of acoustic frequency.

In the special case that $f_1(t)$ and $f_2(t)$ are time limited signals,

$$f_1(t),\ f_2(t) = 0 \qquad \text{for } t < 0,\ t > d/v_a, \tag{3.26}$$

and $T(z)$ is a simple window function,

$$T(z) = \begin{cases} 1 & |z| \leq d/2 \\ 0 & |z| > d/2 \end{cases}, \tag{3.27}$$

the limits of integration for all integrals appearing in Eq. (3.11) can be taken from $-\infty$ to ∞ without affecting the value of the integrals. With $n = 0$ for the zero order diffracted light, and $(r - p) = 1$ corresponding to the component at twice the acoustic frequency, Eq. (3.11) provides, after rearrangement of terms,

$$\begin{aligned} I_o^{(2\omega_a)} = 2C^2 \{ & \int_{-\infty}^{\infty} J_1[V_1(v_a t - z - d/2)]\ J_1[V_2(v_a t + z + d/2)]\ dz \} \\ & \times \{ \int_{-\infty}^{\infty} J_o[V_1(v_a t - z - d/2)]\ J_o[V_2(v_a t + z + d/2)]\ dz \\ & + \int_{-\infty}^{\infty} J_2[V_1(v_a t - z - d/2)]\ J_2[V_2(v_a t + z + d/2)]\ dz \} \\ & + (\text{higher order terms}) \quad , \end{aligned} \tag{3.28}$$

in which terms involving sixth and higher order products have been neglected. The function $J_1(V_1)\, J_1(V_2)\, [J_o(V_1)\, J_o(V_2) + J_2(V_1)\, J_2(V_2)]$ is plotted in Fig. 3.2 for various standing wave ratios V_1/V_2. For small arguments of the Bessel functions, Eq. (3.28) becomes

$$I_o^{(2\omega_a)} \simeq \frac{1}{2} C^2 d \int_{\infty}^{\infty} V_1(v_a t - z - d/2)\, V_2(v_a t + z + d/2)\, dz \quad . \tag{3.29}$$

With the substitution $v_a \tau = v_a t - z - d/2$, Eq. (3.29) reduces to the familiar convolution integral. In terms of the voltage signals $f_1(t)$ and $f_2(t)$,

$$I_o^{(2\omega_a)} \simeq \frac{2\pi^2 L^2 b^2}{\lambda_{o_f}^2} C^2 d \int_{-\infty}^{\infty} f_1(\tau)\, f_2(2t - \tau)\, d\tau \quad . \tag{3.30}$$

An interesting feature of Eq. (3.30) is the time-compression factor of two which arises from the fact that both functions V_1 and V_2 are propagating in opposite directions along the acoustic track. In the usual convolution integral, one function is considered fixed with respect to the coordinate system while the other is shifted with respect to it.

The analog convolver is a powerful signal processor because of its great flexibility. If the two input carrier frequencies are not identical, and if $f_2(t)$ is an even function of time, then the modulating factor of the output frequency $2(\omega_a - \Delta\omega_a)$ is proportional to the cross-ambiguity function of f_1 and f_2:

$$I_o^{[2(\omega_a - \Delta\omega_a)]} = \int_{-\infty}^{\infty} f_1(\tau)\, f_2(\tau - 2t)\, e^{j\Delta\omega_a \tau}\, d\tau \quad , \tag{3.31}$$

In the case that $\Delta\omega_a = 0$, Eq. (3.31) reduces to the correlation integral. Equation (3.31) also provides a means of producing the Fourier Transform of the function $f_1(t)$, by taking $f_2(t)$ equal to a constant and sweeping $\Delta\omega_a$.

Table 3.1 on the next page indicates the application capabilities of the optical system of Fig. 3.1. In the table, a δ-function optical input T(z) refers to a narrow window function; a δ-function voltage input refers to a short rectangular pulse.

3.2 Convolver and Related Devices

3.2.1 Introduction

In its simplest form, a communication system is characterized by a transmitter end where information is encoded and imposed upon some carrier, a transmission medium, and a receiver end where the information is abstracted from the received signal. A major consideration in all real communication systems is the signal to noise ratio at the output of the receiver. From a practical point of view, signal/noise considerations determine the number of repeaters required along the transmission path, and thus have a direct bearing on the cost of the system.

It is well known[75] that the signal to noise ratio with respect to power at the output of a receiver is given by

TABLE 3.1

Optical Processor Functions

Function	Time-Limited Voltage Inputs $f_1(t)$	$f_2(t)$	Space-Limited Optical Input $T(z)$	Output Voltage Signal	Comment
Modulation (Power)	$f_1(t)$	0	$\delta(z_o)$	$\left\|f_1(t - \frac{z_o}{v_a})\right\|^2$	Detect time-averaged intensity. Time-delay controlled by position of optical window.
Image Scanning (Intensity)	$\delta(t)$	0	$T(z)$	$\|T(v_a t)\|^2$	Detect time averaged intensity.
Convolution	$f_1(t)$	$f_2(t)$	1	$\int f_1(\tau)\, f_2(2t - \tau)\, d\tau$	Detect component at $2\,\omega_a$.
Modulation (Voltage)	$f_1(t)$	$\delta(t)$	1	$f_1\,(2t - \frac{d}{2\,v_a})$	
Image Scanning (Amplitude)	$\delta(t)$	1	$T(z)$	$T(v_a t)$	
Ambiguity Function Generation*	$f_1(t)$	$f_2(t)$	1	$\int f_1(\tau) f_2(\tau - 2t) e^{j\Delta\omega_a \tau}\, d\tau$	Input signals shifted in frequency by ω_a. Detect component at $2(\omega_a - \Delta\omega_a)$. Input signals must exhibit time-symmetry.
Fourier Transformation*	$f_1(t)$	1	1	$\int f_1(\tau) e^{j\Delta\omega_a \tau}\, d\tau$	Input signals shifted in frequency by ω_a. Detect component at $2(\omega_a - \Delta\omega_a)$.

*Sweeping of the frequency $\Delta\omega_a$ is required to implement function.

$$\frac{S}{N} = \frac{1/4\ \pi^2 \left| \int_{-\infty}^{\infty} S(\omega)\ H(\omega)\ e^{j\ t}\ d\omega \right|^2}{N_o/2\pi \int_{-\infty}^{\infty} |H(\omega)|^2\ d\omega} \tag{3.32}$$

where ω represents angular frequency, t is time, $S(\omega)$ is the frequency spectrum of the received signal, $H(\omega)$ is the transfer function of the receiver which is assumed linear and time invariant, and N_o is the noise spectrum power density, which for simplicity has been assumed flat. For a given signal, this ratio can be maximized by taking the receiver frequency characteristic to be of the form

$$H(\omega) = \alpha S^*(\omega)\ e^{-j\omega\tau} \tag{3.33}$$

where $S^*(\omega)$ is the complex conjugate of the signal spectrum, and α and τ are arbitrary real constants. This approach to matched filtering has of course, found widespread use in electrical and optical processing. The output of such a matched receiver to a signal of frequency spectrum $S(\omega)$ is given by

$$V_o = 1/2\pi \int_{-\infty}^{\infty} S(\omega)\ S^*(\omega)\ e^{-j\omega t}\ d\omega \tag{3.34}$$

where for simplicity, we have taken, $\alpha = 1$, $\tau = 0$. It is easily shown that this output can be equivalently written as an autocorrelation function of the signal s(t) itself, where

$$s(t) = 1/2\pi \int_{-\infty}^{\infty} S(\omega)\ e^{j\omega t}\ d\omega \tag{3.35}$$

$$S(\omega) = \int_{-\infty}^{\infty} s(t)\, e^{-j\omega t}\, dt \tag{3.36}$$

That is

$$V_o = \int_{-\infty}^{\infty} s(t')\, s(t' - t)\, dt \tag{3.37}$$

For the receiver output in a real communication system, $s(t')$ in Eq. (3.37) would be replaced by $s(t') + n(t')$, where $n(t')$ represents the noise. It is apparent from Eqs. (3.34) and (3.37) that best reception requires that either the receiver be matched in its frequency response to the incoming signal, or that the receiver be capable of signal correlation. The former method requires that the receiver have a different frequency response for each signal anticipated; the latter method requires a means for real-time correlation. These mathematically equivalent methods have very different realizations. The experimental demonstration of real-time correlation via the surface acousto-optic interaction is presented in Section 3.2.2.

If $s(t)$ represents a transmitted radar signal, then the matched filter output of the receiver for the return signal reflected from a moving target is given by

$$V_o = \int_{-\infty}^{\infty} s(t')\, s(t' - t)\, e^{j\Delta\omega t'}\, dt \quad . \tag{3.38}$$

In Eq. (3.38), which represents the ambiguity function of $s(t)$, the time delay t is related to the target's range, and the doppler shift $\Delta\omega$ is related to the time rate of change of the range.

The use of waveforms which can be processed at the receiver to enhance their detectability is of particular importance in modern communications. Each data element in such a system is generally encoded into a symbol from an a priori established alphabet. It is usual that the transmitted waveforms are of more complex form than the baseband data, but correlation can be performed at the receiver to increase detection probability since each symbol is one of a set of predetermined waveforms. The increased detectability is achieved at the expense of increased bandwidth requirements.

One code which has found widespread use, especially in multiple-access time slot systems, is the Barker code. This code is especially attractive since the autocorrelation of an N-bit Barker code has a correlation peak which is N times the magnitude of the side lobes. Barker sequences $\{q\}$, defined through the relation

$$\sum_{i=0}^{N-k-1} q_i \, q_{i+k} = \begin{cases} 0, & N-k \text{ even with } k \neq 0 \\ \pm 1, & N-k \text{ odd} \end{cases}, \tag{3.39}$$

have been found empirically for N = 2, 3, 4, 5, 7, 11, 13. The individual elements may take on values +1 or -1. For N > 13, no Barker codes exist. It is to be mentioned that other important codes do exist and have been of use. Of special interest are the pseudo-random noise code and linear fm chirp.

3.2.2 Experiment

The basic optical processor is shown schematically in Fig. 3.3. Light from a 3 mW HeNe laser is brought to a line focus by lenses L_1 to L_4, producing a $\sim$ 15 μm wide line in the surface of the $LiNbO_3$ delay line. Lens L_5 recollimates the light and L_6 produces the Fraunhofer diffraction pattern of the light amplitude distribution in its focal plane. Amplitude modulated signals are applied to inputs 1 and 2, and the final optical signal is detected by a photodiode positioned in the focal plane of L_6 where it collects the light of a single diffracted order.

The output of the photodiode, after electronic processing, is displayed on an oscilloscope. A typical processing scheme is shown in Fig. 3.4. Heterodyning of the photodiode signal and subsequent filtering with a tuned amplifier isolates the voltage component at the desired frequency.

Y-cut Z-propagating $LiNbO_3$ was employed for the acoustical delay line with the interdigital transducers matched to 50 Ω at the center frequency. Experiments were performed at several frequencies, results being given for 45 MHz. The 45 MHz delay line had a bandwidth of 9 MHz and an insertion loss of approximately 6 db per transducer. The 2 cm separation of the transducers corresponded to a total delay of 5.8 μsec. The transducer apertures were 2 mm wide. Diffraction was in the Raman-Nath regime. Convolution was obtained in zero, first, second, third, and fourth diffraction orders.

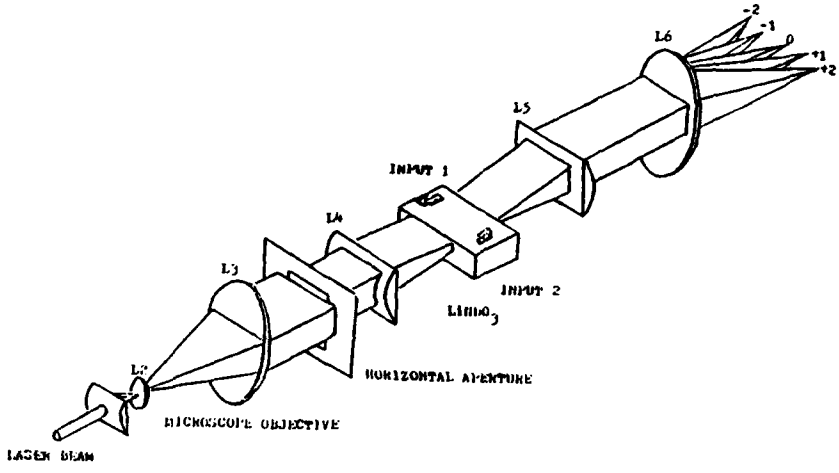

Fig. 3.3 Optical Processor for Real-Time Convolution

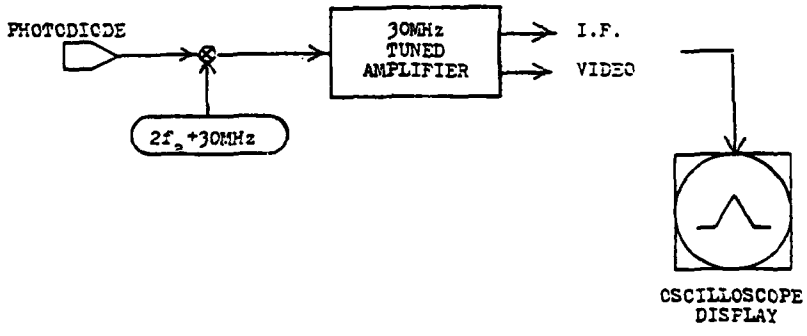

Fig. 3.4 Electronic Processing for Convolution. Electronic heterodyning isolates the component of the photodiode signal at twice ths acoustic frequency.

Figure 3.5 indicates results of the different methods of obtaining the output of the optical convolver. There is a choice as to which diffracted order in which to position the photodiode, as well as a choice of how to process the signal from the photodiode. The input square pulses of 500 mW power and 2 μsec duration which were applied to both transducers are shown in trace 3.5(a). In 3.5(b), on the same time scale, is the total intensity detected in the zero order, displayed on a high frequency oscilloscope after amplification. The signal is composed of a dc component and also high frequency components containing the desired autoconvolution. The component at $2\omega_a$ is obtained by heterodyning and filtering and is displayed in 3.5(c), which is the I.F. signal of the tuned amplifier. Figure 3.5(d) shows the tuned amplifier video output, which is the desired envelope of the autoconvolution signal at $2\omega_a$ in the first order.

It should be noted in these pictures that following the detected signal in time is a smaller signal which is unwanted. This signal is due to the reflection of the acoustic wave upon encountering the interdigital transducer at the opposite end of the delay line. A method was developed which completely eliminated this reflection problem.

In this method the surface acoustic waves do not superimpose, but run parallel to each other by offsetting one transducer slightly from the other as shown in Fig. 3.6. For bulk waves this configuration has been treated theoretically[76] as well as experimentally.[77]

AD-A082 752 RENSSELAER POLYTECHNIC INST TROY NY DEPT OF ELECTRIC--ETC F/G 17/1
ACOUSTO-OPTIC INTERACTION IN SURFACE ACOUSTIC WAVES AND ITS APP--ETC(U)
DEC 77 D SCHUMER, P DAS N00014-75-C-0772
UNCLASSIFIED MA-ONR-30 NL

2 of 2
AD A082752

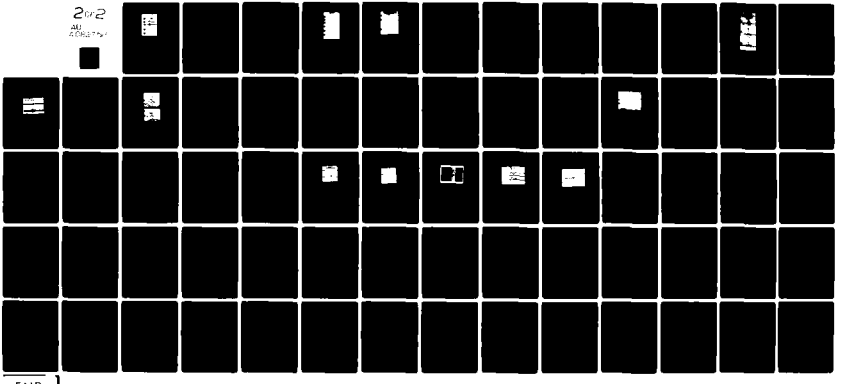

END
DATE FILMED
5-80
DTIC

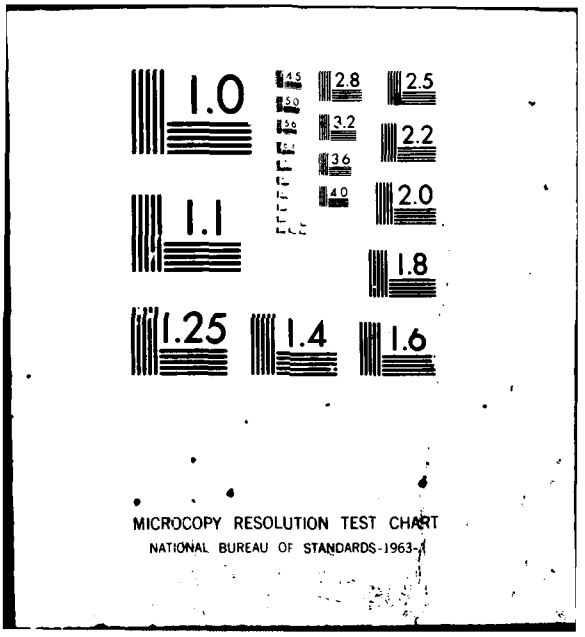
1.0
1.1
1.25
1.4
1.6
1.8
2.0
2.2
2.5
2.8
3.2
3.6
4.0
4.5
5.0
5.6
MICROCOPY RESOLUTION TEST CHART
NATIONAL BUREAU OF STANDARDS-1963-A

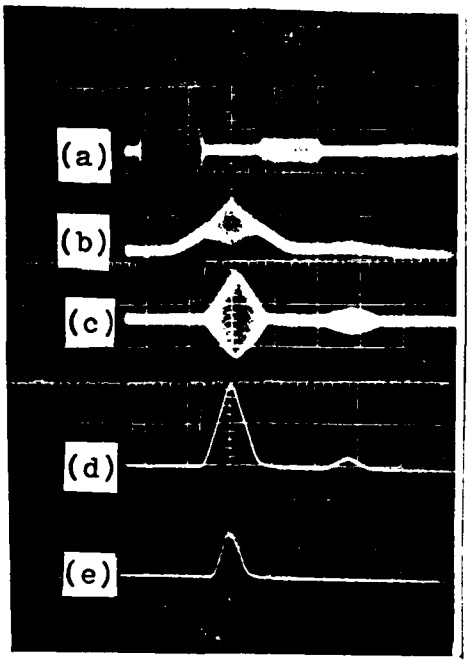

Fig. 3.5 Experimental Results of Real-Time Convolution (a) Rectangular pulse which is applied to both inputs (15Vp-p), (b) Total intensity detected in the zero order, (c) Autoconvolution signal at twice the acoustic frequency detected in zero order, (d) Envelope of autoconvolution at twice the acoustic frequency in the first order, and (e) Envelope of auto convolution at four times the acoustic frequency in the first order. Horizontal scale= 2μ sec/div.

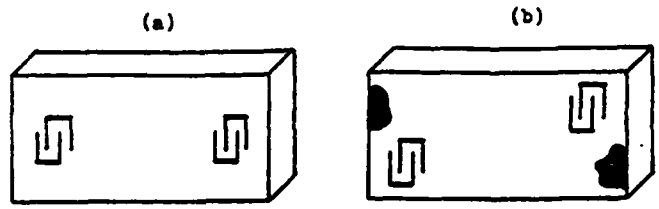

Fig. 3.6 Overlapping and Parallel Acoustic Tracks
(a) In usual acoustic delayline configuration acoustic tracks overlap. Reflections occur at opposite transducer.
(b) In parallel acoustic track configuration both tracks can be terminated with black wax to eliminate reflections.

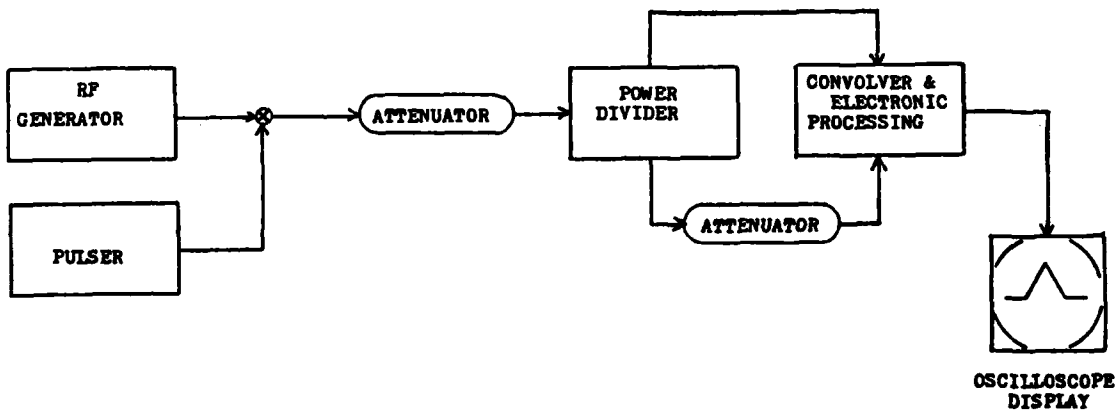

Fig. 3.9 Experimental Arrangement for Convolver Data

Figure 3.7 shows results using the parallel track configuration. For this $LiNbO_3$ sample the delay line length was less than the previous 2 cm, being now 1.5 cm. The absence of the autoconvolution of the reflected wave is readily apparent. Trace 3.7(a) is the rectangular input pulse, 3.7(b) the total intensity in the zero order, 3.7(c) and (d) the autoconvolution and envelope at $2\omega_a$ in the zero order, 3.7(e) and (f) the autoconvolution at $2\omega_a$ in the first order, and the envelope of the autoconvolution at $2\omega_a$ in the first order, respectively.

Figure 3.8 shows results for the autoconvolution of a signal composed of two rectangular pulses. Shown in the figure are (a) the input signal, (b) the autoconvolution detected at $2\omega_a$ in the zero order, and (c) the autoconvolution envelope.

For a rectangular acoustic pulse of fixed length, it is expected that the peak height of the triangular autoconvolution depends on the magnitude of the acoustic signal. For an ideal convolver, the peak height would be proportional to the input signal voltage. However, as was shown in Section 3.1, this situation only pertains in the small signal limit for the acousto-optic convolver. For larger input signals the convolution height follows the curve of Fig. 3.2. From Eq. (3.18) it is also apparent that the convolution height is sensitive to polarization.

The experimental arrangement of Fig. 3.9 was used to measure the peak convolution as a function of the signal power

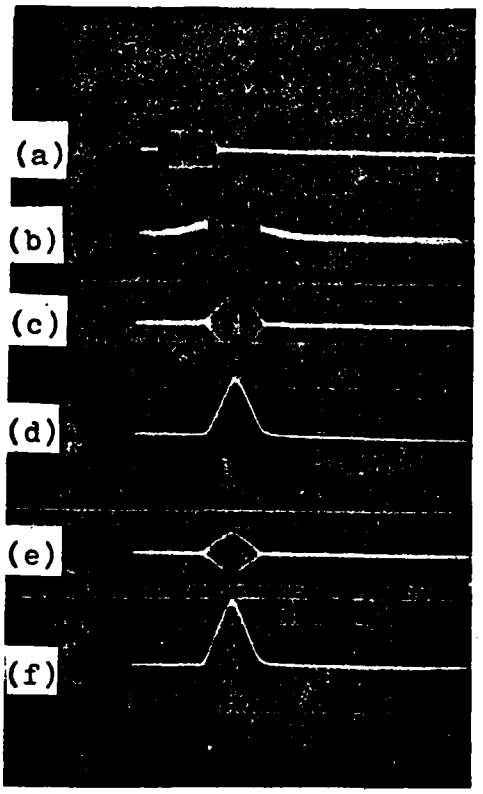

Fig. 3.7 Experimental Results of Real-Time Convolution Using Parallel Tracks.
(a) Rectangular pulse which is applied to both inputs (15Vp-p)(b) Total intensity in the zero order, (c) Auto-convolution and (d) Envelope in the zero order detected at twice the acoustic frequency (e)Autoconvolution and (f) Envelope at twice the acoustic frequency in the first order. Horizontal Scale= 2μ sec/div.

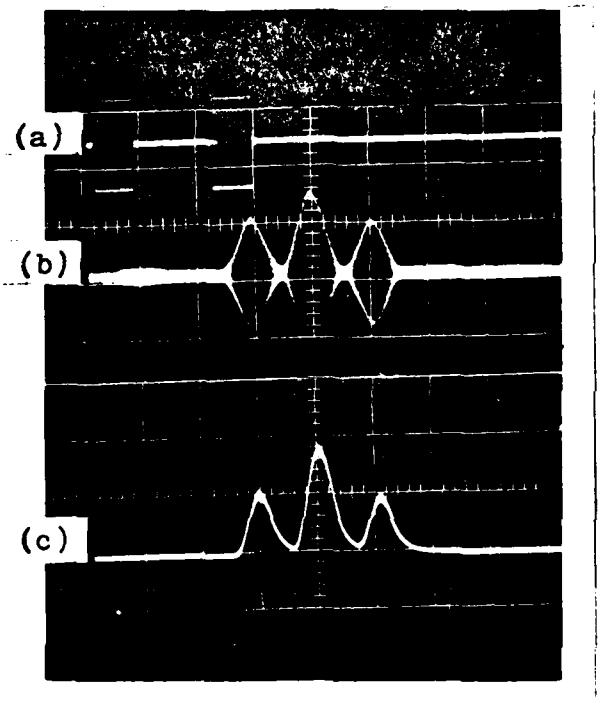

Fig. 3.8 Experimental Results of Real-Time Convolution Using Parallel Tracks.
(a) Input signal, (b) Autoconvolution detected at twice the acoustic frequency in the zero order, (c) Autoconvolution envelope.

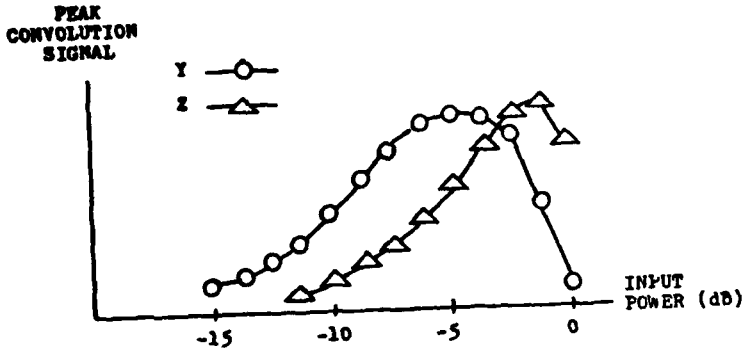

Fig. 3.10 Peak Convolution Signal vs. Input Power: First Order, $2\omega_a$. 0dB= .5W peak power into both inputs.

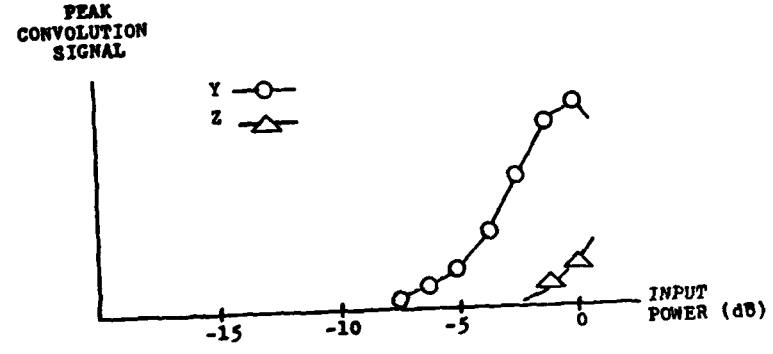

Fig.3.11 Peak Convolution Signal vs. Input Power: First Order, $4\omega_a$. 0dB= .5Wpeak power into both inputs.

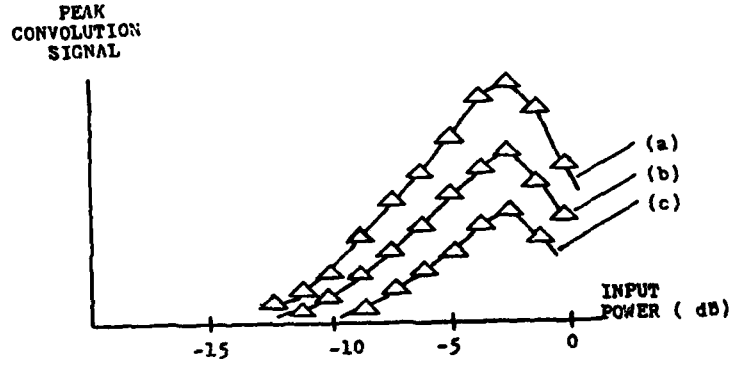

Fig. 3.12 Peak Convolution Signal vs. Input Power for Various Standing Wave Ratios: Z-Polarization. Data is for first order at $2\omega_a$. Horizontal scale: 0db= .5W peak power to input #1. Input #2 is down by (a) 3dB, (b) 6dB, and (c) 9 dB.

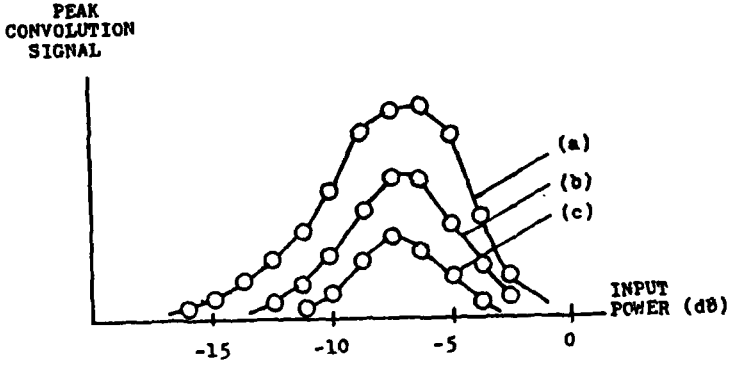

Fig. 3.13 Peak Convolution Signal vs. Input Power for Various Standing Wave Ratios: Y-Polarization. Data is for first order at $2\omega_a$. Horizontal scale: 0db=.5W peak power to input #1. Input #2 is down by (a) 3dB,(b) 6dB, and (c) 9 dB.

of the inputs. The acousto-optical convolver was exactly as that shown in Fig. 3.3, except that a polarizer was placed before the $LiNbO_3$ crystal and an analyzer after. This was necessary in order to take separate measurements for y- and z-polarization since the HeNe laser which was used provided randomly polarized light. To increase the light throughput, the analyzer was removed after verifying that polarization rotation did not occur. The acoustic input signals were single rectangular pulses in which the pulse length was not varied. Data was taken in different diffraction orders, as well as for different frequency components of the photodiode voltage. All data shown has been compensated for the slight nonlinearity of the detection system, including photodiode, mixer, and tuned amplifier.

Figure 3.10 shows peak convolution voltage as a function of input power for identical rectangular inputs. The graph is of the first order diffracted light for the convolution signal being detected at twice the acoustic frequency. The vertical scale of this graph, as with the following graphs, has been normalized to the maximum signal; it is the shape of the curve that is of interest. The horizontal scale is of input power on a decibel scale in which 0 db corresponds to a 1w p-p input divided equally between the two 50 Ω-matched interdigital transducers.

For both z-polarized and y-polarized light the convolution signal increases with input power, attains a maximum, and then decreases with increasing acoustic power, although the maxima

occur at different acoustic powers for the two polarizations. Because one would want to operate the device on a monotonically increasing portion of the curve, the location of the maximum is important.

Figure 3.11 is again for the first order diffracted light, in which the convolution signal appearing in the photodiode voltage at four times the input acoustic frequency is now detected. As in the previous case the y-polarized convolution signal attains its maximum at a lower power level than the z-polarized one, all other factors being equal. The families of curves shown in Figs. 3.12 and 3.13 were generated by taking the inputs to be of unequal magnitude. The peak convolution signal is plotted as a function of the magnitude of the larger input. The top curve in each graph is for the case in which one input is 3 db down from the other input. The second curve is for 6 db down, and the bottom curve for 9 db down. Both Figs. 3.12 and 3.13 are for the first order diffracted light and for the convolution detected at twice the acoustic frequency. In both graphs the maxima for the three cases occur at the same point, although this point depends on polarization.

Figure 3.14 is for the convolution detected at twice the acoustic frequency in the zero order light. The inputs were equal amplitude rectangular pulses. Again the y-polarized signal attains its maximum before the z-polarized.

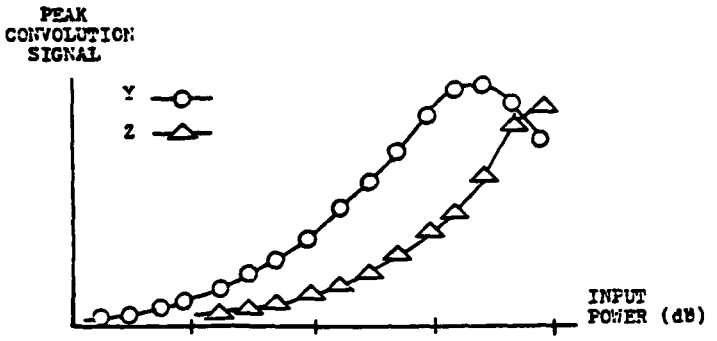

Fig. 3.14. Peak Convolution Signal vs. Input Power: 0 Order, $2\omega_a$. 0db=.5% peak power into both inputs.

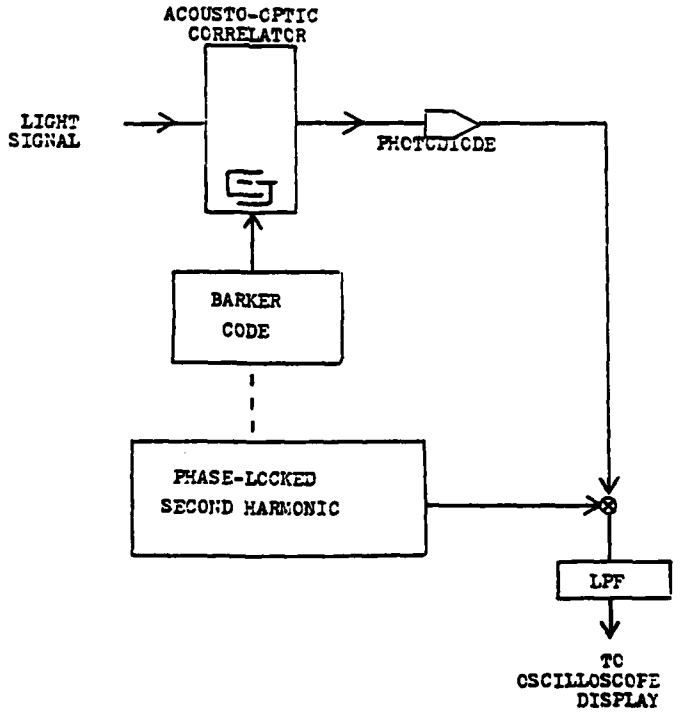

Fig.3.16 Electronic Arrangement for Barker Code Detection

Figure 3.15 shows the input signal and detected autocorrelation for a single rf pulse, a 3 bit Barker code, 7 bit Barker code, and 13 bit Barker code. The disproportionate sidelobe level in the last case was due to an electronic difficulty in the generation of the code. In obtaining these results a 100 MHz acousto-optic convolver was employed, using the side-entry interaction configuration. The light source was an argon laser operating at 5145 $\mathring{A}$. The Barker code was impressed upon the rf carrier by introducing a phase shift of π in the electrical cw signal used to launch the acoustic wave. In this way +1 was distinguished from -1. In detecting the autocorrelation of the Barker code, the electronic arrangement of Fig. 3.16 was employed, in which the second harmonic reference signal used in heterodyning was phase locked to the carrier of the reference code. Because the Barker code is not symmetric with respect to reversing the order of the bits, it was necessary to send the time-inverted signal from the correlating end in order to perform the correlating function with the convolver.

The autocorrelation of a linearly fm chirped signal is shown in Fig. 3.17. The 2 μsec pulse swept at a rate of 5 MHz sec^{-1} provided the time compression factor of 20 evidenced in that figure.

As was pointed out, under certain conditions the analog convolver can be used to generate the ambiguity function of time limited signals. Figure 3.18 shows the electronic arrangement for

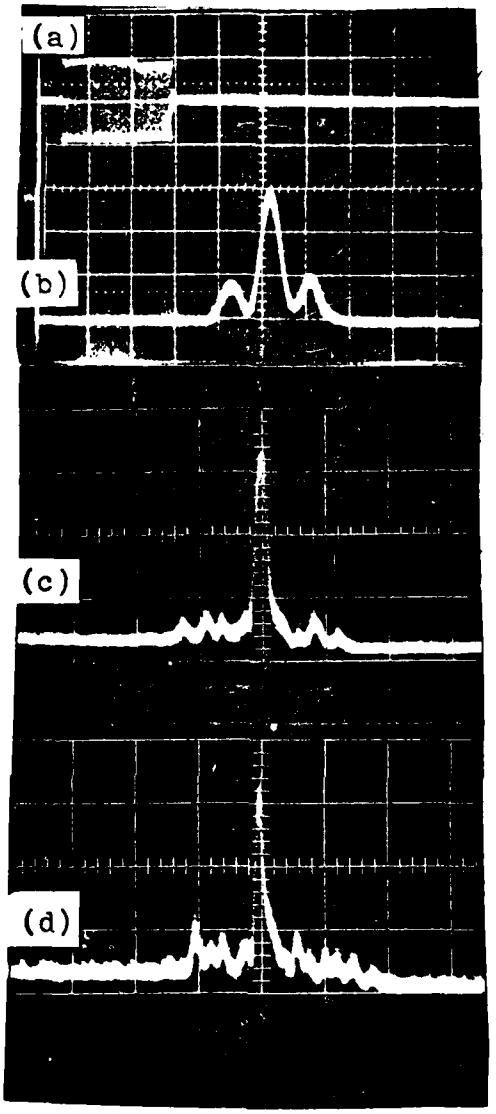

Fig 3.15 Autocorrelation of 100MHz Signals. Result for Barker encoded data.
(a) Input rf signal and (b) Autocorrelation of 3 bit . Barker code (1μ sec/div.) (c) Autocorrelation of 7 bit Barker code. (2μ sec/div.) (d) Autocorrelation of 13 bit Barker code (2μ sec/div.)

the ambiguity function generation. Figure 3.19 shows results for (a) a rectangular pulse and (b) a signal consisting of two rectangular pulses. The multi-exposure photographs provide a three-dimensional plot of the ambiguity function as a function of t and $\Delta\omega$.

3.2.3 Discussion

The theoretical treatment of the acousto-optic interaction of the previous chapter is related to the device description employed in this chapter through Eq. (3.18). It is of interest to relate these two descriptions of the interaction to the experimental results of the preceding section.

A comparison of Figs. 3.2 and 3.14 provides an experimental determination of the proportionality constant b appearing in Eqs. (3.2) and (3.3). From Fig. 3.2, for the case in which $V_1 = V_2$, the maximum convolution signal occurs for $V_1 = 1.1$. In the experimental result, Fig. 3.14, the maximum for y-polarization corresponds to -4 db from the 7.1 V point. This corresponds to a voltage signal of 5.8 V. Equation (3.2), with $\lambda_{o_f} = 6328$ Å and L = 2 mm, provides the result $b = 9.6 \times 10^{-6}\ V^{-1}$. Similarly, for z-polarization, $b = 7.8 \times 10^{-6}\ V^{-1}$.

An experimental determination can also be made for the effective phase grating $R_{ii}(\alpha)$ at this acoustic power level. With $V_1 = 1.1$, Eq. (3.18) provides $R_{22}(\alpha) = 2.5 \times 10^{-4}$, for example. These numerical values should only be

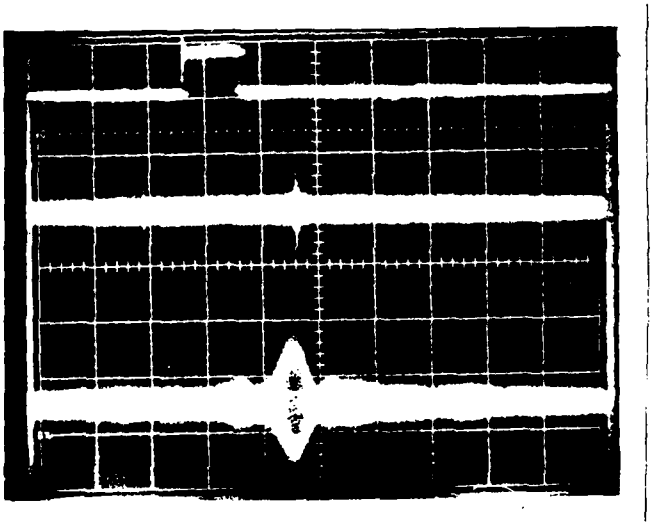

Fig. 3.17 Autocorrelation of Linear FM Chirp.
(a) Frequency swept input pulse (2μ sec/div.) (b) Autocorrelation (2μ sec/div.) (c) Autocorrelation on expanded scale (.1μ sec/div.)

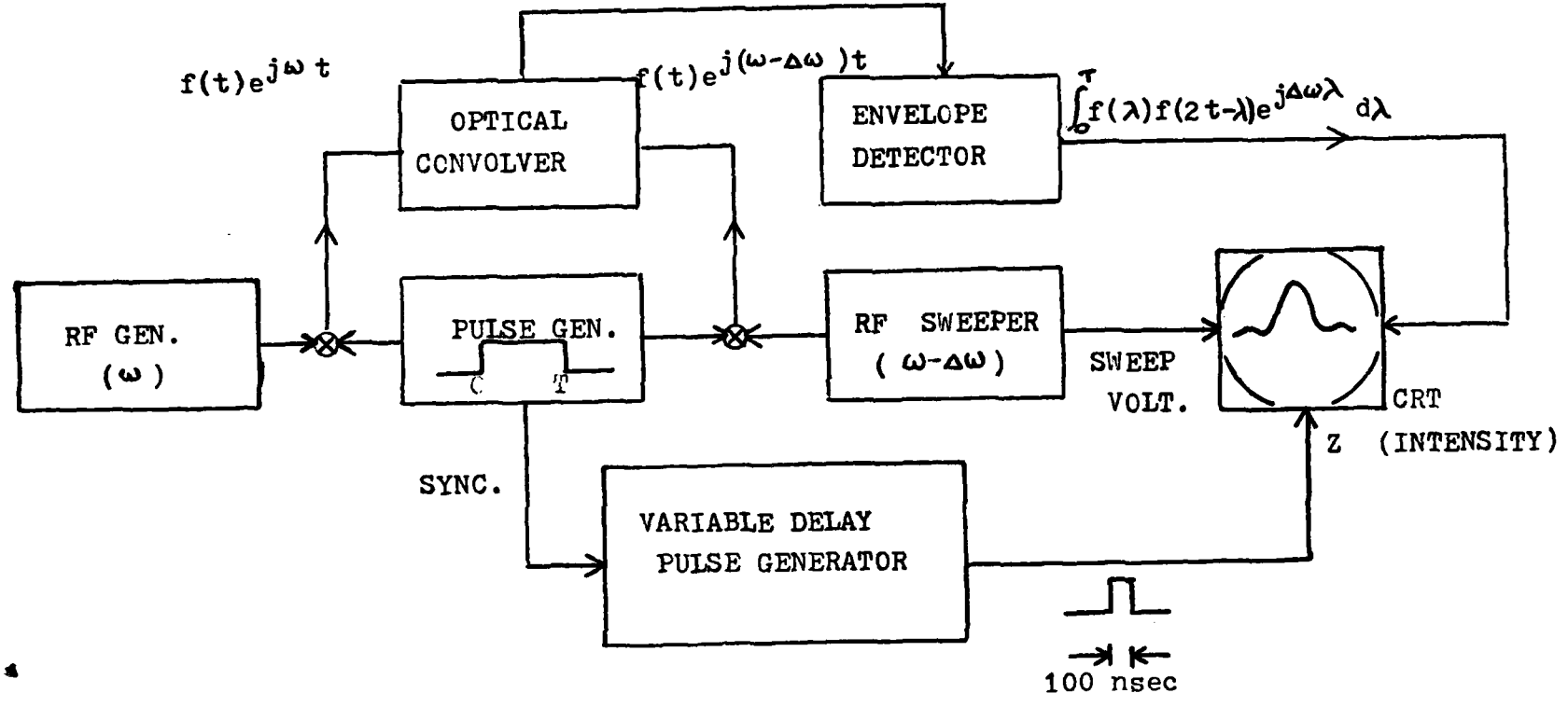

Fig. 3.18 Electronic Arrangement for Ambiguity Function Generation

(a)

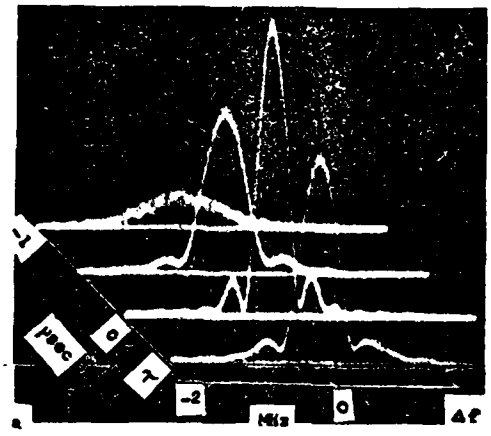

(b)

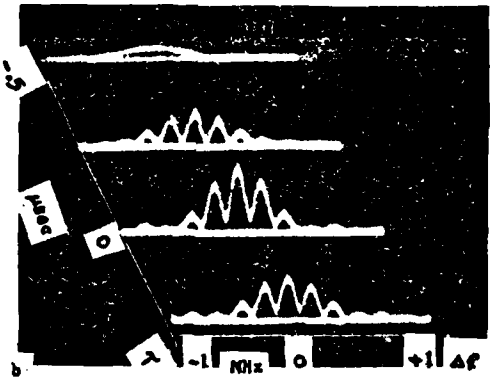

Fig. 3.19 Experimental Results for Ambiguity Function. (a) Multiexposure photograph showing slices of the ambiguity function surface of a 3μ sec pulse. (b) Ambiguity function for a signal comprised of two rectangular pulses each 0.8μ sec and separated by approximately 1.5μ sec.

considered estimates, since the Bessel function expansion Eq. (3.11) was truncated in obtaining Fig. 3.2.

In Figs. 3.10 - 3.14 the signal associated with the y-polarized light obtained its maximum value at a lower acoustic power level than that associated with the z-polarized light. With reference to Fig. 2.6 we can infer that the optical beam was focused one third of an acoustic wavelength or deeper beneath the crystal surface, since the interaction is stronger there for y-polarized light than for z-polarized.

From an operational point of view, several comments are in order regarding the use of the devices demonstrated for actual signal processing. Two important measures are time-bandwidth product and dynamic range.

The time-bandwidth product is given by the product of transducer bandwidth with acoustic delay line transit time. The former is proportional to transducer center frequency and inversely proportional to the number of transducer finger pairs. The 45 MHz device reported had a time bandwidth product of 52; the 100 MHz device had a time bandwidth product of 200.

For the processing of sophisticated signals comprised of lengthy algebraic codes, a large time-bandwidth produc' is required. The limitations imposed in achieving a large bandwidth product are primarily technological and not fundamental. High frequency transducers are required and long crystals of good quality. With presently available technology, time-bandwidth products of several thousand could be achieved.

The dynamic range of the acousto-optical convolver was limited in the experiment by the noise level of the I.F. amplifier and mixer combination employed. Any signal had to be above approximately 1 μV. The current from the photodiode is given by βH, where H is the light irradiance and β is the diode's response. For the HP 4203 photodiode used, β is 1.0 μA per mW/cm^2 of irradiance. Assuming a maximum irradiance of 1 W/cm^2 in any practical experiment, the resulting current through a 50 Ω load would result in a voltage of 50 mV. On this basis, the maximum obtainable dynamic range in any practical experiment would be 20 log (50,000) = 94 dB. The dynamic range evidenced in Figs. 3.10-3.14 is substantially less than this estimate due to the fact that in the experimental arrangement employed in obtaining this data, the irradiance never approached 1.0 μA per mW/cm^2.

While the detectability of a signal in noise is enhanced by using a matched filter receiver, it should be noted that any physical realization of a real-time correlator will have its own noise contributions. In the case of the acousto-optic convolver/correlator, the chief noise contributions are those associated with the light detection. An especially attractive feature of the acousto-optic signal processor presented is that it inherently employs optical heterodyning, which permits quantum limited detection,[14] thereby minimizing the processor noise contribution. The requirements placed on the photodetector are that it should have a linear response and that it must have good frequency

response. It must be capable of detecting signals of at least twice the acoustic frequency.

A particular feature of the technique used to generate the ambiguity function should be mentioned. A separate convolution operation must be performed for each discrete value of the delay-time parameter. Thus actual radar system implementation would require a signal repeater, which would sacrifice real-time capability, or an array of parallel processors.

Of practical importance applicable to the optical system alignment of all the devices discussed in this chapter is the fact that the photodetector need not be placed exactly at the diffraction plane, nor need it have a flat surface. It is spatially integrated intensity that is measured, and the total power of the light is the same whether measured in the diffraction plane or behind it, as long as the intensity pattern does not spread wider than the active area of the detector.

3.3 Optical Communication System

3.3.1 Introduction

To use the convolver/correlator described in the Section 3.2 in an optical communication system, it is necessary to receive the transmitted data at the receiver end, convert this to an electrical signal, use this signal as one input to the acousto-optic correlator, and supply the desired reference code to the other input.

Far more desireable would be to use the light directly as one of the correlator inputs. The possibility of such an arrangement is suggested by the parallel track configuration shown in Fig. 3.6, in which the acoustic tracks are nonoverlapping.

A natural extension of the parallel track configuration would be to separate the two tracks completely, using one for light modulation at the transmitter end of a communication system, and using the second acoustic track for correlation of the received light signal at the receiver end. It is a requirement of this particular scheme that the transmission medium preserve the phase front of the transmitted light. Such a system is applicable where the optical transmission line can be modeled as a series of lenses, as indicated in Fig. 3.20(a). Under this assumption, Fig. 3.20(b) depicts the communication system implementation.

3.3.2 Experiment

The arrangement shown in Fig. 3.21 was used to approximate an actual communication system. A uniform argon laser beam was brought to a line focus in the transmitter acousto-optic modulator. Lens L_1, placed intermediately between the two $LiNbO_3$ acousto-optic modulators and twice its focal length from both produced a real inverted image with unit magnification of the transmitter acousto-optic modulator in the plane of the receiver acousto-optic correlator. L_2 then provided the Fourier transformation of this spatial light distribution producing distinct spots in its

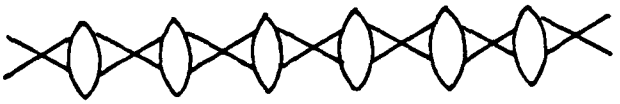

(a) Lens model of optical waveguide

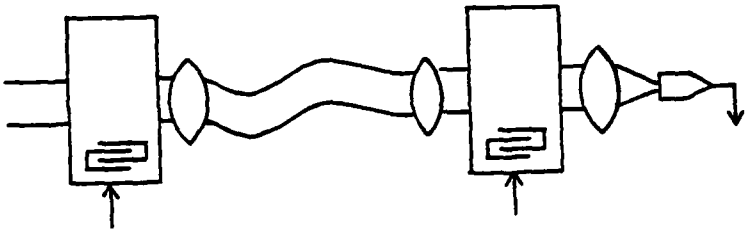

(b) System implementation

Fig. 3.20 Optical Communication System

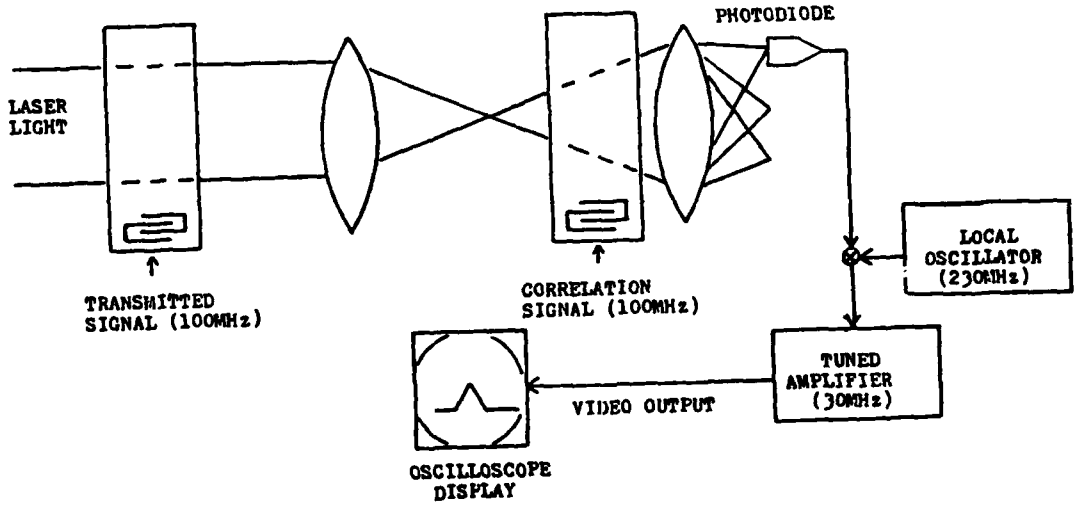

Fig. 3.21 Optical Communications Implementation 1

focal plane corresponding to the various diffraction orders. A photodiode collected light in the first order diffracted light, and electronic processing of the photodiode signal yielded the oscilloscope display of the desired convolution in the same manner as discussed previously.

An objection to this arrangement is that the optical transmission line must carry not only the modulated light containing the information but the unmodulated light as well. An alternative arrangement is shown in Fig. 3.22. In this configuration only the first order diffracted light from the first acousto-optic modulator is permitted to interact with the second acousto-optic modulator. The photodiode output in this case provides the desired convolution without further electronic processing. Shown in Fig. 3.23 are experimental results using the latter arrangement.

3.3.3 Discussion

The discussion of the real-time convolver is germane to the optical communication system presented, with two notable exceptions. First, the light is video detected in the system of Fig. 3.22. The consequences of this are less noise immunity than for heterodyne detection and the relaxing of the detector frequency response requirement. The reduced detector frequency requirements would enable the use of phototransistors rather than the faster photodiodes, with the obvious advantage of large signal gain.

Second, the system of Fig. 3.22 does not produce the convolution of the signals $f_1(t)$ and $f_2(t)$, but rather the square

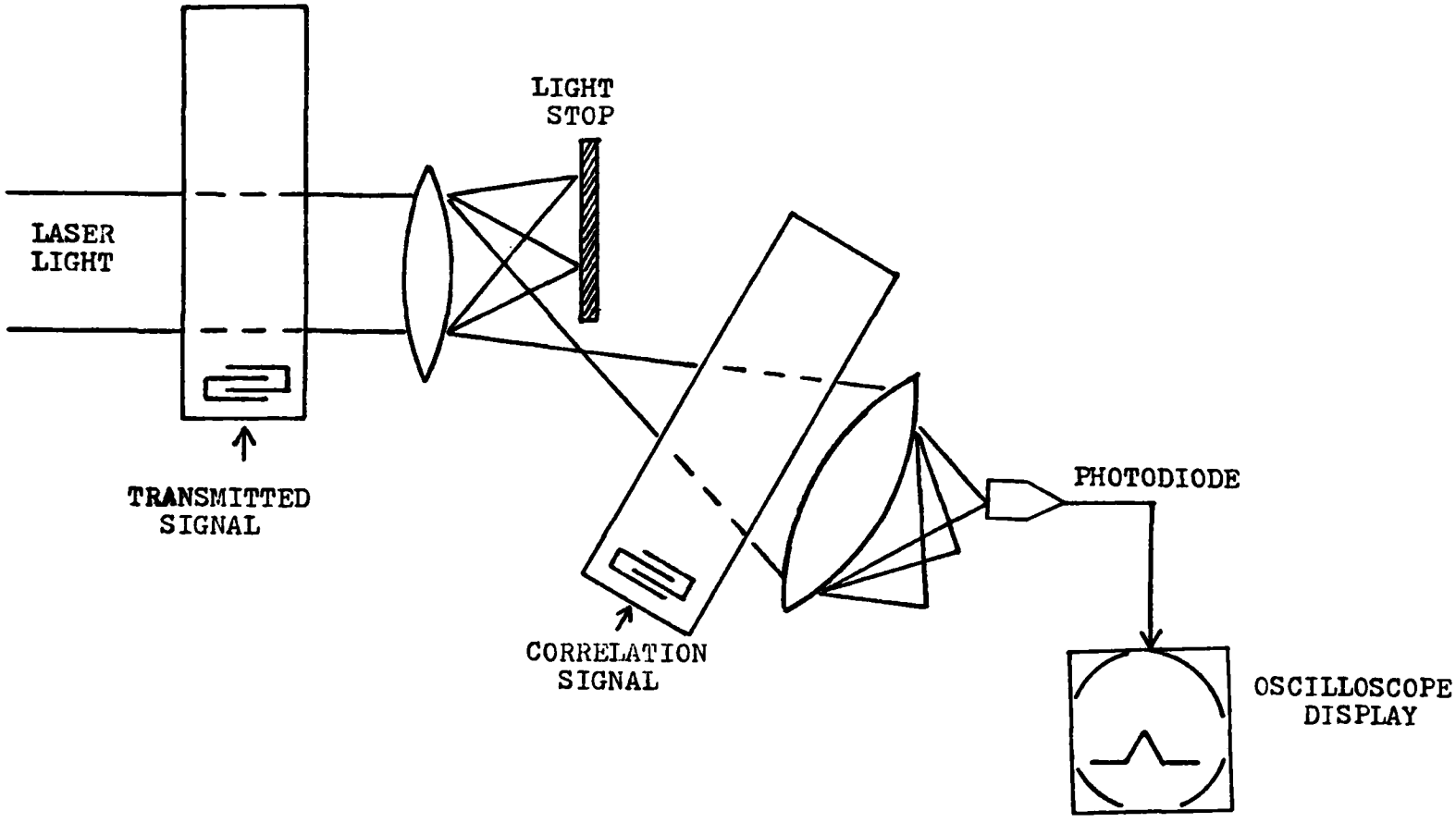

Fig. 3.22 Optical Communications: Implementation 2

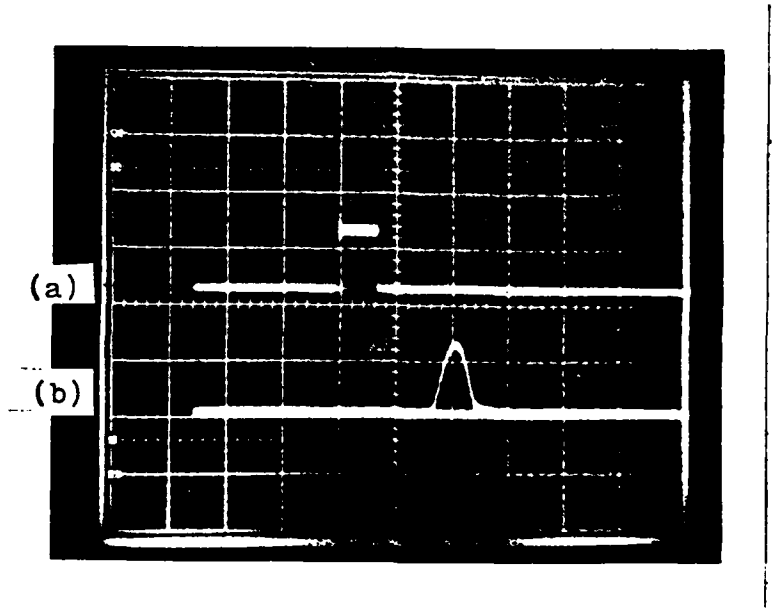

Fig. 3.23 Optical Communication System: Experimental Results (a) Rectangular pulse of 1.8 μ sec duration applied to transmitter and correlator (b) Photodiode output displayed directly on oscilloscope.

of the convolution. This is not readily apparent from the experimental result due to the fact that a low frequency oscilloscope was used to display the signal, resulting in rounding of the features. That it is the square of the convolution is easily seen by analyzing the system using the device model developed in Section 3.1.

As only the first order diffracted light is passed by the aperture stop, the light distribution incident on the acousto-optic correlator is $J_1[V_1(v_a t - z - d/2)]$, which is incident at the light frequency $(\omega + \omega_a)$. Thus the light amplitude diffracted by the correlator is given by

$$A(\theta) = e^{j(\omega + \omega_a)t} \int_{-\infty}^{\infty} J_1[V_1(v_a t - z - d/2)] e^{j V_2(v_a t + z + d/2)\sin(\omega_a t + k_a z)} dz. \tag{3.40}$$

Expanding the complex exponential in terms of Bessel functions, the first order diffracted light from the correlator is given by

$$A_1 = e^{j(\omega + \omega_a)t} \int_{-\infty}^{\infty} J_1[V_1(v_a t - z - d/2)]\, J_1[V_2(v_a t + z + d/2)]\, dz \tag{3.41}$$

which in the limit of small V_1 and V_2 is the convolution integral. What is detected by the photodetector is the intensity

$$I_1 = \left| \int_{-\infty}^{\infty} J_1[V_1(v_a t - z - d/2)]\, J_1[V_2(v_a t + z + d/2)]\, dz \right|^2 , \tag{3.42}$$

which is incident at the light frequency $(\omega + 2\omega_a)$.

The convolution of Eq. (3.41) could be abstracted by using optical heterodyning techniques, combining a coherent

reference with this light. If desired a logarithmic amplifier can be used to obtain the proper convolution from the detected light, Eq. (3.42). However, for purposes of signal identification, there is no signal-to-noise advantage in doing so.

It is of interest to compare the optical communication system employing an acousto-optic correlator at the receiver end with the simpler system in which uncoded serial data is transmitted and received by video detection. For simplicity we assume that both systems are characterized by stochastic noise associated with transmission through the channel, with average power P_c. In addition we assume that the photodetector and associated circuitry at the reception end of both systems can be characterized by a fixed noise power P_d, which in a crude approximation is taken to be independent of the incident light signal. This is reasonable if the maximum photodetector shot noise does not exceed the thermal noise of the load resistor.

Since the channel noise and detector noise are uncorrelated, the signal-to-noise ratio at the detector output for the system transmitting uncoded data, in terms of the average signal power P_s, is

$$(S/N)_{\text{uncoded}} = \frac{P_s}{P_c + P_d} \tag{3.43}$$

For the system employing coded data, designating by N_i the ideal process gain and by η the acousto-optic deflection factor of the correlator, defined as the ratio of useful deflected

light to incident light, the signal-to-noise ratio is

$$(S/N)_{coded} = \frac{\eta N_i P_s}{\eta P_c + P_d} \quad . \tag{3.44}$$

The deflection factor is always equal to or less than unity. In a Bragg deflector, η can be 1 under maximum deflection conditions, but for a Raman-Nath device in which light is detected in the first diffraction order, $.339 \leq \eta \leq 0$, since $(J_1)^2_{max} = .339$. Defining γ by $\gamma = P_c/P_d$, the ratio of the coded to the uncoded signal-to-noise ratio is given by

$$\frac{(S/N)_{coded}}{(S/N)_{uncoded}} = \frac{\eta N_i(\gamma + 1)}{\eta \gamma + 1} \tag{3.45}$$

For a noisy channel and fairly efficient acousto-optic deflector, $\gamma >> 1$ and $\eta \gamma >> 1$,

$$\frac{(S/N)_{coded}}{(S/N)_{uncoded}} = N_i \quad , \tag{3.46}$$

as expected. The process gain N_i for autocorrelation of an M-bit pseudo-random code is M, which can be made quite large being limited by the correlator time-bandwidth product.

In the event that the channel is noiseless, $\gamma = 0$,

$$\frac{(S/N)_{coded}}{(S/N)_{uncoded}} = \eta N_i \quad . \tag{3.47}$$

There is an advantage in using the acousto-optic correlator only if the code is sufficiently long to compensate for light lost as

a consequence of using the acousto-optic device. Moreover, if the received light signal is not buried in noise due to the channel, correlation techniques are not appropriate.

3.4 Image Scanner

3.4.1 Introduction

Surface acoustic waves provide a convenient means of scanning a light intensity distribution for the purpose of facsimile transmission. The first reported experiments employed the photoconductive effect along the surface of a semiconductor.[78] Allipi et al.[48] demonstrated acousto-optic image scanning with surface waves using the top reflection and back reflection configurations. We present here an image scanner for facsimile transmission of black and white transparencies employing the side entry technique, and extend the capability of that system to handling color transparencies.

The black and white image scanner is shown in Fig. 3.24. Incident laser light is spatially modulated by a one dimensional transparency which is imaged into the $LiNbO_3$ crystal. A short acoustic pulse scans this image and provides a light intensity in the first order diffracted light which replicates the intensity distribution as a function of time. Scanning of a two dimensional transparency is achieved by mechanical translation of the transparency in the horizontal direction after each vertical scan of the acoustic pulse.

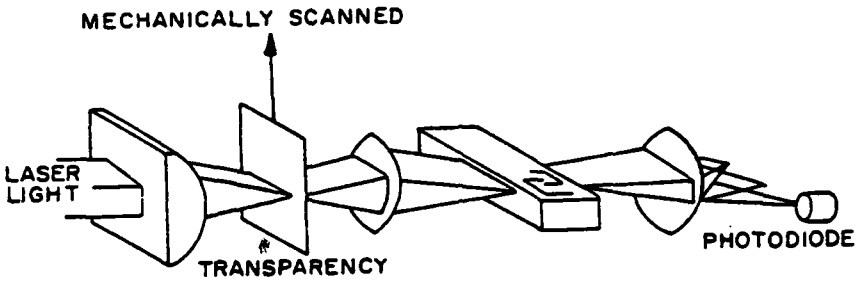

Fig. 3.24 Black and White Image Scanner

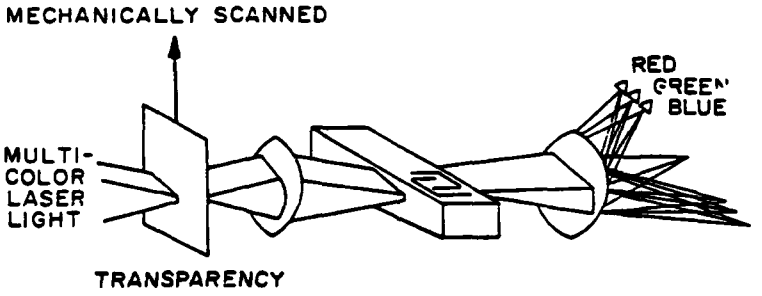

Fig. 3.25 Color Image Scanner

Recalling that in Raman-Nath diffraction the diffraction angle of the first order is proportional to the light wavelength, λ, it is a natural extension of this system to provide scanning of multicolor transparencies. The incident light is now composed of several colors, such as red, green, and blue laser light, and the intensity transmission function is a color transparency. The first order diffracted light exits at a different angle for each color, as shown in Fig. 3.25. Three photodiodes, one for each color, are then used to collect the light. The three photodiode signals, after amplification, can then be multiplexed for transmission. Because diffraction is used rather than color filters to separate color components, the system is capable of color separation with high spectral purity.

An important factor which characterizes any image scanner is resolution. For an acoustic pulse of time duration T_P, the spatial resolution obtained is given by

$$R = T_P v_a \quad , \tag{3.48}$$

where v_a is the acoustic velocity. The design of the transducer used to launch the surface acoustic wave provides a lower limit for the pulse duration T_P. For the interdigital transducers used, having 5 finger pairs, the transducer bandwidth is 20%. Thus, the minimum pulse duration $T_{P(min)}$ is given by

$$T_{P(min)} = 5/f_o \quad , \tag{3.49}$$

where f_o is the transducer center frequency.

The amount of light diffracted is proportional to the pulse length, T_p. Therefore, as resolution is improved, the signal is decreased, other factors being equal. For this reason, in a practical scheme one cannot simply improve resolution without bound by going to higher acoustic frequencies. Ultimately, signal-to-noise considerations will determine the optimal pulse width, and therefore, resolution. The signal-to-noise ratio at the photodetector output is improved by increasing the incident light intensity, but optical damage to the $LiNbO_3$ places a limit on useful intensity.

In addition to determining resolution, the distance $T_p v_a$ also determines the spot size of the diffracted orders, since this is the diffraction limiting aperture. If a lens of focal length F is used to form the Fraunhofer diffraction pattern of the diffracted light, the spot size, s, in each order will be on the order of

$$s = \frac{F \lambda}{T_p v_a} \quad . \tag{3.50}$$

It is quite possible that if T_p is small enough the spots corresponding to the first order diffraction for each color used may overlap. In this case, a dispersive element such as a prism can be used to enhance the spatial separation of the different color components.

3.4.2 Experiment

In the experiment, green (5145 Å) and blue (4880 Å) light from an argon ion laser was combined in a beam splitter with red

light (6328 Å) from a HeNe laser. The beam was horizontally expanded, then truncated and recollimated, so that the light incident on the color transparency was of uniform intensity in the one dimension of interest. The surface acoustic waves were launched on YZ $LiNbO_3$ by interdigital transducers matched to 50 Ω at center frequency. Several different $LiNbO_3$ samples were used, with center frequencies ranging from 50 to 100 MHz. We take f_o = 100 MHz for the following numerical example. From Eq. (3.49), $T_{p(min)}$ = 50 nsec. Using v_a = 3488 m/sec, Eq. (3.48) provides that this corresponds to a spatial resolution on the crystal of 0.17 mm. This provides a scan of 2 x 10^7 spots/sec. For a $LiNbO_3$ sample 5 cm long the number of resolvable spots per scan is 294. Electronic constraints, however, required the use of 200 nsec pulses. Therefore, the resolution obtained was 0.68 mm, corresponding to 73 resolvable spots and a scan rate of 5 x 10^6 sec^{-1}. For the red, green, and blue laser beams the respective diffraction angles for the first order diffracted light were 0.019, 0.015, and 0.014 radians for an acoustic frequency of 100 MHz. Using a 30 cm focal length lens to form the diffraction pattern of the diffracted light and an acoustic pulse of 200 nsec, the spot sizes of the focused diffracted light were 0.27 mm, 0.22 mm, and 0.21 mm for the red, green, and blue respectively. These spots were spatially separated.

Figures 3.26 - 3.31 show results obtained. Figure 3.26(a) is the trace of the signal obtained with no modulating transparency present, except for a window aperture. The response shown is

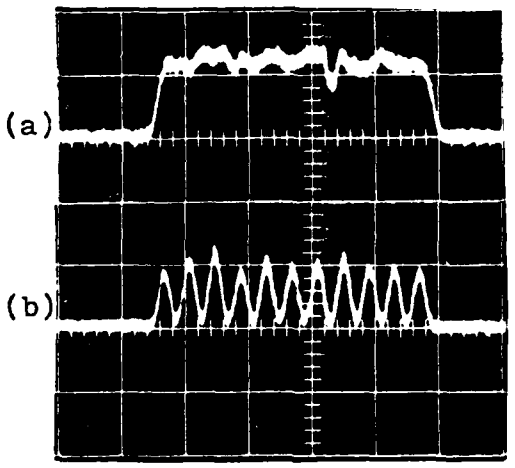

Fig. 3.26 Unprocessed Scanner Output
(a)Photodiode output with no input transparency (b) Photodiode output with input transparency composed of .8mm wide black lines evenly spaced (1μ sec/div.)

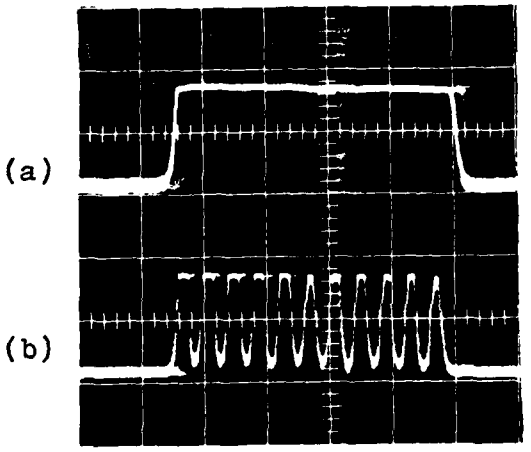

Fig. 3.27 Scanner Output With Electronic Processing
(a) Photodiode output with no input transparency after threshold detection and limiting. (b) Processed photodiode output for input transparency of .8mm wide lines (1μ sec/div.)

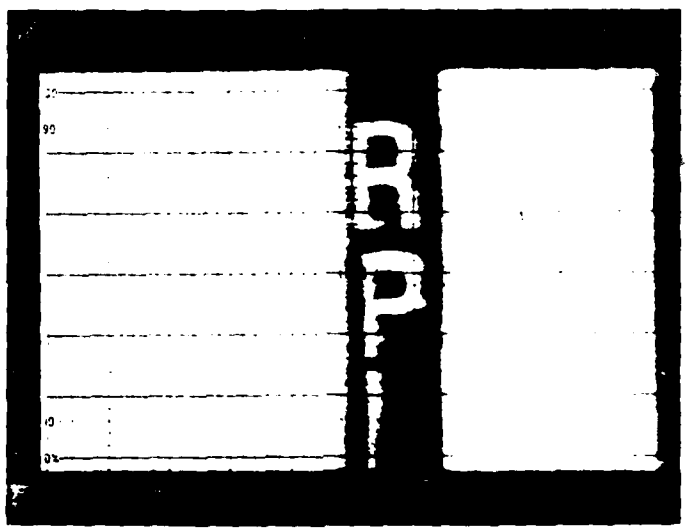

Fig. 3.28 Two Dimensional Image Scanning
Photodiode output modulates Z-axis of oscilloscope while transparency is scanned mechanically in the vertical direction. Letters are 4mm high. Acoustic frequency=100 MHz.

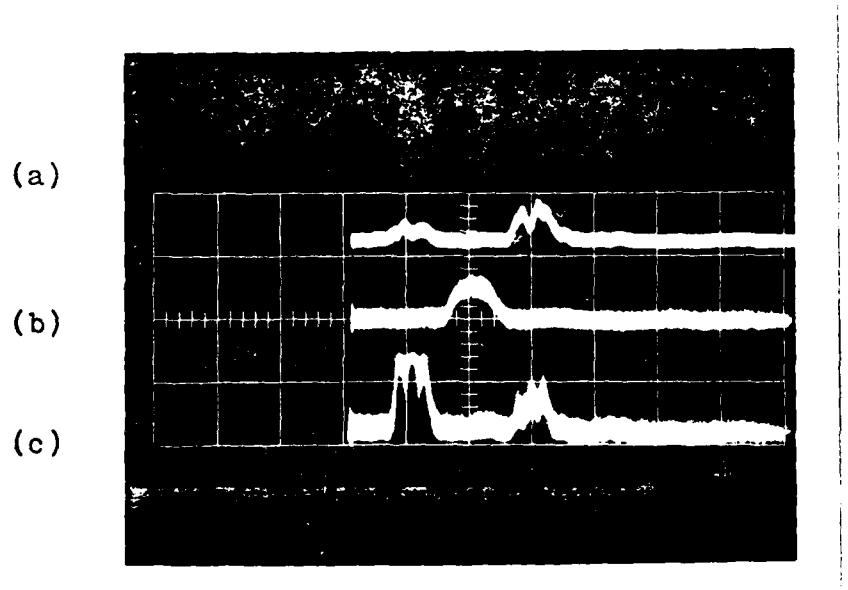

Fig. 3.29 Results of Color Image Scanning
Photodiode output for (a) Blue light (b) Red light (c) Green light. Optical input is a green-red-blue striped transparency. Time scale=1μ sec/div. Acoustic frequency =100 MHz.

(a)

(b)

(c)

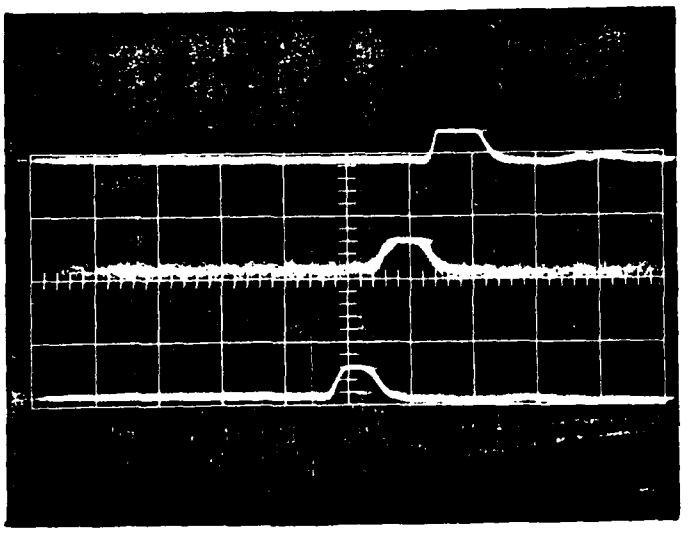

Fig. 3.30 Results for Color Image Scanning
Photodiode output for (a) Blue light (b) Red light (c) Green light. Optical input is a green-red-blue striped transparency in which only one section is illuminated at a time. Time scale= 1μ sec/div. Acoustic frequency = 100 MHz.

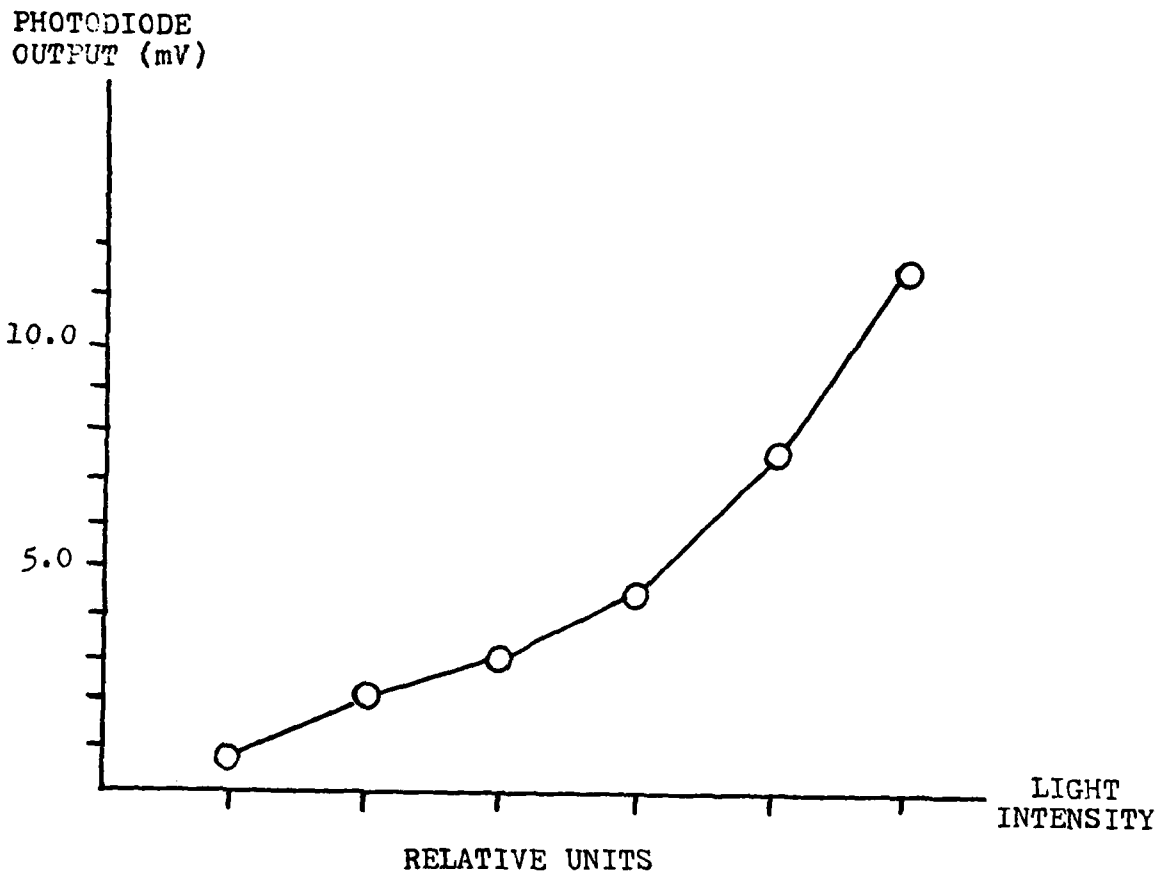

Fig. 3.31 Image Scanner Intensity Response (Photodide output across 50 ohm load)

4.5 μsec long which corresponds to 1.6 cm of interaction length. The acoustic pulse was 200 nsec long at a center frequency of 100 MHz. Figure 3.26(b) is the oscilloscope trace for a monochromatic object composed of .84 mm black and white stripes. The static variations, resulting from beam nonuniformities and crystal surface defects, were eliminated by imposing a threshold detector and limiter before display. Results are shown in Fig. 3.27. The cost of this modification is the digital nature of the output in which some information concerning gray tones is lost.

The two dimensional scanning capability is shown in Fig. 3.28, in which mechanical scanning of the black and white transparency was used for the vertical direction. The photodiode output was used to modulate the oscilloscope z-axis to obtain this picture. A voltage ramp synchronized with the vertical mechanical scan was applied to the y-axis, and sweep triggering was synchronized to the acoustic pulse.

Figure 3.29 demonstrates color scanning operation. The one dimensional object was composed of parallel colored stripes, green, red, and blue. The top trace is the detector output placed to collect the blue light, the middle trace is for the red light, and bottom trace is for the green light. Note that a blue component of light is in evidence in the light passed by the green stripe, and visa versa. Covering the blue stripe while detecting the green light, and separately covering

the green stripe while detecting the blue light, gave the corresponding output signals of Fig. 3.30.

Using neutral density transparencies the photodiode output of the image scanner was measured as a function of light intensity incident on the $LiNbO_3$ crystal. Results are shown in Fig. 7.

3.4.3 Discussion

The acousto-optic interaction provides a simple means of scanning monochromatic as well as color transparencies for the purpose of transforming the light intensity distribution into a voltage signal. In the system demonstrated, resolution was limited by the bandwidth of a preamplifier in the detection system, but normally resolution would be limited by transducer bandwidth. Although higher bandwidths can be achieved with bulk wave transducers, the higher acoustic velocity of bulk waves tends to degrade resolution. For this reason it is advantageous to use surface acoustic wave devices for image scanning.

The lens system used in imaging the transparency into the crystal can be used to provide magnification. Hence resolution is a measure of spatial separation achieveable in the plane of the crystal, not in the transparency plane. For this reason a better measure of system capability is the number of resolveable spots. The number of resolveable spots is proportional to the transducer bandwidth and acoustic propagation length, hence it is

directly proportional to the device time-bandwidth product. It is profitable to improve the time-bandwidth product by means of increasing transducer bandwidth, rather than going to longer crystals, because for two dimensional scanning the minimum time for each individual line scan is given by the transit time of the acoustic pulse to travel the sample length.

Because laser sources were used to illuminate the transparency, the color components detected are not directly compatible with commercial television standards. The HeNe red is only slightly deeper than that specified by the FCC. The blue and green argon lines, however, depart considerably from both the FCC values and the currently used television phosphors. The 5145 Å green should be closer to 5350 Å, and the 4880 Å blue should be 4700 Å. The use of the argon lines excludes discrimination of deep blues and purples. It is to be noted that the imaging system is completely compatible with the laser TV display system reported by Korpel et al.,[79] as they employ the same laser lines. No colorimetric distortion would be introduced in using the two complementary systems, but as pointed out deep blues and purples would be absent.

An especially attractive feature of the acousto-optic image scanner is that it is easily adapted to other functions such as electronic focusing of images and forming real-time Fourier transforms of images. These operations are achieved electronically without any alteration of the optical system. For example, to

obtain the Fourier transform of a transparency imaged into the $LiNbO_3$, two acoustic waves are launched from opposite ends of the crystal. One is the usual narrow scanning pulse which modulates its carrier which is at frequency ω_a, while the second is a continuous constant amplitude wave at the frequency $\omega_a + \Delta\omega_a$. The photodiode voltage, processed as for the ambiguity function, provides the signal $\tau(v_a t) \exp [\Delta\omega_a t]$. Integration of this signal in the time domain provides the desired Fourier transform as $\Delta\omega_a$ is swept in time.

CHAPTER 4

SUMMARY AND CONCLUSIONS

4.1 Summary

A classical description of the interaction of laser light with ultrasonic surface acoustic waves and an experimental demonstration of the application of the interaction to several new devices is presented. The analysis assumes linear constitutive relations, and it assumes the perturbation of the impermeability tensor elements is linearly related to the strain and electric field associated with the acoustic wave. The inclusion of a term proportional to the rotation tensor is readily incorporated into the analysis but is deleted in the numerical calculation due to the unavailability of published data for the appropriate coefficients. Good agreement with previously published experimental data is achieved but requires some modification of the reported photoelastic constants.

A scalar diffraction model of the acousto-optic interaction is discussed and is used in describing the operation of the modulator, image scanner, and convolver. The scalar diffraction model is related analytically to the theoretical treatment of the interaction in surface acoustic waves and numerically to experimental results for the convolver.

New experimental results are obtained and device applications demonstrated using the side-entry interaction configuration.

New experimental results for the real-time convolver employing optical heterodyning include autocorrelation of Barker codes, ambiguity function generation, and the measurement of diffraction characteristics for y- and z-polarized light.

Results are given for the correlation of a time varying light intensity distribution with an electrical signal, and the application to an optical communication system is discussed. A scheme involving an acousto-optic modulator at the transmission end and an acousto-optic correlator at the reception end is demonstrated. In this scheme only modulated light in the first diffraction order of the acousto-optic modulator is transmitted with the result that squared correlation is performed at the reception end, detected in real-time by video detection.

The scanning of one and two dimensional black and white transparencies is performed using the side-entry technique. Mechanical scanning is employed for the two dimensional scan, but could be replaced by faster light deflection methods. The system is extended to the scanning of color transparencies. High spectral purity is achieved, and no cross-talk due to overlapping diffraction orders is observed.

4.2 Conclusions

The side-entry technique provides a simple and efficient means of diffracting an unguided optical beam by means of the acousto-optic interaction using surface acoustic waves. The

technique provides a much longer interaction length than any of the other interaction configurations, comparable to bulk wave devices, while retaining the advantageous features of surface acoustic waves. These features include high power density for a given acoustic power, a lower acoustic group velocity, and use of planar fabrication techniques. In using Rayleigh waves, there is the additional significant advantage that the acoustic propagation is dispersionless. The potential of utilizing thin films is also available with surface wave devices which is not with bulk wave devices. The longer interaction length achieved with the side-entry technique which is not possible in the other interaction configurations provides a more efficient diffraction, in terms of electrical drive power, and puts the interaction in the Bragg regime at a lower frequency. At 45 MHz about 50% of the zero order light can be modulated with 300 mW of applied electrical power using the side-entry technique. Any of the other three configurations would provide only a few percent modulation. The side-entry configuration can provide Bragg scattering at frequencies below 150 MHz. The top transmission configuration remains in the Raman-Nath regime to frequencies above 1 GHz.

In terms of electrical drive power, the devices reported here employing the side-entry technique do not compare favorably with the best integrated optics acousto-optic modulators reported in recent literature. Nguyen[57] reports acousto-optic Bragg

deflection employing guided optical waves and surface acoustic waves in which 50% of the output zero order light is deflected with 68 mW of electric drive power. This result can probably only be achieved with integrated optics structures. The paper cited, however, does not list optical losses associated with coupling into the waveguide, so actual fractional deflection might be less than 50%.

All of the devices experimentally reported here would benefit by increasing the time-bandwidth product. To use spread spectrum techniques to advantage in a communications system employing real-time correlation at the receiver it is necessary to handle codes of long bit length to obtain substantial process gain. At best, the process gain using signal correlation to identify a signal comprised of M bits is M, except for the case of Barker codes in which M^2 is achieveable for $M \leq 13$. Because the operation of the acousto-optic convolver requires that all M bits must simultaneously be accommodated on the device acoustic propagation path for maximum correlation to occur, the crystal sample must be long or the spatial extent of each bit must be short. Moreover, the maximum code length is proportional to the device time-bandwidth product. In the case of ambiguity function generation for radar or sonar, discrimination of a target's range and velocity is proportional to the time-bandwidth product. In image scanning applications of the acousto-optic interaction, the number of resolveable spots per scan is limited by the device time-bandwidth product.

It is readily apparent that for the applications reported the transducer bandwidth should be large, and the optical aperture should be wide, except as noted for the image scanner if a very high repetition rate is required for two dimensional scanning. Generally it is impractical to use an optical aperture greater than $\sim$ 6 cm, although crystals of longer dimension are readily available. It might be possible to employ a folded acoustic path to increase the time bandwidth product of the convolver, but this method would not be of use for the image scanner. The only other means of obtaining higher time-bandwidth products is to use wider transducer bandwidths. For fixed fractional bandwidth this requires higher frequency operation. Effective bandwidth can be increased, also, by using a multiple transducer array composed of transducers of sequential center frequencies with overlapping or contiguous bandwidths. With present technology bandwidths of several hundred megahertz are attainable, providing potential time-bandwidth products of several thousand. A 6 cm optical aperture and a 200 MHz bandwidth would provide a time-bandwidth product of 3440, which is well within the capability of present transducer technology. It is significant that such time-bandwidth products are not to be expected from surface acoustic wave integrated optics devices because of difficulties encountered in coupling over large optical apertures. A 1 cm aperture is the largest reported to date.[80] Of course improvement is to be expected.

the first order intensity for Bragg diffraction to that for Raman-Nath diffraction, $[\sin(\frac{1}{2}x)/J_1(x)]^2$, as a function of the argument x. Thus for most applications, there is no disadvantage in going to the higher acoustic frequencies at which the Bragg regime occurs.

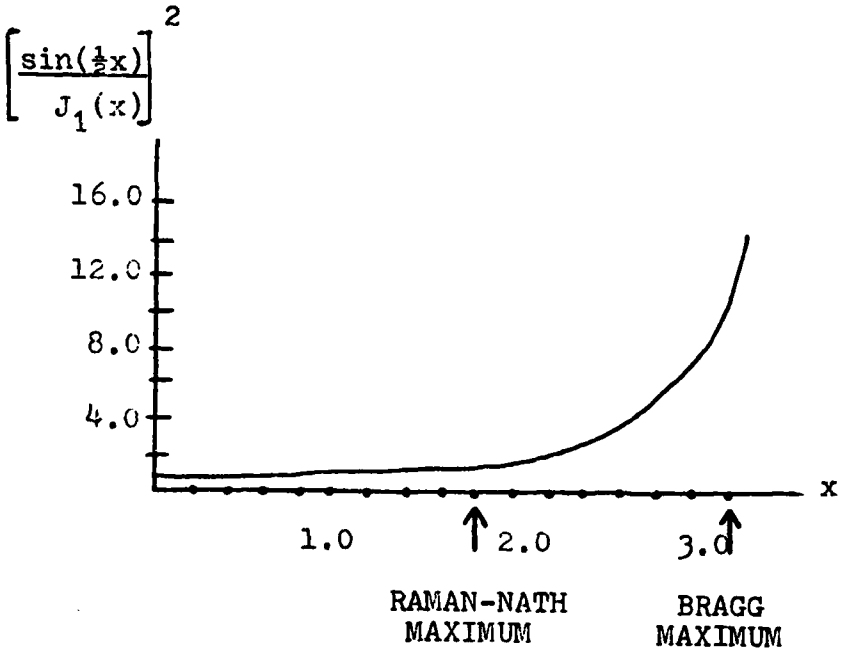

Fig. 4.1 Comparison of Bragg and Raman-Nath First Order Intensity

There is one major difficulty attendant with Bragg diffraction, and that is the optical aperture characteristic. For a given light wavelength and angle of incidence, efficient diffraction occurs only for a very small bandwidth.

It is of interest that while wider bandwidths are available using bulk acoustic waves, this does not result in a proportionate gain in time-bandwidth product. The greater bulk wave velocity produces a diminution of time-bandwidth product.

As was indicated in Chapter 1, the acoustic aperture of an interdigital transducer is important in determining input impedance. For a four and one half finger pair transducer, which optimizes the efficiency-bandwidth product for a transducer fabricated on YZ-$LiNbO_3$, the acoustic aperture which yields a 50 Ω resistive component of input impedance is 108 Λ. Since the interaction length in the side-entry configuration is given by the acoustic aperture, this has the interesting consequence that if impedance matching is to be achieved without the use of a transforming network, the transducer center frequency determines whether the interaction is to be in the Raman-Nath or Bragg regime. For frequencies of 100 MHz and below, the interaction is in the Raman-Nath regime. For frequencies in excess of 100 MHz the interaction becomes more Bragg-like. This is an important consideration.

For low acoustic powers, the Raman-Nath and Bragg regimes yield the same amount of light deflected into the first diffraction order. This follows from Eqns. (2.65) and (2.77), using the approximations $\sin x \sim x$ and $J_1(2x) \sim x$. However at higher powers, the Bragg interaction is more efficient. This is shown by the graph below, Fig. 4.1, which shows the ratio of

frequency which satisfies the Bragg condition. No such difficulty is associated with Raman-Nath devices. Hence, signal processors in the Bragg regime require phased-array frequency-steering acoustic transducers for wide band operation.

In the color image scanning experiment, three color components ranging from 4880 Å to 6328 Å are incident in a collimated beam on the $LiNbO_3$ crystal. Only Raman-Nath diffraction provides a simple means of deflecting all the colors with the same acoustic pulse; Bragg diffraction is inappropriate for this application. As a consequence, at very high acoustic frequencies necessary to achieve a large number of resolveable spots, the side-entry technique is not suitable. One of the less efficient interaction configurations, such as top-transmission, must be used in order to remain in the Raman-Nath regime.

It should be pointed out that as the acoustic frequency increases, the acoustic power resides proportionally closer to the crystal surface. One can anticipate that guiding of the optical wave to confine it near the crystal surface will be essential at high acoustic frequencies. For this reason it is to be expected that most research in the near future in surface wave acousto-optics will be in the area of integrated optics.

From the foregoing discussion, the following guidelines concerning the application of the acousto-optic interaction in surface acoustic waves seem apropos. From the point of view of power consumption, integrated optics devices are most attractive

and will be even more so as higher acoustic frequencies are achieved. These devices are especially well suited at the present time for such functions as digital switching, modulation, and beam steering, since a narrow optical beam can be used in these operations. For device applications in which a large time bandwidth product is required, such as those applications discussed in this report, the wider optical aperture available with the side-entry technique can be used to advantage. Should large time-bandwidth products be obtained with integrated optics devices in the future, almost all the device applications demonstrated here using the side-entry technique could be performed equally well using a guided optical wave. The one exception is that of the color image scanner. In order to remain in the Raman-Nath regime at higher acoustic frequencies, it will be necessary to employ a less efficient interaction configuration.

It is of interest to point out several specific areas where further investigation of the acousto-optic interaction in surface acoustic waves would be pertinent. An analysis of the effect of cone angle and incident light inclination is especially relevant to the side-entry technique. In the present treatment a truncated uniform plane wave with propagation in the x-z plane is assumed, but this idealization does not obtain in practice.

An experimental program to determine the coefficients of the rotation contribution, q_{ijkl}, would be of significant value. Such coefficients might account for the discrepancies in the literature for the other photoelastic constants.

In the area of applications, the present work suggests a number of new applications and new devices which should be investigated. In particular, in the signal processor described in Chapter 3, the integration associated with computing the convolution is performed in the spatial domain. In many applications in which careful laboratory optical alignment is not practical, it might be desireable to perform this integration in the time domain. Implementation involves using a narrow optical aperture and adding a low pass filter for the final electronic processing stage.

The same idea is readily carried over to other device and system applications. The optical communication system discussed in the previous chapter requires that the transmission channel preserve the amplitude distribution of the optical wavefront. While this may not be a deficiency for an intersatellite communication network, it is far too stringent a requirement for present day optical waveguides used in conventional terrestrial communications. An alternative system which does not impose this requirement could again be implemented by taking a narrow optical beam, which we may consider a spatial δ-function, and using a low pass filter to facilitate temporal integration. In such a system

the transmitter end need not be an acousto-optic device. Any suitable means of light modulation could be used for transmission, including direct modulation of a solid state emitter. The important feature of such a system is the acousto-optic correlator at the receiver end.

A slight variant of the optical communication system described above could be used for pulse-doppler laser radar. In this case a high power laser and bulk wave acousto-optic modulator would be required at the transmission end. Following acousto-optic correlation at the receiver, heterodyne optical detection to determine doppler shift is easily performed since transmitter and receiver can be located in close proximity, thus allowing the use of the same laser for purposes of local oscillation.

Another area which warrants attention is the use of the collinear interaction for signal processing purposes. Because polarization rotation occurs only over a narrow acoustic bandwidth for a given light wavelength, previous attention has been paid only to narrow band filtering. Barker encoded data, however, imposed upon a carrier's phase, can be accommodated with narrow band signals. The optical arrangement for a correlator in such a system is shown in Fig. 4.2. The desired correlation signal appears in the photodiode output at twice the acoustic frequency. By using a GaAs LED for the light source and a compatible silicon p-i-n photodiode for detection, operation using YZ-$LiNbO_3$ would be in the 300 MHz range. No lenses are required for optical

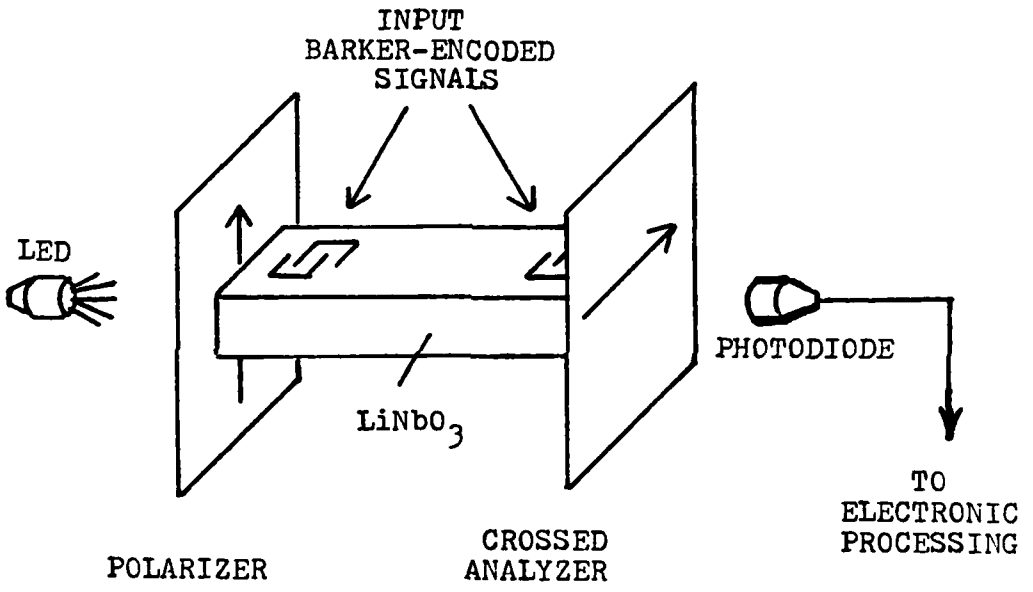

Fig. 4.2 Collinear Convolver

alignment, and the crystal itself would provide directional guiding of the LED output. Simplicity of alignment and compact packaging contribute to the commercial attractiveness of the device.

As with all devices employing the side-entry configuration, there is a corresponding integrated optics analog. An integrated optics collinear convolver could be built based on waveguide mode conversion, rather than polarization rotation. Again, operation is narrow band, but the frequency of operation is determined by waveguide thickness, which is controlled by the designer. In the device utilizing polarization rotation, the operating frequency is dictated by the crystal's birefringence.

The achieveable performance of devices employing the acousto-optic interaction in surface waves is intimately tied to surface acoustic wave technology in general. Progress including improvements in transducer technology and the identification of new crystal cuts with desireable properties will undoubtedly be reflected in more efficient acousto-optic devices operating at higher frequencies and wider bandwidths. Further improvements will come as a result of progress in acousto-optic materials research. It is reasonable to expect that surface wave acousto-optic technology, judiciously applied, will result in economical devices to augment the existing options of the optical and system engineer.

CHAPTER 5

LITERATURE CITED

1. F. Pockels, Lehrbuch der Kristalloptik, Teubner, Leipzig, 1906.

2. L. Brillouin, "Diffusion de la lumière et des rayons X par un corps transparent homgène", Ann. Physique, Vol. 17, p. 88, 1922

3. P. Debye and F. W. Sears, "On the Scattering of Light by Supersonic Waves", Proc. Nat. Acad. Sci. U.S., Vol. 18, p. 409, 1932.

4. C. F. Quate, C. D. W. Wilkinson, D. K. Winslow, "Interactions of Light and Microwave Sound", Proc. IEEE, Vol. 53, p. 1604, 1965.

5. D. A. Pinnow, "Acousto-Optic Light Deflection: Design Considerations for First Order Beam Steering Transducers", IEEE Trans. Sonics and Ultrasonics, Vol. SU-18, p. 209, 1971.

6. S. E. Harris and R. W. Wallace, "Acousto-Optic Tunable Filter", Jour. Opt. Soc. Am., Vol. 59, p. 744, 1969.

   J. A. Kusters, D. A. Wilson, D. L. Hammond, "Optimum Crystal Orientation for Acoustically Tuned Optical Filter", Jour. Opt. Soc. Am., Vol. 64, p. 434, 1974.

   S. T. K. Nieh and S. E. Harris, "Aperture Bandwidth Characteristics of the Acousto-Optic Filter", Jour. Opt. Soc., Am., Vol. 62, p. 672, 1972.

   S. E. Harris and R. W. Wallace, "Acousto-Optic Tunable Filter", Jour. Opt. Soc. Am., Vol. 59, p. 744, 1969.

7. S. E. Harris, S. T. K. Nieh, D. K. Winslow, "Electronically Tunable Acousto-Optic Filter", App. Phys. Lett., Vol. 15, p. 325, 1969.

   W. Streifer and J. R. Whinnery, "Analysis of a Dye Laser Tuned by Acousto-Optic Filter", App. Phys. Lett., Vol. 17, p. 335, 1970.

   S. E. Harris, S. T. K. Nieh, R. S. Feigelson, "$CaMoO_4$ Electronically Tunable Optical Filter", App. Phys. Lett., Vol. 17, p. 223, 1970.

   D. J. Taylor, S. E. Harris, S. T. K. Nieh, T. W. Hansch, "Electronic Tuning of a Dye Laser Using the Acousto-Optic Filter", App. Phys. Lett., Vol. 19, p. 269, 1971.

8. C. S. Tsai and S. K. Yao, "Bragg Diffraction by Standing Ultrasonic Waves with Application to Optical Demultiplexing", Jour. App. Phys., Vol. 43, p. 5081, 1972.

9. M. King, W. R. Bennett, L. B. Lambert, M. Arm, "Real-Time Electrooptical Signal Processors with Coherent Detection", App. Opt., Vol. 6, p. 1367, 1967.

10. E. B. Felstead, "A Simple Real-Time Incoherent Optical Correlator", IEEE Trans. Aerospace and Electronic Systems, Vol. AES-3, p. 907, 1967.

11. M. Born and E. Wolf, Principles of Optics, Pergamon Press, New York, 1965.

J. W. Goodman, Introduction to Fourier Optics, McGraw Hill, New York, 1968.

12. C. V. Raman and N. S. N. Nath, "The Diffraction of Light by High Frequency Sound Waves", Proc. Indian Acad. Sci.: Part I, Vol. 2A, p. 406, 1935; Part II, Vol. 2A, p. 413, 1935; Part III, Vol. 3A, p. 75, 1936; Part IV, Vol. 3A, p. 119, 1936; Part V, Vol. 3A, p. 459, 1936.

N. S. N. Nath, "Generalized Theory", Proc. Indian Acad. Sci., Vol. 4A, p. 222, 1937.

13. A. Yariv, Quantum Electronics, Wiley, New York, 1967.

14. A. Yariv, Introduction to Optical Electronics, Holt, Rinehart and Winston, Inc., New York, 1971.

15. W. R. Klein and B. D. Cook, "Unified Approach to Ultrasonic Light Diffraction", IEEE Trans. Sonics and Ultrasonics, Vol. SU-14, p. 123, 1967.

16. J. F. Nye, Physical Properties of Crystals, Clarendon Press, Oxford, 1957.

17. T. M. Smith and A. Korpel, "Measurement of Light-Sound Interaction Efficiency in Solids", IEEE Jour. Quant. Elect. (Correspondence), Vol. QE-1, p. 283, 1965.

18. E. I. Gordon, "A Review of Acousto-Optical Deflection and Modulation Devices", Proc. IEEE, Vol. 54, p. 1391, 1966.

19. R. W. Dixon, "Photoelastic Properties of Selected Materials and Their Relevance for Applications to Acoustic Light Modulators and Scanners", Jour. App. Phys., Vol. 38, p. 5149, 1967.

20. D. Maydan, "Acoustooptical Pulse Modulators", IEEE Jour. Quant. Elect., Vol. QE-6, p. 15, 1970.

21. D. A. Pinnow, "Guidelines for the Selection of Acousto-Optic Materials", IEEE Jour. Quant. Elect., Vol. QE-6, p. 223, 1970.

22. D. A. Pinnow, L. G. Van Uitert, A. W. Warner, W. A. Bonner, "Lead Molybdate: A Melt-Grown Crystal with a High Figure of Merit for Acousto-Optic Device Applications", App. Phys. Lett., Vol. 15, p. 83, 1969.

N. Uchida and Y. Ohmachi, "Elastic and Photoelastic Properties of TeO_2 Single Crystal", Jour. App. Phys., Vol. 40, p. 4692, 1969.

23. N. Uchida and N. Niizek, "Acoustooptic Deflection Materials and Techniques", Proc. IEEE, Vol. 61, p. 1073, 1973.

24. R. W. Dixon, "Acoustic Diffraction of Light in Anisotropic Media", IEEE Jour. Quant. Elect., Vol. QE-3, p. 85, 1967.

25. W. T. Maloney and H. R. Carleton, "Light Diffraction by Transverse Ultrasonic Waves in Hexagonal Crystals", IEEE Trans. Sonics and Ultrasonics, Vol. SU-14, p. 135, 1967.

26. R. W. Dixon and M. G. Cohen, "A New Technique for Measuring Magnitudes of Photoelastic Tensors and its Application to Lithium Niobate", App. Phys. Lett., Vol. 8, p. 205, 1966.

27. D. A. Pinnow, "Elasto-Optic Materials", Handbook of Lasers with Selected Data on Optical Technology, CRC Press, Cleveland, 1971.

28. M. H. Grimsditch and A. K. Ramdas, "Elastic and Elasto-Optic Constants of Rutile from a Brillouin Scattering Study", Phys. Rev., Vol. B14, p. 1670, 1976.

29. G. Arlt and H. Schweppe, "Paratellurite, a New Piezoelectric Material", Sold State Comm., Vol. 6, p. 783, 1968.

30. I. C. Chang, "Acoustooptic Devices and Applications", IEEE Trans. Sonics and Ultrasonics, Vol. SU-23, p. 2, 1976.

31. E. K. Sittig and H. D. Cook, "A Method for Preparing and Bonding Ultrasonic Transducers Used in High Frequency Digital Delay Lines", Proc. IEEE (Letters), Vol. 56, p. 109, 1968.

32. J. D. Larson III and D. K. Winslow, "Ultrasonically Welded Piezoelectric Transducers", IEEE Trans. Sonics and Ultrasonics, Vol. SU-18, p. 142, 1971.

33. H. C. Huang, J. D. Knox, Z. Turski, R. Wago, and J. J. Hanak, "Fabrication of Submicron $LiNbO_3$ Transducers for Microwave Acoustic (Bulk) Delay Lines", App. Phys. Lett., Vol. 24, p. 109, 1974.

34. D. M. Stevenson and J. J. Hanak, "Low Loss, Broadband Microwave Ultrasonic Delay Lines Using Ion-Beam Milled Shear Wave Transducers", RCA Review, Vol. 35, p. 355, 1974.

35. E. K. Sittig, "Effects of Bonding and Electrode Layers on the Transmission Parameters of Piezoelectric Transducers Used in Ultrasonic Delay Lines", IEEE Trans. Sonics and Ultrasonics, Vol. SU-16, p. 2, 1969.

A. E. Meitzler and E. K. Sittig, "Characterization of Piezoelectric Transducers Used in Ultrasonic Devices Operating Above .1 GHz", Jour. App. Phys., Vol. 40, p. 4341, 1969.

36. See for example, the Special Issue on this subject: IEEE Trans. on Microwave Theory and Techniques, Vol. MTT-17, 1969.

37. P. K. Tien, "Light Waves in Thin Films and Integrated Optics", App. Opt., Vol. 10, p. 2395, 1971.

38. R. M. De LaRue, C. Stewart, C. D. W. Wilkinson, and I. R. Williamson, "Frequency Controlled Beam Steering of Surface Acoustic Waves Using a Stepped Transducer Array", Elect. Lett., Vol. 9, p. 326, 1973.

39. Lord Rayleigh, "On Waves Propagated Along the Plane Surface of an Elastic Solid", Proc. London Math. Soc., Vol. 17, p. 4, 1885.

See also:
E. A. H. Love, Some Problems in Geodynamics, Cambridge University Press, New York, 1911.

R. Stonely, "Elastic Waves at the Surface of Separation of Two Solids", Proc. Royal Soc. (London), Ser. A, Vol. 106, p. 416, 1964.

40. J. H. Collins, H. M. Gerard, H. J. Shaw, "High Performance Lithium Niobate Acoustic Surface Wave Transducers and Delay Lines", App. Phys. Lett., Vol. 13, p. 312, 1968.

41. Burfoot, Ferroelectrics, An Introduction to the Physical Principles, Van Nostrand, Princeton, 1967.

Grindlay, An Introduction to the Phenomenological Theory of Ferroelectricity, Pergamon Press, New York, 1970.

42. H. F. Tiersten, Linear Piezoelectric Plate Vibrations, Plenum Press, New York, 1969.

J. J. Campbell and W. R. Jones, "A Method for Estimating Optimal Crystal Cuts and Propagation Directions for Excitation of Piezoelectric Surface Waves", IEEE Trans. Sonics and Ultrasonics, Vol. SU-15, p. 209, 1968.

H. F. Tiersten, "Wave Propagation in an Infinite Piezoelectric Plate", Jour. Acoust. Soc. Am., Vol. 35, p. 234, 1963.

J. L. Bluestein, "A New Surface Wave in Piezoelectric Materials", App. Phys. Lett., Vol. 13, p. 412, 1968.

K. A. Ingebrigtsen, "Surface Waves in Piezoelectrics", Jour. App. Phys., Vol. 40, p. 2681, 1969.

Chin-Chong Tseng and R. M. White, "Propagation of Piezoelectric and Elastic Surface Waves on the Basal Plane of Hexagonal Piezoelectric Crystals", Jour. App. Phys., Vol. 38, p. 4274, 1967.

43. W. R. Smith, H. M. Gerard, J. H. Collins, T. M. Reeder, H. J. Shaw, "Analysis of Interdigital Surface Wave Transducers by Use of an Equivalent Circuit Model", IEEE Trans. on Microwave Theory and Techniques, Vol. MTT-17, p. 856, 1969.

44. M. G. Cohen and E. I. Gordon, "Acoustic Beam Probing Using Optical Techniques", Bell System Technical Journal, Vol. 44, p. 693, 1965.

E. G. Lean and C. G. Powell, "Optical Probing of Surface Acoustic Waves", Proc. IEEE, Vol. 58, p. 1939, 1970.

A. J. Slobodnik, "Acoustic Surface Wave Investigations Using Laser Light Deflection", Acoustic Surface Waves and Acousto-Optic Devices, ed. T. Kallard, Optosonic Press, New York, 1971.

45. R. Normandin and G. I. Stegeman, "Signal Processing with Surface Waves via the Double Acousto-Optic Interaction", Jour. App. Phys., Vol. 47, p. 2277, 1976.

46. C. J. Kramer, M. N. Araghi, P. Das, "Real Time Convolution Using Acousto-Optic Diffraction from Surface Waves", App. Phys. Lett., Vol. 25, p. 180, 1974.

47. C. J. Kramer, M. N. Araghi, P. Das, "TIR Acousto-Optic Surface Wave Modulator", Presented at the Conference on Laser and Electro-Optical Systems, San Diego, 1976.

48. A. Allipi, A. Palma, L. Palmieri, G. Socino, "Image Scanning Through the Acousto-Optical Effect Produced by Acoustic Surface Waves", App. Phys. Lett., Vol. 26, p. 357, 1975.

49. A. Allipi, A. Palma, L. Palmieri, G. Socino, "Incidence Angle and Polarization Dependence of Light Diffracted by Acoustic Surface Waves", Jour. App. Phys., Vol. 45, p. 1492, 1974.

50. E. G. Lean, "Interaction of Light and Acoustic Waves", Progress in Optics, Vol. XI, ed. E. Wolf, North Holland Publishing Company, Amsterdam, 1973.

51. C. J. Kramer, "Elasto-Optic Investigation of Rayleigh Wave and Layer Wave Properties", Ph.D. Thesis, University of Rochester, 1975.

52. P. Das and D. Schumer, "Signal Processing Using Surface Acousto-Optic Interaction in $LiNbO_3$", Ferroelectrics, Vol. 10, p. 77, 1976. Presented at IEEE Symposium on Applications of Ferroelectrics, Albuquerque, 1975.

53. D. Schumer, L. G. Pearce, P. Das, "Influence of Light Polarization on Performance of Surface Wave Acousto-Optic Convolvers", Presented at Optical Society of America Annual Meeting, Boston, 1975.

54. L. G. Pearce, D. Schumer, P. Das, "Image Scanning Using Acousto-Optic Interaction with Surface Waves", Optics Comm., Vol. 19, p. 65, 1976. Presented at Optical Society of America Annual Meeting, Boston, 1975.

55. P. Das, D. Schumer, H. Estrada-Vazquez, "Optical Communications Using Surface Acoustic Waves", Presented at International Conference on Applications of Holography and Optical Data Processing, Jerusalem, Israel, 1976.

56. P. Das, D. Schumer, F. M. Mohammed Ayub, "Color Image Scanning Using Acousto-Optic Interaction with Surface Waves", Laser Scanning Components and Techniques, SPIE Vol. 84, p. 91, 1976. Presented at Society of Photo-Optical Instrumentation Engineers Annual Meeting, San Diego, 1976.

57. L. Kuhn, M. L. Dakss, P. F. Heidrich, B. A. Scott, "Deflection of an Optical Guided Wave by a Surface Acoustic Wave", App. Phys. Lett., Vol. 17, p. 265, 1970.

R. V. Schmidt, I. P. Kaminow, J. R. Carruthers, "Acousto-Optic Diffraction of Guided Optical Waves in $LiNbO_3$", App. Phys. Lett., Vol. 23, p. 417, 1973.

R. V. Schmidt, "Acoustooptic Interactions Between Guided Optical Waves and Acoustic Surface Waves", IEEE Trans. Sonics and Ultrasonics, Vol. SU-23, p. 22, 1976.

C. S. Tsai and P. Saunier, "New Guided Wave Acousto-Optic and Electro-Optic Devices Using $LiNbO_3$", Ferroelectrics, Vol. 10, p. 257, 1976.

L. T. Nguyen and C. S. Tsai, "Efficient Wideband Guided Wave Acoustooptic Bragg Diffraction Using Phased Surface Acoustic Wave Array in $LiNbO_3$ Waveguides", App. Opt., Vol. 16, p. 1297, 1977.

58. L. Kuhn, P. F. Heidrich, E. G. H. Lean, "Optical Guided Wave Mode Conversion by an Acoustic Surface Wave", App. Phys. Lett., Vol. 19, p. 428, 1971.

59. K. W. Loh, W. S. C. Chang, R. A. Becker, "Convolution Using Guided Acoustooptical Interaction in As_2S_3 Waveguides", Optical Society of America Topic Meeting on Integrated Optics, Salt Lake City, 1976.

60. M. N. Araghi, C. J. Kramer, P. Das, "Acousto-Optic Investigation of Layer Wave Properties", Proc. IEEE Ultrasonics Symposium, p. 103, 1973.

61. H. Meyer, "Design and Performance of a 20-Stage Digital Light Beam Deflector", App. Opt., Vol. 11, p. 1732, 1972.

62. W. C. Wang and P. Das, "Surface Wave Convolver Via Space Charge Nonlinearity", Proc. IEEE Ultrasonics Symposium, p. 316, 1972.

P. Das, M. N. Araghi, W. C. Wang, "Ambiguity Function Generator Using Acoustic Surface Wave Convolvers", Proc. IEEE, Vol. 62, p. 1714, 1974.

M. Yamanishi and T. Kawamura, "Acoustic-Surface-Wave Convolver Using Nonlinear Electron Interactions in Coupled Semiconductor Piezoelectric Systems", Proc. IEEE Ultrasonics Symposium, p. 288, 1972.

H. Gautier, G. S. Kino, H. J. Shaw, "Acoustic Transform Techniques Applied to Optical Imaging", Proc. IEEE Ultrasonics Symposium, p. 99, 1974.

63. G. A. Coquin, "Acoustic-Optic Interactions in Piezoelectric Crystals", Presented at IEEE Ultrasonics Symposium, St. Louis, 1969.

64. D. A. Pinnow, "Elasto-Optical Materials", Handbook of Lasers with Selected Data on Optical Technology, CRC Press, Cleveland, 1971.

65. D. F. Nelson and M. Lax, "New Symmetry for Acousto-Optic Scattering", Phys. Rev. Lett., Vol. 24, p. 378, 1970.

D. F. Nelson and M. Lax, "Theory of the Photoelastic Interaction", Phys. Rev., Vol. B3, p. 2778, 1971.

66. D. F. Nelson and P. D. Lazay, "Measurement of the Rotational Contribution to Brillouin Scattering", Phys. Rev. Lett., Vol. 25, p. 1187, 1970.

67. N. Bloembergen, Nonlinear Optics, Benjamin, New York, 1965.

68. R. N. Spaight and G. G. Koerber, "Piezoelectric Surface Waves on $LiNbO_3$", IEEE Trans. Sonics and Ultrasonics, Vol. SU-18, p. 237, 1971.

69. G. W. Willard, "Criteria for Normal and Abnormal Ultrasonic Light Diffraction Effects", Jour. Acoust. Soc. Am., Vol. 21, p. 101, 1949.

70. R. Extermann and G. Wannier, "Theory de la diffraction de la lumière par les ultrasons", Helv. Phys. Acta (Switzerland), Vol. 9, p. 520, 1936.

71. C. J. Kramer, "Elasto-Optic Investigation of Rayleigh Wave and Layer Wave Properties", Ph.D. Thesis, University of Rochester, 1975.

72. P. Phariseau, "On the Diffraction of Light by Progressive Supersonic Waves", Proc. Indian Acad. Sci., Vol. 44A, p. 165, 1956.

73. I. P. Kaminow and E. H. Turner, "Linear Electrooptical Materials", Handbook of Lasers with Selected Data on Optical Technology, CRC Press, Cleveland, 1971.

74. R. W. Dixon and M. G. Cohen, "A New Technique for Measuring Magnitudes of Photoelastic Tensors and its Application to Lithium Niobate", App. Phys. Lett., Vol. 8, p. 205, 1966.

75. H. L. Van Trees, Detection, Estimation and Modulation Theory, John Wiley and Sons, New York, 1971.

76. R. Mertens, "On the Theory of the Diffraction of Light by Two Parallel Ultrasonic Waves, One Being the n^{th} Harmonic of the Other", Zietschrift für Physik, Vol. 160, p. 291, 1960.

77. C. Atzeni and L. Pantani, "Optical Signal Processing Through Dual Channel Ultrasonic Light Modulators", Proc. IEEE (Letters), Vol. 58, p. 501, 1970.

L. Slobodnik, "Optical Correlation Technique", Proc. IEEE, Vol. 51, p. 1782, 1963.

78. N. J. Moll, O. W. Otlo, C. F. Quate, "Scanning Optical Patterns with Acoustic Surface Waves", Journal de Physique, Vol. 33C6, p. 231, 1972.

M. Luukkala and P. Merilainen, "Image Scanning by Acousto-Electro-Optic Interaction", Elect. Lett., Vol. 10, p. 80, 1974.

S. Takada, H. Hayakaw, N. Mikoshiba, "Surface Wave Acousto-Electric Image Scanner", Proc. 5th (International) Conference on Solid State Devices, p. 194, 1973.

79. A. Korpel, R. Adler, P. Desmares, W. Watson, "A Television Display Using Acoustic Deflection and Modulation of Coherent Light", Proc. IEEE, Vol. 54, p. 1429, 1966.

80. C. S. Tsai, "Wideband Guided-Wave Acousto-Optic Bragg-Devices and Applications", Proc. IEEE Ultrasonic Symposium, p. 120, 1975.

APPENDIX

DERIVATION OF THE WAVE EQUATION

In this appendix we derive from Maxwell's equations of electromagnetic theory the wave equation which is the starting point for the analysis of the acousto-optic interaction. In rationized MKS units, Maxwell's equations can be written in the form

$$\nabla \cdot \overleftrightarrow{\epsilon}\, \vec{E} = \rho \tag{A.1}$$

$$\nabla \times \vec{E} = -\frac{\partial \vec{B}}{\partial t} \tag{A.2}$$

$$\nabla \cdot \vec{B} = 0 \tag{A.3}$$

$$\nabla \times \vec{B} = \mu_o \vec{J} + \frac{\partial}{\partial t} \overleftrightarrow{\epsilon}\, \vec{E} \tag{A.4}$$

where it has been assumed that the material is linear and non-magnetic. $\vec{E}$ and $\vec{B}$ are, respectively, the electric field and magnetic field intensity, ρ and $\vec{J}$ are the free charge density and free current density, μ_o is the permeability of free space, and $\overleftrightarrow{\epsilon}$ is the permittivity tensor which describes the material. The equation of interest is obtained from the vector equation (A.2) in the usual manner by taking the curl of that equation, using the vector identity $\nabla \times \nabla \times \vec{A} = -\nabla^2 \vec{A} + \nabla (\nabla \cdot \vec{A})$ for any vector $\vec{A}$, reversing the order of the curl and time derivative operations on the right hand side, eliminating $\vec{B}$ by means of Eq. (A.4), and assuming $\rho = \vec{J} = 0$ in the material.

Expressing the resultant vector equation in an orthogonal coordinate system in which $\mathbf{E} = \hat{e}_i E_i$, where $\hat{e}_i$ is a unit vector, and the Einstein convention is employed in which repeated subscripted indices indicate summation over those indices, we obtain the three scalar equations:

$$- \nabla^2 E_i + [\nabla(\nabla \cdot \mathbf{E})]_i = - \mu_o \frac{\partial^2}{\partial t^2} \varepsilon_{ij} E_j \qquad (A.5)$$

Summation over $j = 1,2,3$ is understood on the right hand side; the subscript i can take on values $i = 1,2$, or 3. We shall now show that for all cases which we shall consider, the term on the left hand side involving the gradient is negligible compared to all other terms in the equation. We indicate this for the isotropic case in which the permittivity can be represented by a scalar function, however the result will apply to a tensor as well.

With $\rho = 0$, Eq. (A.1) can be written

$$\nabla \cdot \vec{E} = \frac{\vec{E} \cdot \nabla \varepsilon}{\varepsilon} \quad , \qquad (A.6)$$

in obtaining which the following vector identity has been employed:

$$\nabla \cdot f \vec{F} = \vec{F} \cdot \nabla f + f \nabla \cdot \vec{F} \qquad (A.7)$$

in which f is a scalar function and $\vec{F}$ is a vector-valued function of a scalar argument. In Eq. (A.6), $\vec{E}$ is taken to be the electric field associated with light propagation, and ε represents the

permittivity of the material, which we allow to be perturbed by the presence of a propagating acoustic wave. For light propagating in the x_1-direction, or nearly so, we may neglect E_1 and take

$$\vec{E} \simeq \hat{e}_2 E_2 (x,y,z,t) + \hat{e}_3 E_3 (x,y,z,t) \quad , \tag{A.8}$$

in which the orthogonal axes (x_1, x_2, x_3) are identified with the usual (x,y,z) designations. Thus the inner product on the right hand side of Eq. (A.6) only involves a sum over the y and z components.

It will be sufficient to consider an exponentially decaying surface acoustic wave propagating in the z-direction. In this case the relative permittivity can be written as

$$\frac{1}{\varepsilon_o} \varepsilon = \varepsilon^o + Ae^{-\alpha y} \cos (\omega_a t - k_a z) \tag{A.9}$$

where ε_o is the permittivity of free space, ε^o is the unperturbed relative permittivity, and the subscript "a" refers to the acoustic wave. As the perturbation is very small, $A/\varepsilon^o < 10^{-4}$, we may take $\varepsilon \sim \varepsilon_o \varepsilon^o$ in the denominator of Eq. (A.6), and write (A.5) in the isotropic case as

$$-\nabla^2 E_i - \frac{\partial}{\partial x_i} \left(E \cdot \frac{\nabla \varepsilon}{\varepsilon^o}\right) = - \frac{1}{c^2} \frac{\partial^2}{\partial t^2} \{[\varepsilon^o + A e^{-\alpha y} \cos (\omega_a t - k_a z)] E_i\} \tag{A.10}$$

where we have used the fact that the speed of light in free space, c, is given by $(\varepsilon_o \mu_o)^{-1/2}$. In the anisotropic case, in which we allow ε to be a tensor, the last term of the right hand side would

be replaced by the sum of two terms, each of which would be similar in form to the term given in Eq. (A.10).

We show now that the gradient term on the left hand side of Eq. (A.10) is negligible compared to the other small term in the equation, $-1/c^2\ \partial^2/\partial t^2\ A\ e^{-\alpha y} \cos(\omega_a t - k_a z)\ E_i$. In establishing this result, we make the physically reasonable assumption that the spatial rate of change of the electric field E_i, normalized to the magnitude of E_i, is less than or equal to that of the permittivity ε.

The relation we wish to establish is

$$\frac{\left| \frac{\partial}{\partial x_i} \sum_{j=2,3} E_j \frac{\partial}{\partial x_j} \left(\frac{\varepsilon}{\varepsilon^o}\right) \right|}{\left| \frac{1}{c^2} \frac{\partial^2}{\partial t^2} A\ e^{-\alpha y} \cos(\omega_a t - k_a z)\ E_i \right|} \ll 1 \qquad \text{(A.11)}$$

Consider one term of the numerator of (A.11). Using the assumption that the spatial rate of change of the electric field is less than that of the permittivity, observing that the surface wave decay constant α is typically on the order of k_a, and making use of Eq. (A.9),

$$\left| \frac{\partial}{\partial x_i} E_j \frac{\partial}{\partial x_j} \left(\frac{\varepsilon}{\varepsilon^o}\right) \right| \lesssim \left| k_a^2\ A\ e^{-\alpha y} \cos(\omega_a t - k_a z) \right| \qquad \text{(A.12)}$$

The optical electric field is periodic in time with an angular frequency ω which is much larger than ω_a. Thus the denominator of (A.11) obeys

$$\left| \frac{1}{c^2} \frac{\partial^2}{\partial t^2} \left[A\, e^{-\alpha y} \cos (\omega_a t - k_a z)\, E_i \right] \right|$$

$$\gtrsim \left| \frac{1}{c^2}\, \omega^2\, A\, e^{-\alpha y} \cos (\omega_a t - k_a z)\, E_i \right| \qquad \text{(A.13)}$$

The relation $\omega^2/c^2 >> k_a^2$, together with Eqs. (A.12) and (A.13), establishes the inequality (A.11).

It is apparent that the same arguments could easily be generalized to the anisotropic case. The final result is that the wave equation (A.5) can be written neglecting the gradient term:

$$-\nabla^2 E_i = -\frac{1}{c^2} \frac{\partial^2}{\partial t^2} (\varepsilon_{ij} E_j) \qquad \text{(A.14)}$$